

# Accretion Disk Weather of Black Hole X-Ray Binaries

The Case of Cygnus X-1

Dissertation  
zur Erlangung des Grades eines  
Doktors der Naturwissenschaften  
der Fakultät für Physik  
der Eberhard-Karls-Universität Tübingen

vorgelegt von

Katja Pottschmidt

aus Aurich  
2002

Selbstverlegt von: K. Pottschmidt, Spechtstr. 9, 72336 Balingen  
Tag der mündlichen Prüfung: 20. Dez. 2002  
Dekan: Prof. Dr. H. Müther  
1. Berichterstatter: Prof. Dr. R. Staubert  
2. Berichterstatter: Prof. Dr. G. Hasinger  
3. Berichterstatter: Prof. Dr. K. Werner

## Erweiterte deutsche Zusammenfassung

Pottschmidt, Katja

### Akkretionsscheibenwetter von Schwarzschröntgendoppelsternen — Der Fall Cygnus X-1 —

Die Beobachtung der Röntgenemission, die bei der Akkretion von Materie durch ein schwarzes Loch entsteht, gibt uns die bisher einzige Gelegenheit, den Einfluß dieser wichtigen und faszinierenden Objekte auf ihre unmittelbare Umgebung zu untersuchen. Es sind zwei grundlegende Szenarien bekannt, bei denen es zur Akkretion auf ein schwarzes Loch kommen kann: für schwarze Löcher von einigen Sonnenmassen in Doppelsternsystemen oder für supermassive schwarze Löcher von  $10^6$ – $10^8 M_{\odot}$  im Zentrum aktiver Galaxienkerne. Diese Arbeit beschäftigt sich mit der erstgenannten Art schwarzer Löcher.

Eine der charakteristischen Eigenschaften der Röntgenemission schwarzer Löcher ist ihre starke aperiodische Variabilität auf Zeitskalen von  $\sim 100$  s bis hinunter zu typischerweise  $\sim 0.01$  s. Im Vergleich zu Forschungsprojekten, die sich darauf konzentrieren, die Röntgenenergiespektren zu messen und zu modellieren, sind Untersuchungen dieser Kurzzeitvariabilität jedoch weniger fortgeschritten. Seit dem Start des “Rossi X-Ray Timing Explorer” – *RXTE* – Satelliten im Dezember 1995 stehen allerdings zeitlich hochaufgelöste Beobachtungen im Bereich von 2–250 keV zur Verfügung, die die Berechnung neuer Lichtkurvenstatistiken sowie neue Modellierungsansätze ermöglichen. Zusätzlich sind regelmäßige Monitoringbeobachtungen über Wochen bis Jahre eine besondere Stärke dieses Experiments.

Vor diesem Hintergrund wurden von 1998 bis 2001 regelmäßige *RXTE* Monitoringbeobachtungen des Röntgendoppelsterns Cygnus X-1 durchgeführt. Diese Messungen stellen den Hauptteil einer Beobachtungskampagne in mehreren Wellenlängenbereichen dar, die die Datenbasis für diese Doktorarbeit bildet. Die hier hauptsächlich benutzten Analysemethoden sind die Berechnung von Fouriergrößen höherer Ordnung (Zeitverzögerungen oder Kohärenzfunktionen zwischen verschiedenen Energiebändern) der hochaufgelösten *RXTE* Lichtkurven (gewählte Auflösung: 4 ms), wie auch die *Modellierung* dieser Lichtkurven im Frequenzraum (durch multi-Lorentz Fits an die Periodogramme). So wurden neue Informationen aus der Kurzzeitvariabilität gewonnen, die es ermöglichen, aktuelle physikalische Akkretionsmodelle weiter zu verbessern. Diese Methoden wurden erst kürzlich entwickelt und wurden niemals zuvor auf so einen großen, einheitlichen Datensatz von Schwarzschröhtgendoppelsternen angewandt. Der letzte Punkt ist vor allem deshalb wichtig, weil Schwarzschröhtgendoppelsterne verschiedene Emissionszustände einnehmen (“hard state” und “soft state”), deren jeweilige innere Stabilität niemals zuvor systematisch

beobachtet, geschweige denn berücksichtigt, wurde.

Das Monitoring hat unter anderem enthüllt, daß 1998 ein Übergang von einem langfristig ruhigen “hard state” mit starker Kurzzeitvariabilität zu einem anderen “hard state” mit wochenlangen Intensitätsausbrüchen im Bereich von 2–13 keV und weniger starker Kurzzeitvariabilität stattgefunden hat. Es wurde entdeckt, daß die Berechnung der Fourierphase zwischen zwei Energiebändern die Identifizierung der Ausbrüche als “fehlgeschlagene Übergänge” in den “soft state” erlaubt. Außerdem konnte gezeigt werden, daß die Modellierung des Zeitverhaltens mit diskreten Komponenten, die durch verschiedene Zentralfrequenzen charakterisiert sind, konsistent für alle “hard state” Beobachtungen der Kampagne möglich ist. Während (fehlgeschlagener) Übergänge unterstützen diese Diagnosemethoden – zusammen mit der Beobachtung von simultanen Ausbrüchen im Radiobereich – neuere Jet-Scheiben-Akkretionsmodelle. Diese Modelle gehen davon aus, daß ein Teil des Materials in der Akkretionsregion nicht vom schwarzen Loch “verschluckt” wird, sondern seine Nachbarschaft in Form eines Materieausflusses wieder verläßt.

Die Struktur dieser Arbeit ist die folgende: In Kapitel 1 wird zunächst die Entwicklung geschildert, die 1971 schließlich zur Identifizierung des ersten stellaren schwarzen Lochs, Cygnus X-1, in einem Röntgendoppelstern geführt hat. Ein O Überriesenstern, HDE 226828, ist die optische Komponente dieses Systems, das auch im Radiobereich detektiert wurde. Danach werden die verschiedenen Klassen von Schwarzlöchröntgendoppelsternen vorgestellt und ein Überblick über die bisher entdeckten Quellen wird gegeben. Anschließend werden die Geometrie sowie die wichtigsten Parameter von Cygnus X-1/HDE 226868 zusammengefaßt. Der Rest des Einführungskapitels ist einer Beschreibung der Beobachtungskampagne für diese Quelle, einschließlich einer kurzen Vorstellung des *RXTE* Satelliten, gewidmet.

Gegenstand von Kapitel 2 sind die verschiedenen Emissionszustände von Schwarzlöchröntgendoppelsternen. Das Standardbild, das sich in den letzten Jahren herauskristallisiert hat, geht von zwei prinzipiellen Emissionskomponenten, die zu den beobachteten Zuständen beitragen, aus: Schwarzkörperstrahlung im weichen Röntgenbereich von der Akkretionsscheibe, sowie ein härteres Potenzgesetzspektrum, das durch inverse Comptonstöße in einem heißen Plasma entsteht. Dieses Kapitel ist in zwei Abschnitte unterteilt, wovon sich der erste darauf konzentriert, die Beobachtungscharakteristika von Schwarzlöchröntgendoppelsternen zusammenzufassen, während der zweite die physikalischen Modelle vorstellt, die diskutiert werden, um diese Beobachtungen zu erklären.

Die mathematischen Methoden, die bei der Auswertung der Kurzzeitvariabilität der Cygnus X-1 *RXTE* Monitoringbeobachtungen angewandt wurden, werden in Kapitel 3 beschrieben. Dazu gehören die Berechnung der Fourier Transformierten der hochaufgelösten Lichtkurven in mehreren Energiebändern, sowie die daraus gewonnenen Periodogramme, Kohärenzfunktionen und frequenzabhängigen Zeitverzöge-

rungen. Zuerst wird die mathematische Formulierung dieser Größen entwickelt, einschließlich ihrer statistischen Unsicherheiten und Rauschkomponenten. Danach werden Beispiele, berechnet für eine der Cygnus X-1 Beobachtungen, präsentiert. Sie wurden mit Hilfe von IDL Programmen gewonnen, die im Rahmen dieser Doktorarbeit für die Analyse von *RXTE* Monitoringbeobachtungen entwickelt wurden.

Die Kapitel 4 und 5 enthalten die Ergebnisse aus der Analyse aller 130 Cygnus X-1 Monitoringbeobachtungen, sowie weiterer, öffentlicher *RXTE* Beobachtungen, die während des bekannten “soft states” von 1996 durchgeführt wurden. Der Schwerpunkt liegt dabei auf der Darstellung der verschiedenen zeitlichen Eigenschaften und auf der Modellierung der Periodogramme, aber eine Modellierung der Energiespektren und eine Evaluierung der Entwicklung des Radioflusses sind ebenfalls Teil der Analysen. Die zeitliche Entwicklung der frequenzabhängigen Zeitverzögerungen zwischen den Variabilitätsstrukturen in zwei verschiedenen Energiebändern steht im Mittelpunkt von Kapitel 4. Diese Untersuchung führte u.a. zu der Identifizierung der “fehlgeschlagenen Zustandsübergänge”. Kapitel 5 konzentriert sich auf die Modellierung der Periodogramme mit diskreten Lorentzfunktionen. So konnte zum ersten Mal gezeigt werden, daß eine solche Zerlegung für alle Cygnus X-1 “hard state” Beobachtungen konsistent möglich ist. Beide Ergebniskapitel basieren jeweils auf einer Veröffentlichung, Pottschmidt et al. (2000) und Pottschmidt et al. (2002).

Das abschließende Kapitel 6 faßt zunächst die Ergebnisse noch einmal zusammen. Um die Periodogrammfits mit ähnlichen Untersuchungen neueren Datums an anderen Röntgendoppelsternen vergleichen zu können, werden dann Korrelationen zwischen den “Peakfrequenzen” der Lorentzkomponenten präsentiert und diskutiert. Ein physikalisches Akkretionsszenario, das als mögliches Erklärungsmodell für die Ergebnisse aus den verschiedenen Analysen in Betracht gezogen werden kann, wird vorgeschlagen. In diesem Zusammenhang weisen beide Ansätze – die Untersuchung der Zeitverzögerungen, wie auch die Modellierung der Periodogramme – auf eine vertikale Expansion der Akkretionsregion während fehlgeschlagener und erfolgreicher Zustandsübergänge hin. Schließlich werden noch geplante zukünftige Projekte vorgestellt, die auf der Datenbasis aus der Cygnus X-1 Kampagne aufbauen sollen.



## Abstract

Pottschmidt, Katja

### Accretion Disk Weather of Black Hole X-Ray Binaries — The Case of Cygnus X-1 —

Observing the X-ray emission produced by accretion of matter onto a black hole gives us the so far unique opportunity to study the influence of these important and fascinating objects on their immediate surroundings. In principle two different scenarios are known where accretion onto a black hole is possible: for stellar mass black holes in a binary system or for supermassive black holes of  $10^6$ – $10^8 M_{\odot}$  in the center of Active Galactic Nuclei. This work focuses on the first type of black holes.

One of the characteristic properties of the X-ray emission of black holes is its strong aperiodic variability on timescales from  $\sim 100$  s down to typically  $\sim 0.01$  s. Compared to research projects concentrating on measuring and modeling the X-ray energy spectra, the understanding of this short term variability is less advanced. However, with the launch of the “Rossi X-Ray Timing Explorer” – *RXTE* – satellite in 1995 December, high time resolution observations in the 2–250 keV regime became available that allow to compute new lightcurve statistics and use new modeling approaches. In addition, regular monitoring observations, sampling weeks to years, are a special strength of this experiment.

On this background, regular *RXTE* monitoring of the black hole X-ray binary Cygnus X-1, were performed from 1998 to 2001. They make up the central part of the multi-wavelength observation campaign for that source which constitutes the data basis of this thesis. Higher order Fourier analyses (time lags and coherence functions between different energy bands) of the high resolution *RXTE* lightcurves (selected bintime: 4 ms) as well as *modeling* of the variability of those lightcurves in the frequency domain (multi-Lorentzian fits to the power spectra) are the main analysis methods that were applied here. Thus new information was extracted from the short term variability that can be used to constrain current physical accretion models. These methods have only recently been developed and have never before been applied to such a uniform data set of black hole X-ray binary observations. The latter is important since these sources are known to assume different emission states (“hard/soft state”) whose internal long term stability has never been systematically observed before, let alone been taken into account.

Among other things, the monitoring revealed a 1998 transition from a long term quiet hard state with strong short term variability to a different hard state showing week-long flares in the 2–13 keV range and weaker short term variability. It was found that calculating the Fourier phase between two energy bands allows to identify

the observed flaring as “failed transitions” to the soft state. Additionally, modeling of the timing behavior with discrete components characterized by different center frequencies could be shown to be consistently possible for all hard state observations. During the (failed) state transitions these diagnostics – together with the observation of simultaneous radio flares – strongly support recent jet-disk-accretion models. These models assume that a fraction of the material in the accretion region is not “swallowed” by the black hole but leaves its neighborhood again in form of an outflow.

The outline of this thesis is as follows: chapter 1 starts with the description of the historical evolution which in 1971 finally led to the identification of the first stellar mass black hole, Cygnus X-1, in an X-ray binary. A supergiant O-star, HDE 226828, is the optical component of this system, which has also been detected at radio wavelengths. Next, the different classes of black hole X-ray binaries are introduced and an overview of the known sources is given. The geometry as well as the most important parameters of Cygnus X-1/HDE 226868 are summarized. The remainder of the introductory chapter is dedicated to a description of the observing campaign for this source, including a short introduction of the *RXTE* satellite.

Chapter 2 focuses on the different emission states of black hole X-ray binaries. In the standard picture of black hole states which has emerged in recent years, two principal emission components exist which contribute to the observed states: black body radiation of the accretion disk in the soft X-ray regime and a harder power law spectral component which is produced by inverse Compton scattering in a hot plasma. This chapter is divided into two parts: one concentrating on summarizing the observational properties of black hole X-ray binaries and the other on introducing the physical models that are discussed to explain these observations.

In chapter 3 the mathematical methods are described which were used to characterize the short term variability as found in the Cygnus X-1 *RXTE* monitoring observations. This includes the calculation of the Fourier transforms of the high resolution lightcurves in several energy bands, as well as the power spectra, coherence functions, and frequency dependent time lags. First, the mathematical formulation of these quantities is developed, including their uncertainties and noise components. Then, examples calculated for one of the Cygnus X-1 observations are presented. They were obtained with IDL tools specifically developed as part of this thesis for analyzing *RXTE* monitoring observations.

The chapters 4 and 5 contain the results of analyzing  $\sim 130$  Cygnus X-1 monitoring observations plus additional public *RXTE* observations performed during the well known 1996 soft state. Here, the emphasis lies on presenting the different timing properties and on modeling the power spectra, but modeling of the energy spectra and an evaluation of the radio flux evolution are also included. The main objective of chapter 4 is to study the temporal evolution of the frequency dependent time lags



between the variability structures in different energy bands. Among other results this leads to the definition of “failed” state transitions. Chapter 5 concentrates on modeling the power spectra in terms of discrete Lorentzian components, showing for the first time that such a description is possible for all Cygnus X-1 hard state observations in a consistent way. The structure of each of those chapters is based on a publication, Pottschmidt et al. (2000) and Pottschmidt et al. (2002) for chapter 4 and 5, respectively.

The remaining chapter 6 first summarizes the results. In order to be able to compare the power spectra fits with similar recent studies on other X-ray binaries, correlations between the Lorentzian peak frequencies are then presented and discussed. A physical accretion scenario which can be considered as a possible model for explaining the results of the different analyses is proposed. In this context both approaches – studying the lags as well as modeling the power spectra – indicate the vertical expansion of the accretion region during state transitions, failed and successful ones. Finally, an outlook on planned future work involving data from the Cygnus X-1 monitoring campaign is given.

# Contents

---

<b>1</b>	<b>Black Hole X-Ray Binaries</b>	<b>16</b>
1.1	History . . . . .	16
1.2	X-ray Emission . . . . .	19
1.3	Sources . . . . .	22
1.4	Cygnus X-1 . . . . .	27
1.5	Monitoring of Cygnus X-1 . . . . .	30
1.6	Thesis Outline . . . . .	33
<b>2</b>	<b>The States of BHXRBs</b>	<b>35</b>
2.1	Observational Properties . . . . .	35
2.1.1	Hard State . . . . .	36
2.1.2	Soft State . . . . .	39
2.1.3	Intermediate / Very High State . . . . .	40
2.1.4	Quiescent State . . . . .	42
2.1.5	Transitions: LMC X-3 . . . . .	45
2.1.6	Transitions: New Results . . . . .	45
2.2	Models . . . . .	46
2.2.1	$\alpha$ Disk . . . . .	47
2.2.2	SLE . . . . .	49
2.2.3	ADC . . . . .	50
2.2.4	ADAF . . . . .	59
2.2.5	Jets . . . . .	60
2.3	The Importance of Timing Studies . . . . .	62
<b>3</b>	<b>Fourier Statistics</b>	<b>65</b>
3.1	The Discrete Fourier Transform . . . . .	65
3.2	The Power Spectral Density . . . . .	66
3.2.1	PSD, Averaging . . . . .	66
3.2.2	PSD Normalization, Background . . . . .	67
3.2.3	PSD Uncertainties . . . . .	69
3.2.4	PSD Noise, Deadtime . . . . .	69

3.3	The Cross Power Density . . . . .	73
3.3.1	CPD, Averaging . . . . .	73
3.4	The Coherence Function . . . . .	74
3.4.1	Coherence . . . . .	74
3.4.2	Coherence Noise . . . . .	75
3.4.3	Coherence Uncertainties . . . . .	76
3.5	The Lags . . . . .	76
3.5.1	Phase- and Time Lags . . . . .	76
3.5.2	Noise Estimation . . . . .	77
3.5.3	Time Lag Uncertainties . . . . .	77
3.6	Example: Cygnus X-1, IDL Tools . . . . .	78
<b>4</b>	<b>Temporal Evolution of X-ray Lags in Cygnus X-1</b>	<b>85</b>
4.1	Observations and Data Analysis . . . . .	85
4.2	Temporal Evolution of the Lags . . . . .	86
4.3	Discussion and Conclusions . . . . .	88
<b>5</b>	<b>Modeling PSDs of Cygnus X-1 &amp; More</b>	<b>91</b>
5.1	Observations and Data Analysis . . . . .	92
5.1.1	The <i>RXTE</i> Monitoring Observations of Cygnus X-1 . . . . .	92
5.1.2	Computation of the Power Spectra . . . . .	93
5.1.3	Modeling the Power Spectra . . . . .	94
5.1.4	Time Lags, Coherence, and Spectral Modeling . . . . .	99
5.2	Evolution of the Power Spectrum . . . . .	100
5.2.1	The Two Hard States . . . . .	103
5.3	Failed State Transitions and the 2001 October Soft State . . . . .	108
5.3.1	1998 July . . . . .	111
5.3.2	1999 December . . . . .	112
5.3.3	2000 November . . . . .	113
5.3.4	2001 October: A Short Soft State . . . . .	113
5.3.5	2001 January: A Possible Soft State . . . . .	117
<b>6</b>	<b>Summary, Conclusions, and Outlook</b>	<b>119</b>
6.1	Summary . . . . .	119
6.2	Relationship between Neutron Star and Black Hole Frequencies . . . . .	120
6.3	A Possible Physical Scenario . . . . .	122
6.4	Outlook . . . . .	126
	<b>Bibliography</b>	<b>128</b>
<b>A</b>	<b>Table of Fit Results</b>	<b>137</b>

Acknowledgements 150

Lebenslauf 152

## List of Figures

---

1.1	Equipotential lines of the Roche potential for Cyg X-1 . . . . .	19
1.2	Accretion disk temperature profile . . . . .	22
1.3	Accretion disk around a black hole . . . . .	23
1.4	Basic components of the HDE 226868/Cyg X-1 binary . . . . .	27
1.5	<i>RXTE/ASM</i> lightcurve of Cyg X-1 from 1996 to 2002 . . . . .	31
2.1	Measured BHXRB broad band energy spectra . . . . .	36
2.2	Measured BHXRB power spectra . . . . .	37
2.3	The canonical BHXRB states . . . . .	38
2.4	Multi-wavelength lightcurves of GX 339-4 . . . . .	39
2.5	Cyg X-1 spectra extending into the MeV regime . . . . .	40
2.6	Relative strength of accretion disk and Comptonizing plasma . . . . .	42
2.7	<i>MERLIN</i> observations of GRS 1915+105 . . . . .	43
2.8	Spectral evolution of LMC X-3 in 1999 . . . . .	44
2.9	Density distribution simulation for a standard accretion disk . . . . .	48
2.10	The magneto-rotational instability . . . . .	49
2.11	Accretion geometries . . . . .	50
2.12	Magnetic loops above a thin accretion disk . . . . .	51
2.13	Compton scattering of a photon from a stationary electron . . . . .	52
2.14	Monte Carlo simulation of spectra produced by thermal Comptonization . . . . .	54
2.15	Spectral models for an <i>RXTE/PCA</i> observation of GX 339-4 . . . . .	55
2.16	Simulated spectra emerging from a hybrid plasma . . . . .	57
2.17	Simulated spectra produced by reprocessing in the accretion disk . . . . .	58
2.18	Decomposition of a flat, optically thick radio spectrum . . . . .	60
2.19	Broad band hard state spectrum of XTE J1118+480 . . . . .	61
2.20	Power spectrum and time lags from a modified shot noise model . . . . .	63
3.1	Poisson noise power spectrum and its deadtime correction . . . . .	72
3.2	Vector representation of the Cross Power Density . . . . .	74
3.3	Typical power spectra of Cyg X-1, noise, uncertainties . . . . .	80
3.4	Typical coherence functions of Cyg X-1, noise, uncertainties . . . . .	81
3.5	Typical time lag spectra of Cyg X-1, uncertainties . . . . .	83

4.1	Two hard state time lag spectra of Cyg X-1 . . . . .	86
4.2	Temporal evolution of the average lag in different frequency bands and of the <i>RXTE/ASM</i> flux in 1998 . . . . .	87
4.3	Temporal evolution of the average lag and the <i>RXTE/ASM</i> flux from 1996–1998 . . . . .	88
4.4	Time lag spectra of Cyg X-1 for different states . . . . .	89
5.1	Typical multi-Lorentzian fit to the hard state power spectrum, I. .	95
5.2	Typical multi-Lorentzian fit to the hard state power spectrum, II. .	96
5.3	Spectral and timing parameters of Cyg X-1 from 1998–2001 . .	101
5.4	<i>RXTE/PCA</i> count rate, <i>RXTE/ASM</i> count rate, and 15 GHz radio flux for Cyg X-1 from 1998–2001 . . . . .	102
5.5	Peak frequency ratios . . . . .	103
5.6	Normalization of the four broad noise components, $R_i$ , versus their peak frequencies, $\nu_i$ . . . . .	105
5.7	Correlations between time lags, photon indices, and peak frequencies . . . . .	106
5.8	Energy dependence of the peak frequencies . . . . .	107
5.9	Power spectra and Lorentzian fits during failed state transitions .	109
5.10	Evolution of the power spectra over flaring events . . . . .	110
5.11	Normalization of $L_1$ as a function of energy . . . . .	112
5.12	Evolution of the power spectrum during 2000 November . . . .	114
5.13	<i>RXTE/ASM</i> count rate and 15 GHz flux of Cyg X-1 during the fall of 2001 . . . . .	115
5.14	Time lags and PSD for the brief soft state of 2001 October, compared to those of other typical observations . . . . .	116
6.1	Correlations between the peak frequencies $\nu_1$ , $\nu_2$ , $\nu_3$ , and $\nu_4$ of the broad noise components . . . . .	121

## List of Tables

---

1.1	List of known BHXRBs and their mass functions . . . . .	24
1.1	continued . . . . .	25
1.2	The instruments on-board <i>RXTE</i> . . . . .	32
5.1	Energy bands and data modes of the Cyg X-1 monitoring . . . . .	93
5.2	Average values and standard deviations of the rms amplitudes, $\text{rms}_i$ , the peak frequencies, $\nu_i$ , and the frequency ratios, $\nu_i/\nu_j$ , for the four broad noise components ( $i, j = 1, \dots, 4$ ) . . . . .	100
A	Table of PSD fit results . . . . .	137

# CHAPTER 1

---

## **Black Hole X-Ray Binaries**

Black holes belong to the most fascinating astronomical objects we know. Work and creativity in many different areas have been stimulated by the prediction and discovery of these “gravitational monsters”: they are extremely important to test predictions of fundamental physical theories like those of general relativity or quantum mechanics under extreme conditions. They are also related to fundamental philosophical questions concerning the definition of time and space, the speculative existence of parallel universes, etc. Several books aimed at a larger audience have been published to illustrate the extraordinary properties of black holes (Hawking, 1988; Thorne, 1994; Novikov, 1995). Finally, black holes have found their way into many works of fiction, books as well as movies. But how were they discovered and what can actually be observed from a “black” hole? Answering this question is the aim of the first two sections of this introduction which are influenced by the books of Novikov (1995) and Shapiro & Teukolsky (1983). The remaining sections are dedicated to giving an overview of black hole binary sources and to introducing the scope of this work (Cygnus X-1, monitoring campaign, thesis outline). While there are different classes of black holes known or postulated (Active Galactic Nuclei, ultra-luminous X-ray sources, primordial black holes, isolated black holes, . . . ) this work concentrates on stellar mass black holes in binary systems.

### *1.1 History of Black Hole Research*

First ideas which later led to the prediction and and finally the discovery of black holes where already discussed in the 18th century. Independently, the concept of the black star was introduced by the British geologist Rev. John Michell in 1783 and the French mathematician and astronomer Pierre Laplace in 1795 (Michell, 1784; Laplace, 1795, 1799). Their reasoning was based on the Newtonian theory of gravitation. According to this theory, light is composed of particles which have a mass like ordinary matter. Thus, in order to leave the surface of a body, e.g., a star, the light particles must have a certain escape velocity. This velocity depends on the density  $\rho$  and the radius  $R$  of



the star:

$$v_F = R \cdot \sqrt{\frac{8}{3} \pi G \rho} \quad (1.1)$$

where  $G = 6.67259 \cdot 10^{-8} \text{ cm}^3/(\text{g s}^2)$  is the gravitational constant. For a star with the same density as the sun ( $1.41 \text{ g/cm}^3$ ) and a radius of  $\approx 500$  solar radii ( $R_\odot = 6.96 \cdot 10^{10} \text{ cm}$ ) or more, Laplace and Mitchell calculated that  $v_F$  would exceed the velocity of light. Such an object would thus be a black star. However, this is not the modern concept of a black hole, and it was forgotten together with the particle nature of light when in 1801 Thomas Young discovered the ability of light to interfere like waves.

Only in the 20th century the present theory of black holes was developed. With the discovery of quantum mechanics the wave/particle dualism of light became evident. Furthermore, it was realized that in the case of high gravitational forces the Newtonian theory has to be replaced by the theory of general relativity (GRT). Finally, the theory of special relativity postulated that  $c$  is the highest possible velocity and that therefore no information at all can leave from inside a black hole. In 1915 the German astronomer Karl Schwarzschild succeeded in solving the GRT equations for spherical, non-rotating bodies (Schwarzschild, 1916). A characteristic parameter of this solution is the so-called Schwarzschild-radius  $R_S$ , which is the radius for a body of a given mass at which the gravitational force on its surface becomes infinitely big:

$$R_S = \frac{2GM}{c^2} \sim 3 \text{ km} \frac{M}{M_\odot} \quad (1.2)$$

The new concept of black holes was born when in 1939 the US physicist Robert Oppenheimer calculated that a body which is compressed down to  $R_S$  collapses. After such a gravitational collapse only the gravitational field and the angular momentum are preserved. No surface is present anymore. But according to the GRT, a minimal orbit around a black hole can be defined that is still stable. For a non-rotating black hole, this innermost marginally stable circular orbit (ISCO) is found at  $3R_S$ .

It was also already known that during the final stages of stellar evolution high gravitational fields arise: when the nuclear fusion activity declines, the equilibrium between the thermal and gravitational forces is disturbed. The star contracts, ending as a white dwarf or, if the Chandrasekhar mass of  $\sim 1.4 M_\odot$  is exceeded, a supernova explosion occurs. The latter can have three different possible outcomes: the star can be completely destroyed, a neutron star can form if the remaining mass is below the stability limit for neutron stars of  $2\text{--}5 M_\odot$ , and for higher masses the collapse continues until a black hole is created. However, these theories were not established for a long time and black holes were not thought to exist apart from the theoretical thought

construct. That finally changed in the 1960s when several discoveries were made that shed new light on the universe: the measurement of the microwave background radiation in 1965, e.g., confirmed the big bang, and in 1967 the first radio pulsar, i.e., the first neutron star, was found. The search for black holes became an issue again. However, it was not clear at all in the beginning how and where to look for these exotic but “information swallowing” objects. The development of different ideas and thought models are described in detail by Novikov (1995).

The path that led to success was to look for the influence of the strong gravitational field of a black hole on the surrounding material. In the following section it will be shown that matter falling into the “gravitational well” of a black hole loses its potential energy in form of radiation, mainly in the X-ray regime. One possible scenario according to which a sufficient amount of matter can be supplied to produce an observable X-ray luminosity is a binary system where the companion star transfers mass to the black hole. Thus the search concentrated on X-ray binaries (XRBs). A dynamical mass measurement of the compact object’s mass in an XRB is difficult but in some cases possible: in these cases the optical component is bright and its spectrum can be measured. It only shows the absorption line system of the companion star which is displaying a Doppler shift due to the binary motion. Such a single-lined spectroscopic binary allows to use Kepler’s third law to derive the so-called mass function of the binary:

$$f(M_1, M_2, i) = \frac{(M_2 \sin i)^3}{(M_1 + M_2)^2} = \frac{Pv_1^3}{2\pi G} \quad (1.3)$$

If the binary period  $P$  as well as the radial velocity  $v_1$  can be measured from the optical spectrum, the mass function  $f(M_1, M_2, i)$  is known. Apart from depending on the mass of the compact object,  $M_2$ , it is also determined by the mass of the companion star,  $M_1$ , as well as by the system’s inclination with respect to the line of sight. In any case, the mass function represents a lower limit for the mass of the compact object which can be derived by setting  $M_1 = 0$  and  $i = 90^\circ$ . Table 1.1 on page 24 gives an overview of the known mass functions of black hole X-ray binaries (BHXRBS). Generally, better approximations than  $M_1 = 0$  (spectral class?) and  $i = 90^\circ$  (eclipses?) can be made, but nevertheless the estimate of  $M_2$  typically contains an uncertainty of a few solar masses<sup>1</sup>. The first dynamically measured X-ray binary mass function that led to a compact object mass in the black hole regime was derived in 1971 for the X-ray binary Cygnus X-1 (Murdin & Webster, 1971). Further information on this system is given in section 1.4.

---

<sup>1</sup>For the most accurately measured BHXRBS mass see Greiner, Cuby & McCaughrean (2001).

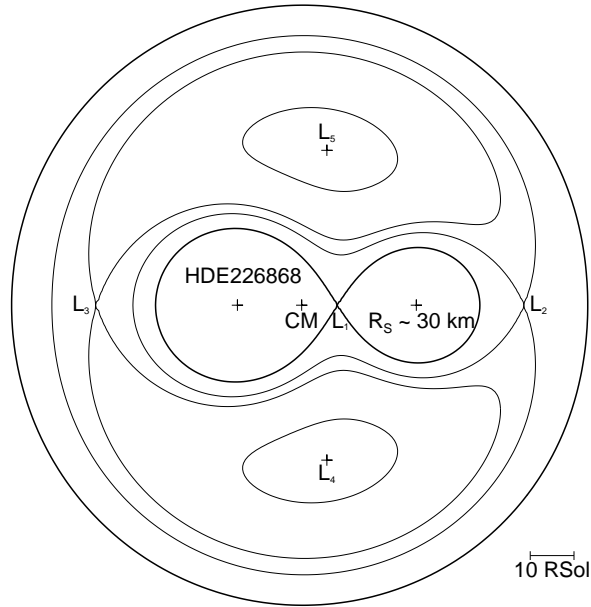


Figure 1.1: Equipotential lines of the Roche potential, Eq. (1.4), calculated for the system parameters of the HDE 226868/Cyg X-1 binary (as given by Herrero et al., 1995). Here the cross section of  $\Phi(\mathbf{r})$  through the binary plane is shown.

## 1.2 X-ray Emission from Accretion onto Black Holes

In this section the basic mechanisms for the mass transfer from the companion star to the black hole are introduced. In addition the emission of X-rays from the accreted material is explained in a principal way. Estimates and limits for the observable flux are given.

In order to understand the mass transfer in a binary system, the gravitational potential that characterizes such a system has to be taken into account. This potential has been theoretically derived for an idealized case by the French mathematician Edouard Roche in the 19th century. For two point masses  $M_1$  and  $M_2$  in circular Kepler orbits around their center of mass, it takes the following form, if calculated in coordinates co-rotating with the binary orbit and with their origin in the center of mass of the

system (Frank, King & Raine, 1992, page 48):

$$\Phi(\mathbf{r}) = -\frac{GM_1}{|\mathbf{r} - \mathbf{r}_1|} - \frac{GM_2}{|\mathbf{r} - \mathbf{r}_2|} - \frac{(\boldsymbol{\omega} \times \mathbf{r})^2}{2} \quad (1.4)$$

where:  $\mathbf{r}$ : position, for which the potential is calculated,  
 $\boldsymbol{\omega}$ : angular velocity in non-co-rotating coordinates,  
 $\mathbf{r}_1, \mathbf{r}_2$ : position of the two binary components.

Fig. 1.1 shows the equipotential lines of the Roche potential (corresponding to equipotential surfaces in the three dimensional case), calculated for two point masses of  $18 M_\odot$  and  $10 M_\odot$ . This example reflects the mass ratio of Cyg X-1. In reality the two binary components are of course spatially extended, however, in order to illustrate principal properties of the mass transfer in X-ray binaries the Roche approximation is adequate. As can be seen from the figure, each component defines its own potential well or ‘‘Roche Lobe’’ (innermost solid line), this being the surface within which a mass element is bound to one of the two components. There are several equilibrium locations in the potential, where no force is acting on a point mass (Lagrange points L1–L5). Especially, there is the saddle point L1 between the two components. If material from the donor star reaches this point possessing momentum in the outward direction, it can enter the Roche lobe of the compact component. A similar case can be made for matter crossing L2 inwards. There are three mechanisms known by which such a mass transfer can proceed:

- Wind accretion: In case that the donor star is of an early type, it usually has a strong stellar wind that can send matter into the Roche lobe of the black hole. This may either happen directly, via L1, or the stellar wind may loose its kinetic energy and angular momentum in the neighborhood of L2. Typical mass loss rates via a stellar wind are in the range of  $10^{-6} - 10^{-5} M_\odot/\text{a}$ , with an estimated 0.01 – 0.1% of that being transferred to the black hole (Frank, King & Raine, 1992).
- Roche lobe overflow accretion: If the companion star is also well ahead in its evolution, it may reach the advanced stage where the stellar radius increases. This increase can continue until the star fills its Roche lobe and mass transfer via L1 sets in. This evolution state is mainly displayed by low mass, i.e., late type stars. Typical mass transfer rates are  $10^{-11} - 10^{-8} M_\odot/\text{a}$  (Frank, King & Raine, 1992).
- Be-stars: There are binaries with a companion of Be type, i.e., it may produce a strong equatorial outflow of material which is then forming an extended disk around that star. If the compact object – a neutron star for all known Be X-ray binaries – passes through this disk on its usually eccentric orbit, mass is transferred.

After matter crosses into the Roche lobe of the compact object, it gathers in a disk-like structure in the binary plane. Due to the binary motion, the transferred material possesses an angular momentum according to which it assumes its orbit in the disk. Angular momentum transfer in the disk causes some of the material to move closer and closer to the black hole, until it crosses the ISCO radius and is accreted into the black hole. The detailed physical process by which the angular momentum is transferred is still unclear (see, however, page 48 for a possible model). On its way down the potential well of the black hole, the material loses its potential energy. A considerable fraction of that energy is heating the accretion disk, resulting in a disk luminosity that can be approximated by (Shapiro & Teukolsky, 1983, pages 394 and 439):

$$L_{\text{acc}} = 2\eta \frac{GM\dot{M}}{R_S} = \eta \dot{M} c^2 \quad (1.5)$$

where  $\eta = 0.057 - 0.42$ , depending on the angular momentum of the black hole. Assuming realistic values for the mass transfer rate  $\dot{M}$  and for  $\eta$ , a typical luminosity of  $\sim 10^{37}$  erg/s can be obtained for the accretion onto black hole in a binary system. A lower limit for the characteristic temperature/energy of the accretion disk can be derived if black body radiation and a black hole mass are assumed (in the following, the latter corresponds to  $R_S=30$  km):

$$kT_{\text{bb}}^4 = \frac{kL_{\text{acc}}}{4\pi R_S^2 \sigma_B} \sim 0.5 \text{ keV} \quad (1.6)$$

where  $\sigma_B = 5.67 \cdot 10^{-5} \text{ erg}/(\text{cm}^2 \text{ s K}^4)$  is the Stefan-Boltzmann constant. The exact spectral shape of the accretion disk emission is difficult to determine, but usually a multi-color disk black body with a temperature profile of  $T(r) \sim r^{-3/4}$  gives a good approximation of the observed disk spectrum (Mitsuda et al., 1984)<sup>2</sup>. Such a temperature profile is shown in Fig. 1.2 for realistic black hole X-ray binary parameters. Fig. 1.3 gives an artists view of an accretion disk, where the temperature profile is indicated by color coding. Note, that a maximum value exists for the X-ray flux produced by accretion. This limit is reached when the radiation pressure due to the X-ray luminosity equals the gravitational “pull” of the black hole. An estimate for this limit is given by the “Eddington luminosity” which is derived under the assumption of spherical accretion. In this case the equilibrium of forces is given by:

$$\frac{GMm_p}{r^2} = L_{\text{Edd}} \frac{\sigma_T}{4\pi cr^2} \quad (1.7)$$

---

<sup>2</sup>Further X-ray emission components will be discussed, e.g., in section 2.2.3.1.

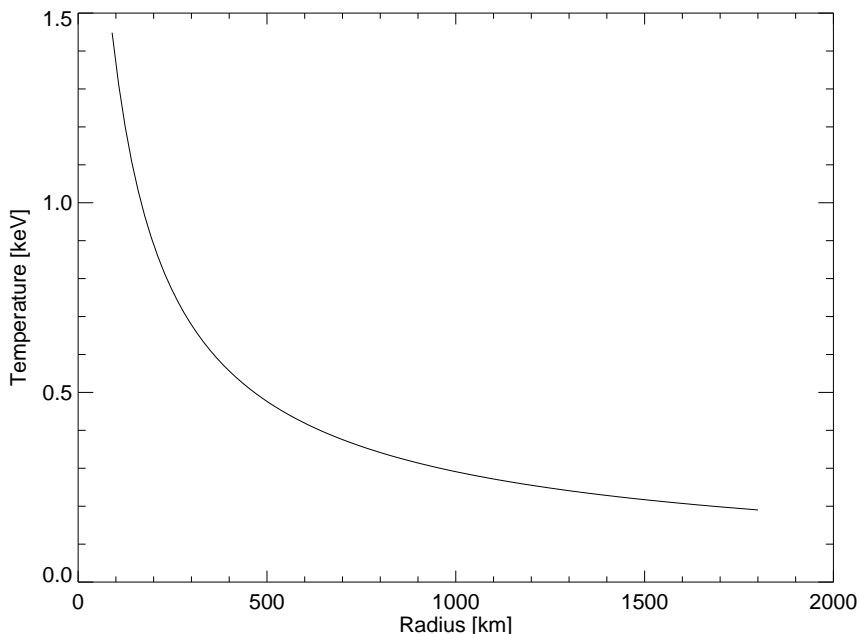


Figure 1.2: Temperature profile of a geometrically thin, optically thick accretion disk according to Eq. (5.45) of Frank, King & Raine (1992). Parameters typical for the accretion onto a black hole in an X-ray binary have been assumed, i.e.,  $M = 10 M_{\odot}$  for the mass of the black hole,  $L = 0.03 L_{\text{Edd}}$  (see Eq. 1.8),  $\eta = 0.1$  (see Eq. 1.5),  $\alpha = 0.1$  (see section 2.2.1).

where  $m_p = 1.67 \cdot 10^{-24}$  g is the proton mass and  $\sigma_T = 6.652 \cdot 10^{-25}$  cm the cross section for Thomson scattering. The Eddington luminosity for a black hole of mass  $M/M_{\odot}$  is thus:

$$L_{\text{Edd}} = \frac{4\pi c G M m_p}{\sigma_T} = 1.3 \cdot 10^{38} \left( \frac{M}{M_{\odot}} \right) \text{ erg/s} \quad (1.8)$$

### 1.3 Black Hole Source Sample and Classification

How many and which black hole binaries do we know today? How certain is the classification of the compact component as a black hole, i.e., how can the distinction

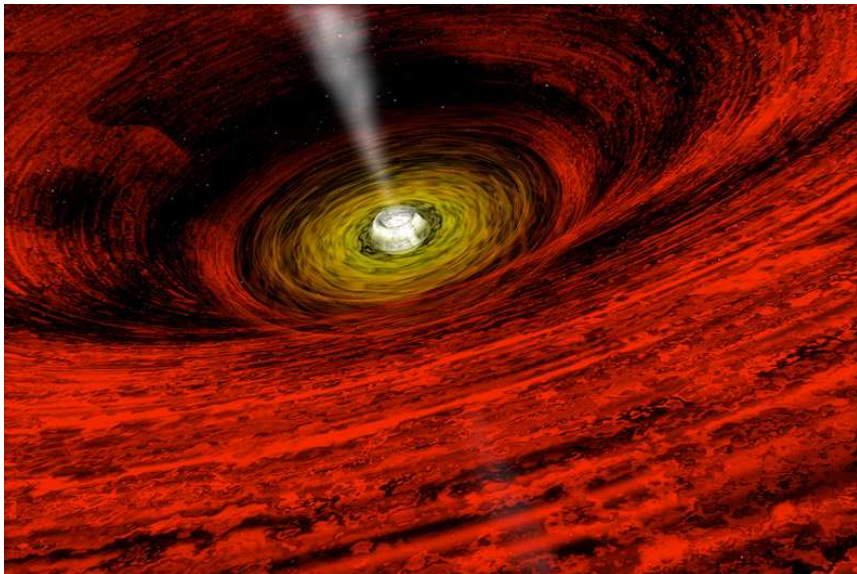


Figure 1.3: Drawing of an accretion disk around a black hole. An outflow (jet) is also included. Available at <http://antwrp.gsfc.nasa.gov/apod/ap010508.html>.

between a black hole and a neutron star be made? These questions have been asked since the first BHXRBS have been discovered in the 1970s. Concerning the level of certainty that a black hole is observed, there have always been two main classes: the objects for which it is possible to determine a dynamically measured mass according to Eq. (1.3) and those objects whose X-ray emission shows properties that were found to be typical for BHXRBS but not for neutron star X-ray binaries. Due to the indirect nature of the strongest observational evidence for the presence of a black hole in an X-ray binary, the dynamical mass measurement, it has long been common practice to call any BHXRBS a black hole “candidate”. However, since the typical characteristics of BHXRBS can be defined and sampled better and better with each new X-ray mission, the “candidate” has usually been dropped during the last several years. The basic observational requirements for the presence of a black hole are of course the absence of spin-pulsations and type I thermonuclear X-ray bursts, which would both indicate that a surface is present instead of a matter-permeable black hole event horizon. New results now allow to quantify long suspected differences of the spectral and temporal statistics between black hole and neutron star binaries: e.g., it has been reported that black hole binaries are generally under-luminous as compared to neutron star binaries (possibly due to advection of energy into the black holes, see, Kong

Table 1.1: List of known BHXRBS and their mass functions. The source list presented here is based on the works of Tanaka & Lewin (1995, Tan95), White & van Paradijs (1996, Whi96) and Fender & Kuulkers (2001, Fen01) as well as on recent IAU Circulars (IAUCs). The last column contains the references for the given mass function values. Generally newer values than those given by Whi96 are given here (Fen01 do not provide mass functions). In those cases where no mass function is given, it is assumed that none has been measured. This assumption is based on the tables by Whi96 and Tan95 and the fact that a very basic literature search did not produce a published mass function. For sources without measured mass function that are not mentioned in Whi96 and Tan95, a reference stating their black hole nature is given. For sources denoted by “?” the nature of their compact object – black hole, neutron star, white dwarf – is still a matter of debate. Sources marked by “N” where only recently discovered and are thus not firmly established BHXRBS yet.

Name	Other name	Mass function [ $M_{\odot}$ ]
XTE J0421+560 (?)	CI Cam	Bel99, Fen01
GRO J0422+32	V518 Per	Har99: $1.13 \pm 0.09$
LMC X-3		Sor01: 1.5
LMC X-1		Tan95: $0.14 \pm 0.05$
A 0620–00	V616 Mon	McC86: $2.91 \pm 0.08$
GRS 1009–45	XN Vel 93	Fil98: $3.17 \pm 0.12$
XTE J1118+480		McC01: $6.00 \pm 0.36$
GS 1124–68	GU Mus	Oro96: $3.01 \pm 0.15$
GS 1354–645	BW Cir, Cen X-2	Tan95, Whi96: –, Bro01
A 1524–62	TrA X-1	Tan95, Whi96: –
4U 1543–47		Oro98: $0.22 \pm 0.02$
XTE J1550–564		Oro02: $6.86 \pm 0.71$
4U 1630–47	GX 337+0, Nor X-1	Whi96: –
XTE J1650–500		Kal02: –
GRO J1655–40	V1033 Sco, XN Sco 94	Sha99: $2.73 \pm 0.09$
GX 339–4	4U 1658–48, V821 Ara	Tan95, Whi96: –
H 1705–25	V2107 Oph	$3.24 \pm 0.09$ , Fil97
GRS 1716–249	GRO J1719–24	Whi96: –
KS 1730–312		Whi96: –
GRS 1739–278		Fen01

et al., 2002) and that neutron star binaries show stronger aperiodic variability at very high frequencies, i.e.,  $> 100$  Hz (possibly due to neutron star surface boundary layers, Sunyaev & Revnivtsev, 2000). The  $\sim 40$  BHXRBS which are known to date are listed in Table 1.1 on page 24. This table is mainly based on the source lists given in Fender & Kuulkers (2001), White & van Paradijs (1996), and Tanaka & Lewin (1995), with additional information from recent IAU circulars.



Table 1.1: continued

Name	Other name	Mass function
1E 1740.7–2942	great annihil.	Tan95, Whi96: –
H 1743–32		Whi96: –
SLX 1746–331		Whi96: –
XTE J1748–288		IAUC 6937, Fen01
XTE J1755–324		IAUC 6710, 6726, Fen01
4U 1755–338		Whi96: –
GRS 1758–258		Whi96: –
SAX J1805.5–2031 (N)		IAUC 7843
SAX J1819.3–2525	V4641 Sgr	$2.74 \pm 0.12$ , Oro01
GS 1826–24		Tan95, Whi96: –
EXO 1846–031		Tan95, Whi96: –
XTE J1859+226		IAUC 7644: $7.4 \pm 1.1$
XTE J1901+014 (N)		IAUC 7880
XTE J1908+094 (N)		IAUC 7856, 7897
GRS 1915+105		Gre01: $9.5 \pm 3.0$
4U 1957+11 (?)	V1408 Aq	Tan95, Whi96: –
Cyg X-1		Gie82: $0.252 \pm 0.010$
GS 2000+25	QZ Vul	Har96: $5.01 \pm 0.12$
XTE J2012+381		Vas00, Fen01
GS 2023+338	V404 Cyg	Cas94: $6.07 \pm 0.05$
Cyg X-3 (?)	4U 2030+40	Sch96: 2.3

Bel99: Belloni et al. (1999), Gie82: Gies & Bolton (1982), Bro01: Brocksopp et al. (2001), Cas94: Casares & Charles (1994), Fen01: Fender & Kuulkers (2001), Fil97: Filippenko et al. (1997), Fil98: Filippenko et al. (1999), Gre02: Greiner, Cuby & McCaughrean (2001), Har96: Harlaftis, Horne & Filippenko (1996), Har99: Harlaftis et al. (1999), Kal02: Kalemci et al. (2002), McC86: McClintock & Remillard (1986), McC01: McClintock et al. (2001), Oro96: Orosz et al. (1996), Oro98: Orosz et al. (1998), Oro01: Orosz et al. (2001), Oro02: Orosz et al. (2002), Sch96: Schmutz, Geballe & Schild (1996), Sha99: Shahbaz et al. (1999), Sor01: Soria et al. (2001), Tan95: Tanaka & Lewin (1995), Vas00: Vasiliev, Trudolyubov & Revnivtsev (2000)

These BHXRBs can be further divided into two main groups, the persistently observable sources and those which are only easily visible during X-ray outbursts with a duration of typically several weeks to a few months. In some cases these so-called transients are known to be recurrent. There are five known persistent sources: Cygnus X-1 the first BHXRB identified and the prototype for typical BHXRB behavior (an overview is given in the next section), two sources in the Large Magellanic

Cloud, namely LMC X-1 and LMC X-3 (see chapter 2.1.5 and, e.g., Boyd et al., 2000; Nowak et al., 2001; Wilms et al., 2001), and two sources in the Galactic center region, GRS 1758–258 (see, e.g., Smith et al., 2001; Heindl & Smith, 2002) and 1E 1740.1–2942 (see, e.g., Mirabel et al., 1991; Smith et al., 1997). GX 339–4 (see, e.g., Wilms et al., 1999; Nowak, Wilms & Dove, 2002; Zdziarski, 1998) is showing X-ray activity more often than most transients, but since it has also off-times, it is not a persistent source. An overview of observations and system parameters of these bright and prominent sources as well as of several transients has, e.g., been given by Cowley (1992).

The physical distinction between the persistent and the transient sources is believed to lie mainly in the nature of the companion star delivering the material accreted by the compact object: in case of an early type donor (O- or B-star), a strong stellar wind is usually continually present and the X-ray emission is comparatively steady. These companions are also high mass stars, therefore the persistent BHXRBS are usually high mass X-ray binaries (HMXBs). If the donor is a late type star, however, accretion proceeds via Roche lobe overflow, following cycles when the companion is over- and underfilling the Roche lobe, i.e. of enhanced mass transfer (leading to X-ray outbursts) and no mass transfer (leading to X-ray quiescence) to the compact object. The transients are usually low mass X-ray binaries (LMXBs). HMXBs and LMXBs are thus classified according to the donor star, not the compact object. Note, that the companion star has not been identified for all known BHXRBS, especially for the transients, the low mass, i.e., low luminosity companions can be difficult to detect.

The majority of the BHXRBS are transient sources, a special and spectacular subclass being the so-called microquasars. While most BHXRBS are known to show radio emission at certain times, the sources originally called microquasars in analogy to the extragalactic radio quasars<sup>3</sup>, GRS 1915+105 and GRO J1655–40, show discrete ejections of blobs of radio emitting material with apparent superluminal motions.<sup>4</sup> The radio emission of BHXRBS is generally related to their different X-ray states. The characterization of these states is the main topic of this work and the key to a physical description of the accretion onto black holes. The black hole states are described in detail in chapter 2. They have also been used as a criterion to classify the ultra-luminous X-ray point sources (ULX) which are now discovered in other galaxies in ever greater numbers by the new sensitive imaging instruments (Kubota et al., 2001; Prestwich et al., 2001; Wu et al., 2002; Colbert & Ptak, 2002) as possible BHXRBS of a few  $100 M_{\odot}$ . However, the ULXs can only now be studied in detail

<sup>3</sup>Active Galactic Nuclei which are harboring black holes of typically  $10^6 - 10^8 M_{\odot}$  and which can have large, structured radio jets.

<sup>4</sup>While the excess of the speed of light can be explained by a geometrical effect, the material is nevertheless moving at relativistic velocities of several tenths of the speed of light.

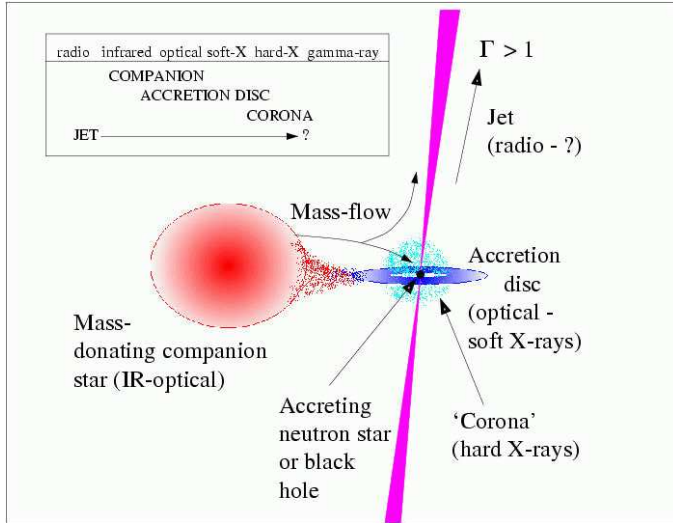


Figure 1.4: Illustration of the basic components of the HDE 226868/Cyg X-1 X-ray binary system (Fender, 2001). The energy regime that characterizes each emission component is indicated. Note that the spatial extensions are not to scale: while the companion star has a radius of approximately  $17 R_{\odot}$ , the radius of the corona is of the order of 500 km, and the Schwarzschild-radius characterizing the extension of the black hole is 30 km.  $\Gamma$  is the Lorentz factor associated with the bulk motion of the outflow.

and are not topic of this work (they are also not included in Table 1.1).

## 1.4 Cygnus X-1

The observational properties of the binary components of Cyg X-1 have always been the test case for models of black hole accretion. Many reviewing as well as specialized works exist, presenting the many observations from many instruments in many wavelength regimes, and/or concentrating on mathematical or physical modeling. Early reviews have, e.g., been given by Oda (1977) and Liang & Nolan (1984). Reviews containing a table of the Cyg X-1 system parameters can, e.g., be found in Pottschmidt (1997) or Nowak et al. (1999a). Here I summarize the basic properties again in an even more compact manner than in the given literature, based on the current picture of the system components as displayed in Fig. 1.4. Please note that several of the system parameters are only known to within large uncertainties (e.g., the distance or the masses), even for this bright and well-studied system:

- The X-ray source Cyg X-1 has been discovered from observations performed during a rocket flight in 1964 (Bowyer et al., 1965).
- Its identification with the spectroscopic single-lined binary HDE 226868 in 1971 was possible because of an outburst of a radio source, whose location could be identified as being consistent with HDE 226828, and a simultaneous decline in the X-ray luminosity of Cyg-X-1, the latter decline measured by the *Uhuru* satellite (Hjellming & Wade, 1971; Braes & Miley, 1971). This was the first “black hole state transition” ever observed.
- The optical identification allowed a dynamical mass determination of the binary components and led to the classification of the compact object as a possible black hole (Murdin & Webster, 1971; Wade & Hjellming, 1972; Bolton, 1972), although the mass function (eq. 1.3) amounts only to  $0.252(10)M_{\odot}$  (Gies & Bolton, 1982). The most recent mass estimate gives  $10M_{\odot}$  for the compact object (Herrero et al., 1995).
- The binary is to be found at a right ascension of  $19^h58^m21^s.676$  and a declination of  $+35^{\circ}12'05''.78$  (J2000.0), i.e., at a galactic longitude and latitude of  $71.33$  and  $+3.07$ , respectively (ESA, 1997).
- Its distance has been measured to be  $2.5(3)$  kpc (Ninkov, Walker & Yang, 1987b).
- The whole system has a proper motion of  $93.4 \pm 17.8$  km/s, measured during the *HIPPARCOS* mission (Chevalier & Ilovaisky, 1998). Such a high value is consistent with the expectation from binary evolution models.
- From radial velocity measurements, the system ephemeris can be given as  $\text{JD } 2441874.707(9) + N \times 5.599829(16) \text{ d}$  (Brocksopp et al., 1999b, see also Gies et al. 2002) and is known to be in good agreement with the photometric ephemeris (Brocksopp et al., 1999b; Voloshina, Lyuty & Tarasov, 1997).
- The mass donor star is of type O9.7 Iab, its mass has been determined from the optical spectrum to amount to  $\sim 18M_{\odot}$  (Herrero et al., 1995).
- The star dominates the emission of the system in the IR and optical regimes:  $L_{\text{opt}} \sim 10^{5.4}L_{\odot}$  (Herrero et al., 1995). Its apparent luminosity is  $m_V = 8.91$  mag (Lutz & Lutz, 1972).
- The donor probably fills its Roche lobe (Herrero et al., 1995). The stellar wind is revealed by emission components observed in some optical line profiles of HDE 226868 (see, e.g., Ninkov, Walker & Yang, 1987a).

- Following this picture, the accretion proceeds via a so-called focused stellar wind (Friend & Castor, 1982; Gies & Bolton, 1986b). The mass loss rate of the donor star has been estimated to be  $\sim 3 \times 10^{-6} M_{\odot}/a$  (Herrero et al., 1995), and about 0.01 – 0.1% of that mass are believed to be accreted onto the black hole via the focused wind.
- A signature of the accretion stream can, e.g., be seen in the emission component of the optical He II  $\lambda 4686 \text{ \AA}$  line, which has a phase shift of  $134^{\circ}$  relative to the binary phase (Ninkov, Walker & Yang, 1987a).
- Another signature of the accretion stream are the dips in the soft X-ray flux that are often observed when the black hole is at superior conjunction (see, e.g., Kitamoto et al., 1984; Bałucińska-Church et al., 1997). Although the inclination of the system is not well constrained, there are indications that it lies around  $35^{\circ}$  (Gies & Bolton, 1986a). At superior conjunction, the X-ray emission from the accretion region around the black hole is thus absorbed in the accretion stream. This also results in the 5.6 d orbital period being observable in the soft X-ray flux (Brocksopp et al., 1999a; Wen et al., 1999).
- The material transferred into the Roche lobe of the black hole forms an accretion disk where the initial orbit corresponds to the angular momentum of the material. Angular momentum transfer in the disk allows the material to move further inward.
- The accretion onto this black hole produces an average X-ray luminosity of  $4 \times 10^{37} \text{ erg/s}$ . Emission from a harder ( $\sim 100 \text{ keV}$ ) and a softer ( $\sim 1 \text{ keV}$ ) X-ray source are observed. They are attributed to two accretion components, the accretion disk and a hot plasma, the corona. The detailed X-ray spectrum, its underlying physical processes, as well as the spectral states are described in the next chapter.
- Strong short term variability on all time scales  $< 1000 \text{ s}$  is present in the X-ray emission, its description is the main diagnostic used in this work.
- Outside of soft X-ray flaring, steady radio emission with an average flux of 15 mJy at 15 GHz is observed. It also displays the 5.6 d orbital modulation (Pooley, Fender & Brocksopp, 1999). This can be explained if some of the material near the black hole is leaving the accretion region again in form of an outflow (see, e.g., Fender, 2001; Stirling et al., 2001). It still has to be determined how extended the wavelength regime of this component is.

- Variability is present on several time scales  $> 30$  d in the radio, optical, and X-ray fluxes. However, those are no strict periodicities. Period search methods usually produce many aliases, hiding the primary time scale, if there is one.
- The most firmly established long term time scale has long been a  $\sim 294$  d period that had been observed in the optical (Kemp, 1983; Kemp et al., 1987) and X-ray flux (Priedhorsky, Terrell & Holt, 1983).
- More recent measurements find the 150 d signature to be the primary period in the soft X-rays (Pooley, Fender & Brocksopp, 1999). This period is also seen in the radio flux (Pooley, Fender & Brocksopp, 1999), a strong indication that the accretion disk and the outflow are coupled by a precessing motion on that time scale (Brocksopp et al., 1999a).

Despite this wealth of knowledge about the system, many questions are still open. Pointed multi-wavelength observations as presented in this work, i.e., performed on a regular basis and covering several times the longest system time scales, have never been done before. As will be shown, they especially allow to constrain the stability of the so-called canonical hard X-ray emission state – which is also the steady radio emission state as well as the strong short term variability state. Thus they help to better understand the interdependencies between the different accretion components. The Cyg X-1 monitoring observations analyzed for this work are described in the following section.

### 1.5 The Monitoring Campaign of Cygnus X-1 from 1998 to 2001

Dedicated monitoring of Cyg X-1 started in 1998 and is still ongoing in 2002. The main observatories used are NASA's Rossi X-ray Timing Explorer (*RXTE*) and the Ryle radio telescope in Cambridge, UK. The *RXTE* satellite has been launched in 1995 December. It carries two pointing instruments, the Proportional Counter Array (*PCA*, Jahoda et al., 1996) and the High Energy X-ray Timing Experiment (*HEXTE*, Rothschild et al., 1998), as well as the All Sky Monitor (*ASM*, Levine et al., 1996). Basic characteristics of these instruments are summarized in Table 1.2<sup>5</sup>.

Although the set-up of the monitoring observations will be apparent in other parts of this work, I will provide a brief summary here: In 1998 the X-ray monitoring campaign was initiated by W.A. Heindl (UC San Diego, USA) and D.M. Smith (UC Berkeley, USA): weekly 3 ks exposures with *RXTE* were performed. Already beginning shortly after the end of the 1996 soft state episode, G.G. Pooley (Cambridge,

---

<sup>5</sup>Note that aging effects exist, e.g., the damage to PCU0 of the PCA, which are not taken into account in the table.

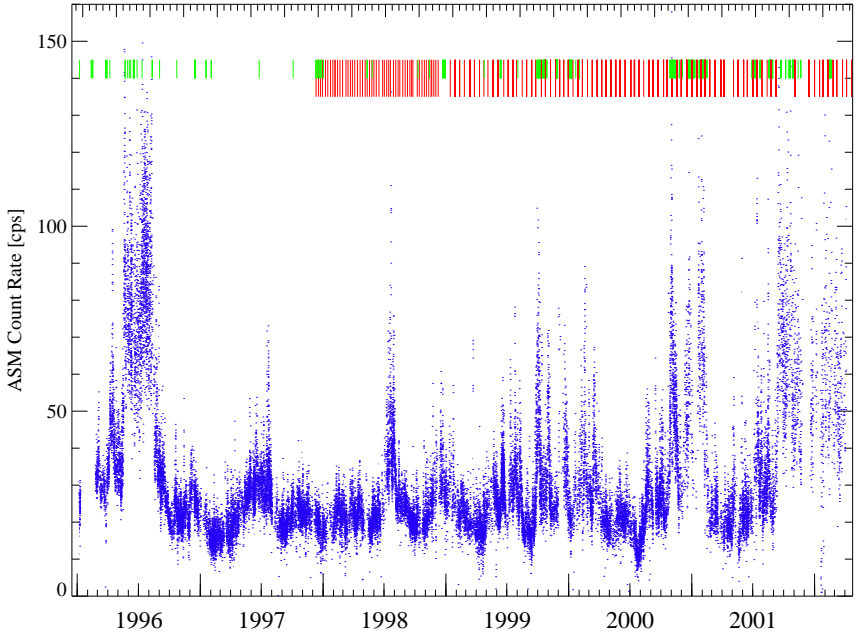


Figure 1.5: The lightcurve of Cyg X-1 as measured from 1996 to 2002 by the *RXTE*/*ASM* in the 2–12 keV energy band, averaged over 1 d bins. The soft state in 1996 is clearly apparent. From this plot it is clear that the behavior of the source is more complex than the usually assumed switching between two well defined soft X-ray flux states. The pointed *RXTE* monitoring observations of our campaign are indicated by the longer (red) tickmarks, all other *RXTE* pointings performed of Cyg X-1 are indicated by the shorter (green) tickmarks.

UK) had been performing daily radio flux measurements of Cyg X-1 using the Ryle telescope. Lightcurves of the 15 GHz flux with a time resolution of 8 s were/are obtained. Therefore, quasi-simultaneous X-ray and radio pointings exist for 1998. From 1999 on, strictly simultaneous radio observations were performed with all *RXTE* monitoring observations, in addition to the daily radio lightcurves. Nominally, the *RXTE* exposures have been increased to 10 ks in 1999 – in order to achieve a high signal-to-noise ratio for higher order timing statistics also – and to 20 ks from 2000 onwards – in order to compensate for *PCA* aging effects that require resting periods for certain PCUs<sup>6</sup>. Several optical spectra have also been taken simultaneously with *RXTE* observations. However, the optical data as well as the evaluation of the radio

<sup>6</sup>However, the actual exposure is only rarely longer than 10 ks due to scheduling limitations

Table 1.2: Characteristics of the instruments on-board *RXTE*.

instrument	<i>ASM</i>
type of detector	3 Scanning Snow Cameras (SSCs) with proportional counters
energy range (nominal)	2–10 keV
max temp. resolution	90 min, 80% of the sky
energy resolution	count rates in three bands are available
effective area	90 cm <sup>2</sup>
background determination	coded mask deconvolution
spatial resolution	3' × 15'
instrument	<i>PCA</i>
type of detector	5 Proportional Counter Units (PCUs)
energy range (nominal)	2–60 keV
energy range (recommended)	2–30 keV
max temp. resolution	1 μs
energy resolution	< 18% at 6 keV
effective area	6500 cm <sup>2</sup>
background determination	theoretical model + particle counter
spatial resolution	collimator with 1° FWHM
instrument	<i>HEXTE</i>
type of detector	2 clusters of 4 NaI/CsI scintillation quadrants
energy range (nominal)	15–250 keV
energy range (recommended)	25–250 keV
max temp. resolution	8 μs
energy resolution	15% at 60 keV
effective area	2 × 800 cm <sup>2</sup>
background determination	1 cluster, alternating
spatial resolution	collimator with 1° FWHM

emission on time scales  $< 1$  d are not presented here (see section 6.4 for future plans). The focus lies on a detailed analysis of the high time resolution data provided by the *RXTE/PCA* instrument for all monitoring pointings, on the background of the daily Ryle and *ASM* monitoring of the source. An overview of the overall source behavior from 1996 to 2002 as characterized by the *ASM* count rates and the schedule of pointed observations is given in Fig. 1.5.



## 1.6 Outline of this Thesis

Chapter 2 is dedicated to presenting an overview of the emission states of black hole X-ray binaries. I review the standard picture of black hole states that has emerged in recent years. The states review is divided into two parts: one concentrating on summarizing the observational properties (section 2.1) and the other on introducing the physical models that are discussed to explain the observed emission of these sources (section 2.2).

In my opinion, three different types of observations – apart from high time & spectral resolution X-ray pointings – are the main reason that this unification could be formed: (1) Combined X-ray and radio observations of BHXRBs (Figs 2.4, 5.3), (2) high energy observations that also extend into the  $\gamma$ -ray regime (100 keV–10 MeV, Fig. 2.5), and (3) last but not least, monitoring observations. The outbursts of transient sources are generally more dynamic and dramatic than the behavior of persistent sources. Most monitoring campaigns concentrate on those outbursts. They typically encompass up to  $\sim 50$  pointings over several weeks. To my knowledge, all five known persistent BHCs have first been monitored in detail with *RXTE*, allowing to also evaluate the long term stability of the states on time scales of years: GRS 1758–258 and 1E 1740.7–2942 (Smith et al., 2001; Smith, Heindl & Swank, 2002), LMC X-1 and LMC X-3 (Boyd et al., 2000; Wilms et al., 2001), and Cyg X-1 (see this work and the corresponding references). While all these sources fit into the states scheme, their individual long term behavior is very different (compare, e.g., LMC X-3, section 2.1.5, and Cyg X-1, Fig. 5.3).

In chapter 3 the mathematical methods are described which were used to characterize the short term variability as found in the Cyg X-1 *RXTE* monitoring observations. This includes the calculation of the Fourier transforms of the high resolution lightcurves in several energy bands, as well as the power spectra, coherence functions, and frequency dependent time lags. First, the mathematical formulation of these quantities is developed, including their uncertainties and noise components. Then, examples calculated for one of the Cyg X-1 observations are presented. They were obtained with IDL tools specifically developed as part of this thesis for analyzing *RXTE* monitoring observations.

The chapters 4 and 5 contain the results of analyzing  $\sim 130$  Cyg X-1 monitoring observations plus additional public *RXTE* observations performed during the well known 1996 soft state. Here, the emphasis lies on presenting the different timing properties and on modeling the power spectra, but modeling of the energy spectra and an evaluation of the radio flux evolution are also included. The main objective of chapter 4 is to study the temporal evolution of the frequency dependent time lags between the variability structures in different energy bands. Among other results this leads to the definition of “failed” state transitions. Chapter 5 concentrates on mod-

eling the power spectra in terms of discrete Lorentzian components, showing for the first time that such a description is possible for all Cyg X-1 hard state observations in a consistent way. The structure of each of those chapters is based on a publication, Pottschmidt et al. (2000) and Pottschmidt et al. (2002) for chapter 4 and 5, respectively. Therefore, those chapters are written in a self-contained form, causing the occurrence of some repeated arguments.

The remaining chapter 6 first summarizes the results. In order to be able to compare the power spectra fits with similar recent studies on other X-ray binaries, correlations between the Lorentzian peak frequencies are then presented and discussed. A physical accretion scenario which can be considered as a possible model for explaining the results of the different analyses is proposed. In this context both approaches – studying the lags as well as modeling the power spectra – indicate the vertical expansion of the accretion region during state transitions, failed and successful ones. Finally, an outlook on planned future work involving data from the Cyg X-1 monitoring campaign is given.

## CHAPTER 2

---

### The States of BHXRBs

#### 2.1 *Observational Properties and Basic Model Components*

The possibility to classify galactic black hole X-ray binaries (BHXRBs) according to several distinct emission states is well known since the beginning of the 1990s (Tanaka & Lewin, 1995; van der Klis, 1995). It has been well documented for many sources, especially since X-ray missions like *CGRO* (1991–2000, 30 keV–30 GeV), *RXTE* (1995–today, 2–250 keV, several  $\mu$ s time resolution), and *BeppoSAX* (1996–today, 0.1–300 keV, 20–500  $\mu$ s time resolution) allow X-ray observations with broad band spectral coverage and/or high time resolution. These states can be distinguished due to their X-ray spectra (which was the initial distinction), their short term X-ray variability, their  $\gamma$ -ray spectra, and also due to their radio emission. Most black hole binaries show transitions between different states. Overviews presenting the phenomenology of black hole states are for example given by Tanaka & Lewin (1995), van der Klis (1995), Remillard (2001), Fender (2001), and Belloni (2001). In this section I summarize this phenomenology and introduce the basic physical model components that are believed to be responsible for the different emission states. In principle all states are built up from two different X-ray emission components – soft black body radiation and a harder component showing a power law spectrum – which dominate in the soft and hard state, respectively. In this sense the hard and the soft state are the two fundamental black hole states<sup>1</sup>.

The states are commonly classified according to their broad band spectra and their aperiodic short term variability on time scales from 0.001 s to 1000 s. The former is usually given as photon number measured per area-, time-, and energy-interval at a

---

<sup>1</sup>The original expressions ‘low’ and ‘high’ state for the hard and soft state, respectively, had been defined in the soft energy band of 2–10 keV, the most sensitive energy band of earlier X-ray missions. Since then it has become clear that ‘hard’ and ‘soft’ state are more fitting expressions, since for some sources there is no big change in bolometric luminosity between both states (< 15% for Cyg X-1; Zhang et al., 1997a, see, however, McConnell et al. 2002)

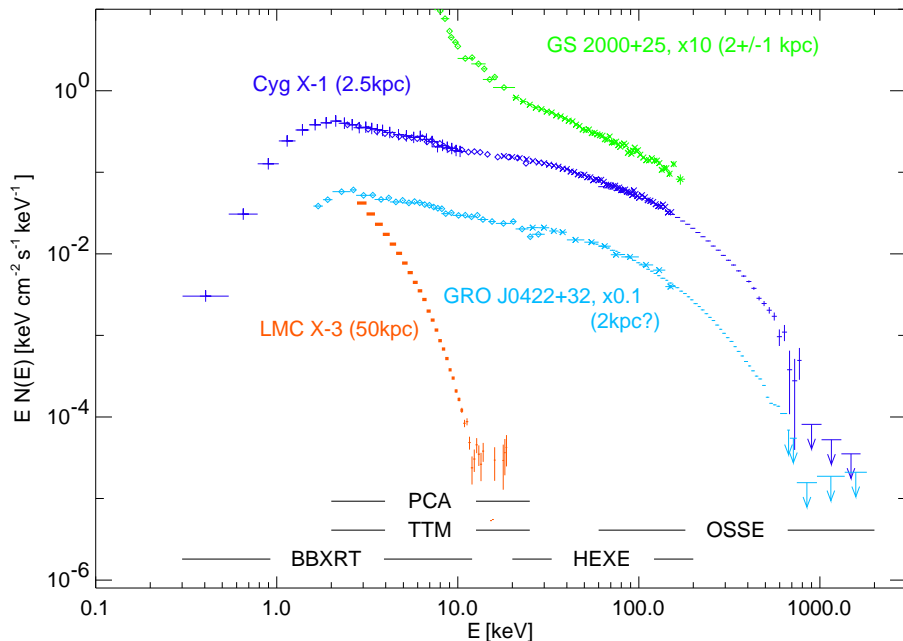


Figure 2.1: Typical examples of measured BHXR broad band energy spectra. The instruments which performed the observations are indicated in the plot. During the measurements Cyg X-1 and GRO J0422+32 displayed a hard state spectrum, LMC X-3 a soft state spectrum, and GS 2000+25 a very high state spectrum. Plot courtesy J. Wilms.

certain photon energy. Typical measured BHXR spectra are shown in Fig. 2.1. The latter is often described in terms of the power spectral density (PSD). The PSD is a Fourier frequency dependent quantity which gives the root mean square variability, rms, of the measured lightcurve at a given Fourier frequency normalized to the average observed count rate (= relative rms amplitude). It will be described in detail in section 3.2. Typical measured BHXR PSDs are shown in Fig. 2.2. Fig. 3.3 displays a typical PSD measured for Cyg X-1, and in chapter 5 many PSDs from our Cyg X-1 monitoring campaign are presented and discussed.

### 2.1.1 The Hard State

In the hard state the X-ray spectrum of BHXRBS is dominated by a hard emission component which can be described with an exponentially cut-off power law (see Cyg X-1 and GRO J0422+32 spectra in Fig. 2.1). The power law index  $\Gamma$  is typi-

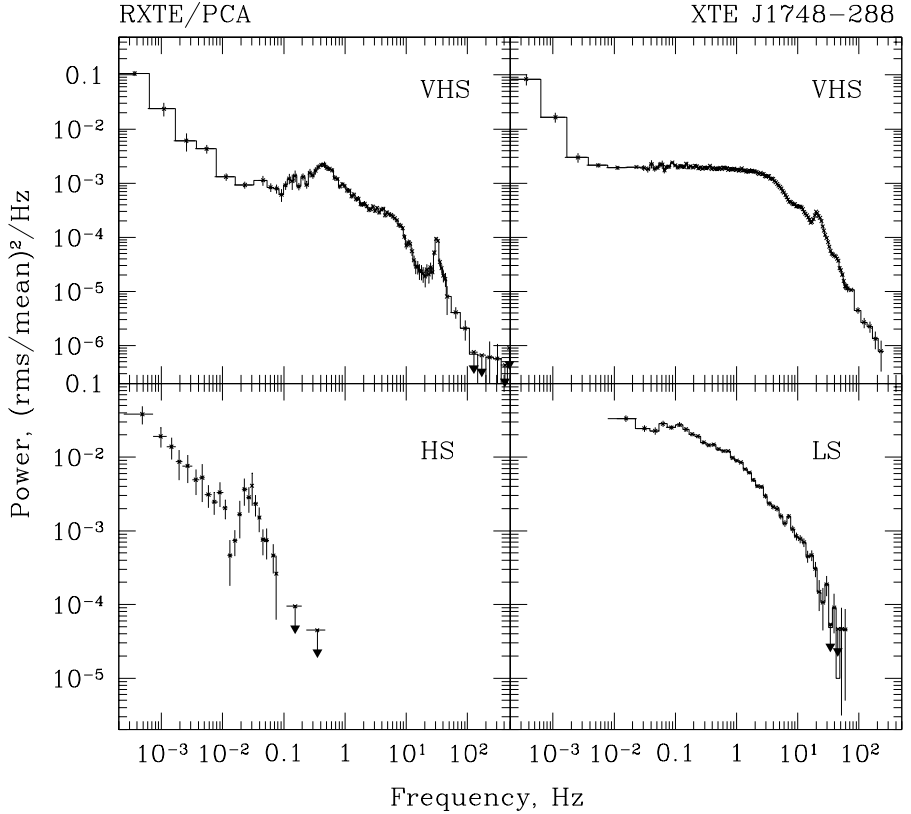


Figure 2.2: Typical examples of measured BHRB power spectra as observed with *RXTE* during the 1998 outburst of the transient XTE J1748–288 (Revnitsev, Trudolyubov & Borozdin, 2000, Fig. 6). The source developed from the very high state (VHS) over the soft/high state (HS) to the hard/low state (LS).

cally  $\sim 1.7$  and the cutoff energy lies around 150 keV. This component is associated with strong short term variability on time scales below 100 s (see lower right panel of Fig. 2.2). Its relative rms amplitude is typically around 35%. The PSD of this hard state noise is characterized by a flat top up to  $\sim 0.1$  Hz and a power law decline towards higher frequencies ( $\sim f^{-1.5}$ ). The hard state energy spectrum can physically be modeled by thermal Comptonization (page 51 and Fig. 2.15) of cool seed photons ( $kT_{\text{bb}} \sim 1$  keV) in a hot electron plasma (“corona”,  $kT_e \sim 150$  keV): The seed photons are believed to be produced in a standard accretion disk (section 2.2.1) and

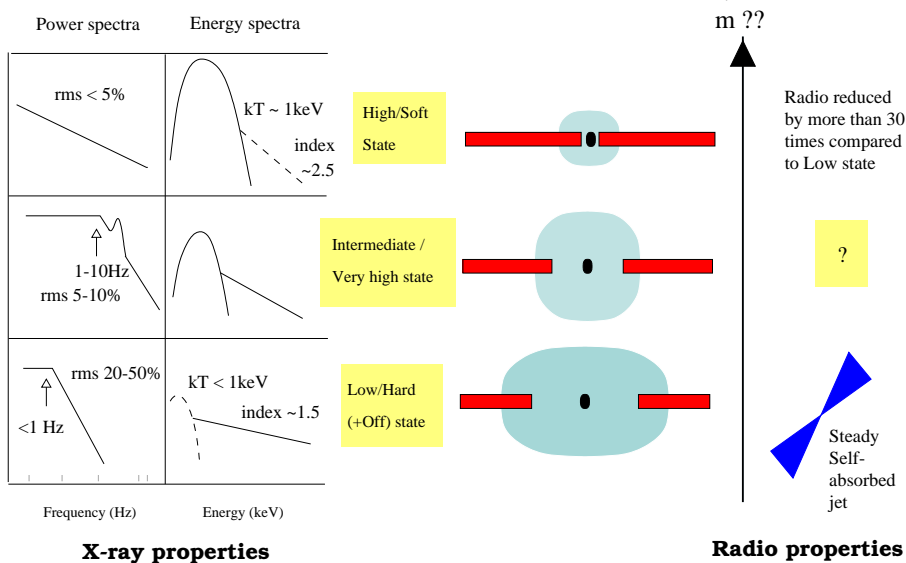


Figure 2.3: The canonical BHXR states (Fender, 2001, Fig. 4). **Left:** Typical X-ray properties. **Middle:** Basic physical components present in each state. **Right:** Typical radio emission properties.

can sometimes be detected in hard state spectra as soft excess black body emission around 1 keV. In most models the accretion disk is disrupted at a characteristic transition radius by the hot plasma (“sphere+disk” geometry, page 54) in which the seed photons are upscattered via inverse Compton collisions with the hot electrons to produce the observed power law energy spectrum. Reprocessing features due to Comptonized radiation that is intercepted by the accretion disk again can often be detected, i.e., an iron  $K\alpha$  fluorescence line at  $\sim 6.4$  keV and Compton reflected emission with maximum flux around 30 keV (page 57 and Fig. 2.17). Recently a positive correlation between the amount of reprocessed emission and the softness of the spectrum – the so-called  $R - \Gamma$  correlation – has been discovered in Active Galactic Nuclei (AGN) as well as in BHXRBs (Zdziarski, Lubiński & Smith, 1999; Gilfanov, Churazov & Revnivtsev, 1999), placing further constraints on the accretion geometry. These canonical X-ray properties of the hard state as well as the basic model components are summarized in the lower part of Fig. 2.3. In addition, the steady, optically thick (= flat spectrum) radio emission that is observed in the hard state indicates the presence of an outflow from the corona which is emitting synchrotron radiation at radio wavelengths (section 2.2.5).

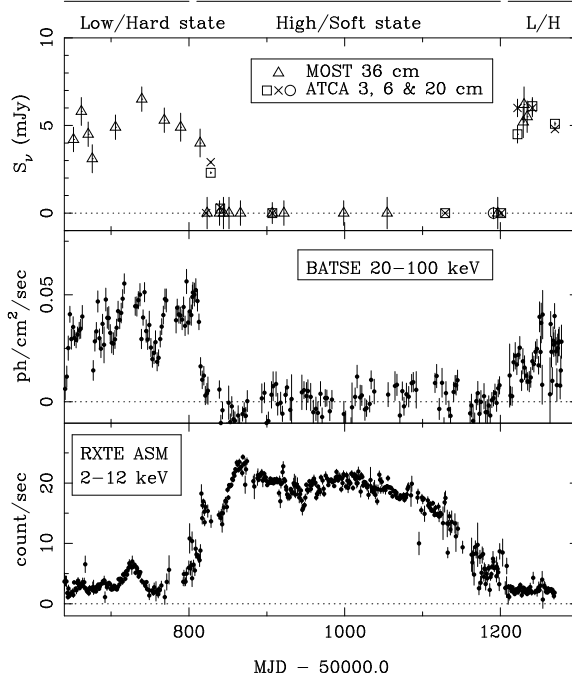


Figure 2.4: Multi-wavelength observations covering the 1998 soft state of GX 339–4 (Fender et al., 1999, Fig. 1). **Top:** Radio lightcurve measured at the indicated wavelengths. **Middle:** *CGRO/BATSE* 20–100 keV hard X-ray lightcurve. **Bottom:** *RXTE/ASM* 2–12 keV soft X-ray lightcurve.

### 2.1.2 The Soft State

In the soft state thermal emission from the accretion disk dominates the X-ray spectrum (see LMC X-3 spectrum in Fig. 2.1, and Cyg X-1 spectrum in Fig. 2.5). It is usually well modeled as a “multi-color disk black body” (Mitsuda et al., 1984), i.e., black body radiation with a radius dependent temperature profile  $T(r) \sim r^{-3/4}$  (Fig. 1.2). The short term variability associated with this emission component is generally less strong than that of the hard state, it can be as low as a few percent relative rms amplitude, however, it can also lie only a few percent below the hard state rms value (as is the case for Cyg X-1, see chapter 5 and Churazov, Gilfanov & Revnivtsev, 2001). The typical soft state power spectrum shows an  $f^{-1}$  power law extending down to below 0.001 Hz (see lower left panel of Fig. 2.2). If present, the hard spectral component is much weaker and steeper ( $\Gamma \sim 2.5$ ) than in the hard state. Therefore, the

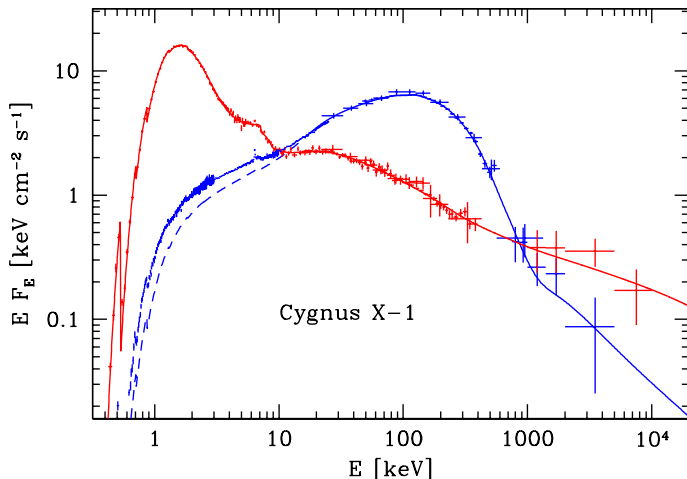


Figure 2.5: Cyg X-1 spectra extending into the MeV regime (McConnell et al., 2002, Fig. 9). Data are from *BeppoSAX* and *CGRO*, *egpair* models (page 56) are fitted (solid curves). For details on the data and models see McConnell et al. (2002). Dashed curve: fitting *CGRO* data only.

corona is thought to be absent or at least considerably weaker. This is consistent with the fact that the radio outflow, which is believed to be anchored in the corona, is also absent or considerably reduced (Fig. 2.4 and chapter 5). The whole soft state picture is summarized in the upper part of Fig. 2.3. One additional difference between the two fundamental states can probably be found in the spectra of even higher energies as *CGRO/OSSE* (Gierliński et al., 1997, 1999) and *CGRO/COMPTEL* (McConnell et al., 2002, and therein, see also Fig. 2.5) observations of Cyg X-1 indicate: While the high-energy cutoff observed in the hard state extends out to  $\gamma$ -ray energies, with a probable break at  $\sim 1$  MeV, the soft state power law does not show any cutoff, resulting in significant emission up to 10 MeV. This high-energy emission could, e.g., be due to inverse Compton scattering from non-thermal electrons, i.e., another accretion model component of electrons with a power law instead of a Maxwellian energy distribution (page 56).

### 2.1.3 Intermediate / Very High State, Transients, Microquasars

In the intermediate state as well as in the very high state both spectral components – the accretion disk black body as well as the Comptonization power law – are present in comparable strength, characterized by parameters that are intermediate between



those of the hard and the soft state (see GS 2000+25 spectrum in Fig. 2.1 and upper panels in Fig. 2.2). In both cases the PSD is flat-topped as in the hard state but with an increased break frequency of a few Hz and low frequency noise below  $10^{-3}$  Hz. Quasi-periodic oscillations (QPOs) which manifest themselves as narrow but visibly broadened peaks in the PSD are preferentially present during the intermediate and the very high state ( $Q \sim f_{\text{center}}/f_{\text{FWHM}}$  is typically of  $\sim 20$ ). The intermediate state is often observed as a “transitional state” between the hard and soft state (see chapter 5 and Belloni et al., 1996) and can be accompanied by flaring, optically thin radio emission (Corbel et al., 2000, and therein). The latter is generally attributed to the destruction/construction of the corona and can be explained in terms of discrete ejections of material (Fig. 2.7), even though this is usually not resolved in the radio images (see, e.g., Cyg X-1, Stirling et al., 2001). The middle part of Fig. 2.3 summarizes the described intermediate state / very high state properties.

It has been observed that the low/hard state corresponds to a few percent of the Eddington accretion rate,  $L_{\text{Edd}}$  and that for higher accretion rate the corona is unstable (Nowak, 1995). In the advection dominated accretion flow (ADAF, section 2.2.4) models, where the states depend only on the mass transfer rate  $\dot{M}$ , the low/hard state is also to be found at about 5% of  $L_{\text{Edd}}$ , developing into the intermediate state for higher  $\dot{M}$ , followed by the high/soft state at around 20%  $L_{\text{Edd}}$ . In this picture the corona becomes strong again for even higher accretion rates, and thus the very high state develops. This  $\dot{M}$ -dependent sequence of states is shown in Fig. 2.6. During their typically a few months long outbursts, transient BHXRBs evolve roughly according to this sequence, starting with a fast rise from quiescence (see next section) to the very high state, followed by a slower decay – roughly exponential in time – through the other states until quiescence is reached again (see, e.g., Revnivtsev, Trudolyubov & Borozdin, 2000; Frontera et al., 2001; Kalemci et al., 2001; Nowak, Wilms & Dove, 2002).

A special class of BHXRBs are the so-called microquasars, which display strong relativistic radio jets and sometimes even discrete ejections of radio-emitting material with apparent superluminal motion (e.g., Mirabel & Rodríguez, 1998, 1999; Fender, 2001). Fig. 2.7 shows radio images of the microquasar GRS 1915+105, the most prominent example of this source class (e.g., Mirabel & Rodríguez, 1994; Harmon et al., 1997; Mirabel et al., 1998; Eikenberry et al., 1998; Fender et al., 1999). For microquasars the canonical black hole states can be expected to be disrupted due to the strong outflow / ejections (Belloni et al., 1998). Indeed, they display a wealth of often QPO-rich “sub-states” with most of them probably related to the very high  $\dot{M}$  state, i.e., the very high state (Greiner, Morgan & Remillard, 1996; Munro, Morgan & Remillard, 1999; Belloni et al., 2000; Homan et al., 2001).

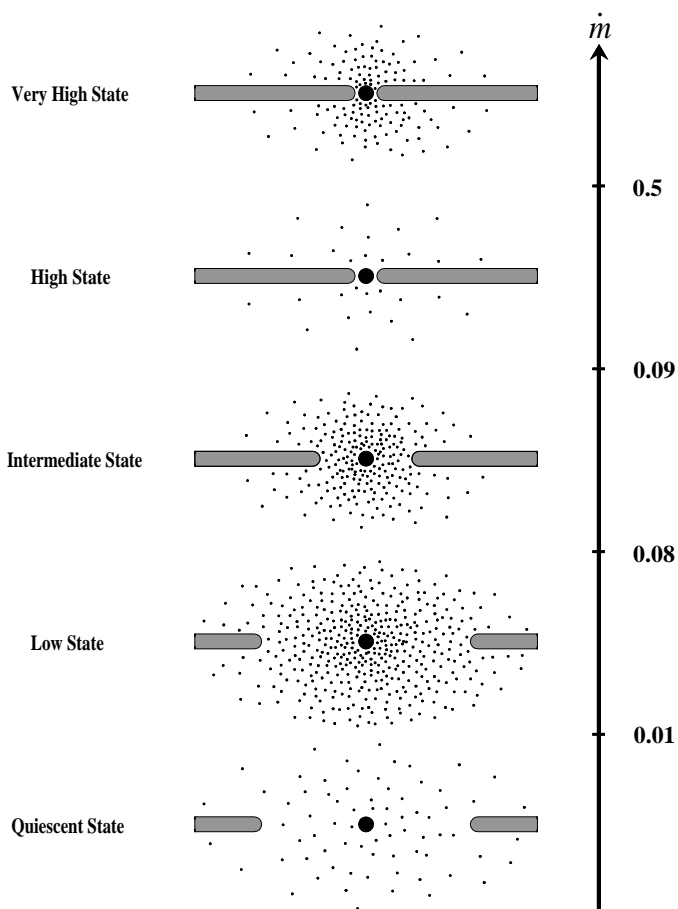


Figure 2.6: Graphic interpretation of the relative strength of the accretion disk and the Comptonizing plasma according to the ADAF model (section 2.2.4). The transition radius  $r_{tr}$  between both components – and thus the state – are determined by the mass accretion rate  $\dot{M}$  (Esin, McClintock & Narayan, 1997, Fig. 1).

#### 2.1.4 The Quiescent State

In the quiescent or off state of black hole transients only very weak X-ray emission can be detected (corresponding to a luminosity of the order of  $10^{30} - 10^{34}$  erg/s compared to typically  $10^{36} - 10^{38}$  erg/s in the hard state). This state can be especially

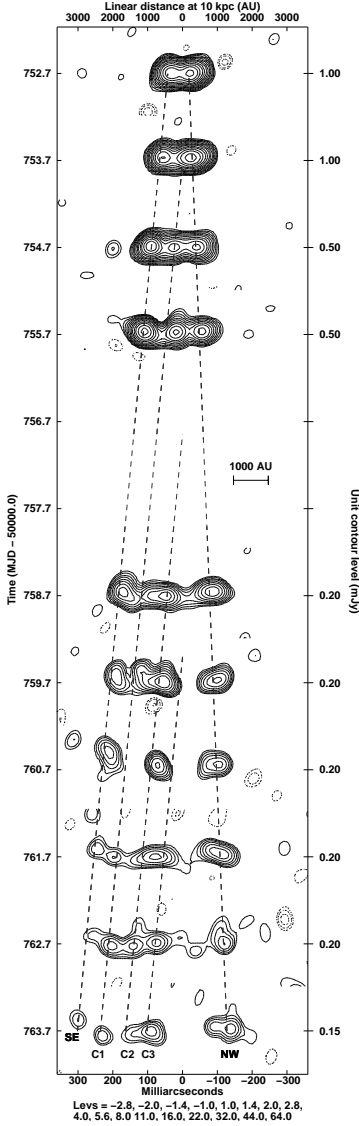


Figure 2.7: *MERLIN* observations at 5 GHz of GRS 1915+105 showing discrete ejections of material radiating at radio wavelengths and their apparent superluminal motion (Fender et al., 1999, Fig. 2).

well explained by the ADAF model (see, e.g., Menou et al., 1999; Narayan, Garcia & McClintock, 2001, and section 2.2.4). In its context the quiescent state corresponds to an accretion rate below 1%  $L_{\text{Edd}}$  (bottom plot of Fig. 2.6). The extension of the hot

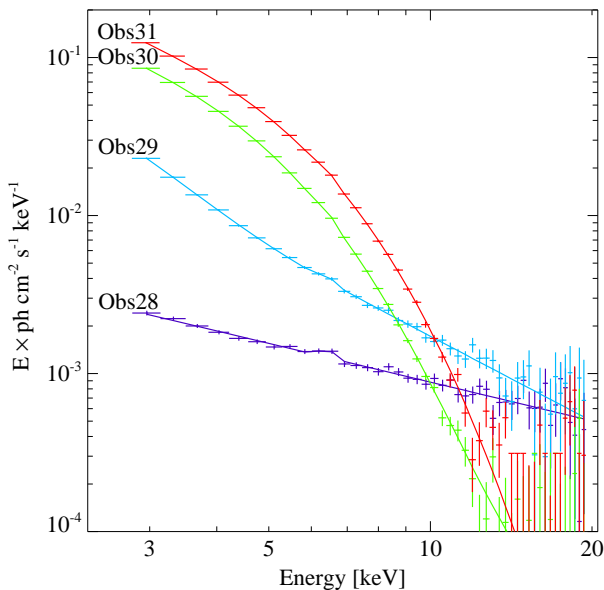


Figure 2.8: Spectral evolution (*RXTE/PCA* 2–20 keV) of LMC X-3 from a clear hard state in 1999 May (best fit:  $\Gamma = 1.8$  power law, Fe line fixed at 6.4 keV, no soft excess) to a clear soft state in 1999 August (best fit:  $kT = 1.16$  keV black body,  $\Gamma = 5.5$  power law, Fe line frozen at 6.4 keV) – the only known state for this source until this monitoring campaign (Wilms et al., 2001, Fig. 4).

plasma is large, but due to the low accretion rate its luminosity is lower than in the hard state. The special feature of ADAF models, the fact that much of the energy of the hot plasma – the advection dominated accretion flow – is stored in the protons and not in the electrons, is of special interest in the quiescent state: since the protons are advected into the black hole without releasing their thermal energy, these flows are underluminous, specifically as compared to the quiescent state of transient neutron star X-ray binaries, where all the residual energy of the accretion flow is transformed into radiation on the neutron star surface. Consistent with these ideas, a systematic difference in X-ray luminosity between black hole and neutron star X-ray binaries in quiescence has been observed for a small sample of sources (Garcia et al., 2001; Narayan, Garcia & McClintock, 2001; Kong et al., 2002).

### 2.1.5 Transitions: LMC X-3, a Prominent Example

As already mentioned, all the transient BHXRBs go through different states during their outbursts. Of the five persistent BHXRBs, 1E 1740.7–2942 and GRS 1758–258 have so far always been found in the hard state<sup>2</sup>, while LMC X-1 has always been found in the soft state. Cyg X-1 is predominantly found in the hard state but has been known to transit to soft states of a few months duration on a timescale of years. This characterization of Cyg X-1 has to be updated by the observation of a softer than normal hard state and the associated occurrence of very brief (near) soft states every few months during our *RXTE* monitoring campaign (chapter 5). The knowledge about the state behavior of LMC X-3 has also recently been expanded by an *RXTE* monitoring campaign performed by our group (Nowak et al., 2001; Wilms et al., 2001): LMC X-3 was believed to be a pure soft state source, although it was known from *Ariel V*, *HEAO1*, *Ginga*, and *HST* data that the soft X-ray count rate of this source varies by a factor of up to 5 on a quasi-regular basis of  $\sim 100$  days (Griffiths & Seward, 1977; Cowley et al., 1991, 1994). With one  $\sim 10$  ks pointed *RXTE* observation every three weeks in 1997 and 1998, we were able to derive the spectral evolution of the source over the luminosity variations. From Fig. 2.8 it is clear that these variations are actually associated with transitions to the hard state during the flux minima, thus making LMC X-3 the one permanent X-ray emitting black hole binary showing state transitions most often and most regularly. As a possible reason for this behavior, Wilms et al. (2001) suggest a “Compton heated accretion disk wind driven limit cycle” after Shields et al. (1986): In LMC X-3 – which is most probably not a pure wind accretor – the circularization radius is large enough to allow the development of an accretion disk wind via Compton heating of the outer disk from the central X-ray source, which regulates the mass accretion rate onto the black hole, thus triggering the observed state transitions. This is consistent with LMC X-1 – a wind accretor with a smaller circularization radius – not showing any transitions to the soft state (see the *RXTE* monitoring of LMC X-1, which is also reported by Nowak et al. 2001).

### 2.1.6 Transitions: New Results from this Work

To complete the description of state behavior, I mention some new results from the Cyg X-1 *RXTE* monitoring campaign here, in advance to the results chapters 4 and 5. One of the main results of the Cyg X-1 monitoring is that the short term variability apparently can deliver the strongest indicators of “state transitions in progress” known so far: While it has been known since the soft state of 1996 that the power spectra of Cyg X-1 during the transition to or from the soft state (=intermediate state) may look very different from either soft or hard state PSDs (Belloni et al., 1996),

<sup>2</sup>Note, however, that since 2001 March GRS 1758–258 displays a peculiar off/soft state (Smith et al., 2001).

the monitoring confirmed this on numerous occasions (chapter 5). In addition, our modeling of the power spectra allows to quantify *how* the transitional PSDs are different (chapter 5). Other Fourier statistics describing the short term variability are also very clear indicators of transitional states (chapters 4 and 5): the time lags between two X-ray lightcurves of different energy bands are larger during transitions, while the coherence between those two energy bands is lower during transitions (the time lags and the coherence function are introduced in sections 3.5 and 3.4). However, these quantities are *not* significantly different in the hard and soft state, themselves. While the change of lags and coherence during transitions had also been noted before for the 1996 episode (Cui et al., 1997), again the monitoring provides many recurrences, as well as their comparison to both hard and soft state quantities. Similar PSD/lag/coherence behavior has also been observed during the intermediate state of the 2001 outburst of the black hole transient XTE J1650–500 (Kalemci et al., 2002).

## 2.2 Accretion Models

While the phenomenology and the basic accretion model components described in the previous section are at this point well established, there exists, however, no physical model which links all the components in a self-consistent way and explains the observed canonical properties<sup>3</sup>. However, as can be expected for such a complex problem, many accretion models exist that are concentrating on certain aspects of the accretion process. Overviews have, e.g., been presented by Poutanen (1998), Svensson (1998), Bisnovatyi-Kogan (1999), Zdziarski (2000), Beloborodov (2000), Spruit (2001), and Done & Nayakshin (2001a). In this section I will give a brief summary of historical accretion models as well as of those models that are presently discussed. This summary is intended to introduce special features of the models (e.g., the sphere+disk geometry), to point to recent trends (e.g., the recent realization of the importance of outflows), and to provide a basis to interpret the results presented in chapters 4 and 5. It is *not* a *description* of the individual models – for that information I refer to the most relevant publications in each model section. Following the historical evolution of physical accretion models, section 2.2 concentrates on modeling spectral aspects. The temporal variability of the emitted X-rays cannot yet be consistently incorporated into the physical accretion models. Examples for sub-models, especially concentrating on explaining the hard state short term variability, are described in section 2.3 and are evaluated in the context of interpreting results from the Cyg X-1 monitoring campaign in chapters 4, 5, and 6.

---

<sup>3</sup>Not to mention source behavior that deviates from the canonical properties, as, e.g., in case of the microquasars.

### 2.2.1 The Standard $\alpha$ Accretion Disk

The modern standard theory of disk accretion was formulated in the papers of Shakura (1972) and Shakura & Sunyaev (1973). The model considers a thin gaseous disk that rotates around the black hole with Keplerian angular velocity. Its height is regulated by the pressure in the disk,  $p$ , which supports the disk against the vertical component of gravity. The matter in the disk gradually drifts inward due to viscous stress. Shakura (1972) suggested that matter in the disk is turbulent and parameterized the turbulent viscous stress tensor by the disk pressure:  $t_{r\phi} = \alpha p$ ,  $\alpha < 1$ . In its stable state, for not too high temperatures, this  $\alpha$  disk is geometrically thin, optically thick and radiates as a multi-color black body (Mitsuda et al., 1984, see also Merloni, Fabian & Ross 2000). The spectrum is a sum of black bodies with a radial temperature distribution  $T(r) \sim r^{-3/4}$  (Fig. 1.2). This radiation corresponds to the UV and soft X-ray emission of AGN as well as of BHXRBs. For explaining the hard X-ray component of these sources, however, additional models are needed.

#### 2.2.1.1 Relativistic Disks

In the vicinity of the black hole general relativistic (GR) effects become important. Improved disk models which are taking this – as well as the spin of the black hole – into account have been successful in reproducing the soft state spectra of galactic black holes: Gierliński, Maciolek-Niedzwiecki & Ebisawa (2001) model the BHXRBs LMC X-1 and GRO J1655–40 using a GR disk plus a thermal Comptonization model (LMC X-1) or a power law (GRO J1655–40). They concentrate on determining the spin parameter,  $a$ , finding that for LMC X-1 a broad range of  $a = 0 \dots 0.75$  is consistent with the data while for GRO J1655–40 the spin can be constrained to  $0.68 < a < 0.88$ .

#### 2.2.1.2 Vertical Disk Structure

In analytical as well as in numerical work it has been customary to discuss essentially one-dimensional solutions, i.e., to obtain the radial structure of the disk by considering equations averaged over the thickness of the disk. This is also true for quasi-spherical flows (ADAFs, section 2.2.4). It has been shown, however, that the flow cannot be properly described by height averaged values (Kley & Li, 1993; Abramowicz, Björnsson & Igumenshchev, 2000). Many new projects now concentrate on including the vertical structure of the disk, i.e., on 2-d or 3-d descriptions (see, e.g., Igumenshchev, Abramowicz & Narayan, 2000; Hawley, Balbus & Stone, 2001; Agol et al., 2001; Caunt & Tagger, 2001, and Fig. 2.9 on the next page). A tendency for back-flows in the midplane of the disk at a certain distance of the black hole has been noted (Kley & Li, 1993).

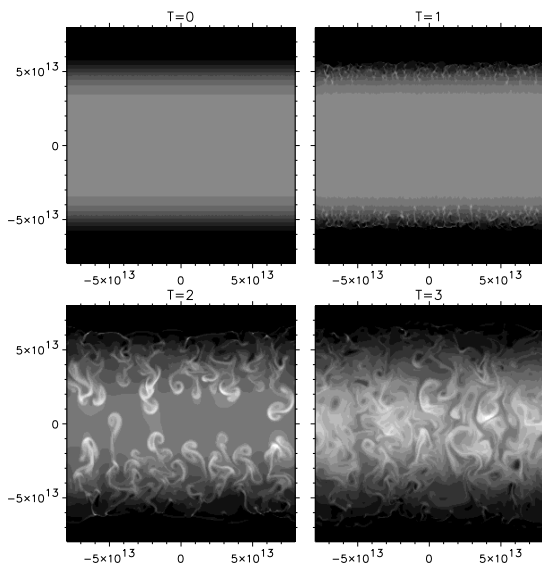


Figure 2.9: Density distribution evolving during a hydrodynamic simulation of a standard accretion disk with convection. Convection can alter the vertical structure of the disk considerably, e.g., producing thinner disks than the standard  $\alpha$  disk. The x- and y-axis are denoting the radial and vertical length scale of the disk and are labeled in cm (Agol et al., 2001, Fig. 1).

### 2.2.1.3 Disk Instabilities

Matter has to lose angular momentum to fall deeper into the gravitational potential well of the black hole. Various models for angular momentum transport have been proposed (Li et al., 2001), including those having a purely radial transport in the disk and those using magneto-hydrodynamical outflows (MHD jets). One promising mechanism works via MHD turbulence within the disk (Balbus & Hawley, 1991; Hawley & Balbus, 1991, and Fig. 2.10). The responsible magneto-rotational instability (MRI) has been explored in numerical simulations (Miller & Stone, 2000; Hawley & Krolik, 2001; Hawley, 2001, and therein). It is one of the best candidates for heating a hot coronal plasma and for introducing the short term variability of the hard X-ray emission via magnetic reconnection events (shots or flares, see section 2.2.3 and section 2.3). In cases where no strong coupling between a magnetic field and the disk is given, a purely hydrodynamic means of angular momentum transport is required as the “Rossby wave instability” proposed by Li et al. (2001).

A different kind of disk instability which leads to discrete ejections of material from the disk is discussed by Caunt & Tagger (2001) and in the references given by



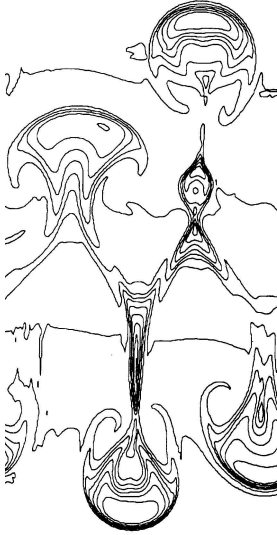


Figure 2.10: Angular momentum contour lines that develop during a simulation of the magneto-rotational instability, demonstrating the angular momentum transfer out off the disk in bubbles due to this instability (Hawley & Balbus, 1991, Fig. 5c).

these authors (“accretion-ejection instability”, AEI).

It has also been found that the whole accretion disk can oscillate on rather complex Eigenmode-frequencies. This form of instability is a good candidate for explaining quasi-periodic oscillations of the X-ray flux, especially the well known 67 Hz QPO of GRS 1915+105 could be explained by such a disk mode (Nowak et al., 1997). For a review on diskoseismology, see Nowak & Lehr (1998).

### 2.2.2 The Two-Temperature Disk (SLE, unstable)

To explain the hard spectrum of BHXRBS, Shapiro, Lightman & Eardley (1976, SLE) suggested a two-temperature model of an accretion disk where the protons are much hotter than electrons,  $T_p \gg T_e$ . The pressure associated with the hot proton component keeps the disk geometrically thick and optically thin (geometry as in Fig. 2.11, top). While SLEs are in agreement with observed hard X-ray spectra of BHXRBS and AGN, their shortcoming is that they are thermally unstable against small perturbations of the proton temperature (Pringle, 1976; Piran, 1978). Thus they are not considered likely candidates for being realized in these objects. However, SLEs provide the basis for the development of the currently often applied ADAF models (section 2.2.4).

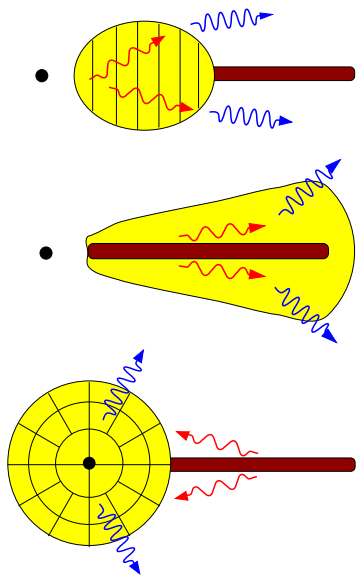


Figure 2.11: Different geometries that are discussed for the thin disk and hot plasma accretion components of BHXRBs and AGN. **Top:** “ADAF”. **Middle:** “Sandwich” or “slab”. **Bottom:** “Sphere+disk” (M.A. Nowak, J. Wilms, priv. comm.).

### 2.2.3 Accretion Disk Coronae (ADC)

The idea of the existence of a hot, low density plasma in addition to the accretion disk is rather old (Bisnovatyi-Kogan & Blinnikov, 1977; Liang & Price, 1977). The picture used to be that of an accretion disk covered by the corona on both sides (Fig. 2.11, middle) – however, as I will describe below, this “sandwich” geometry poses great problems for BHXRBs. The physical parameters defining the Compton corona are its optical depth  $\tau_c$  and its average electron temperature  $kT_e$ . There are two main classes of ADC models: in the first class the corona accretes fast above the disk (Janiuk, Życki & Czerny, 2000), in the second and more widely used class the corona is coupled to the disk by a magnetic field. In these models the corona is heated by reconnecting magnetic loops emerging from the disk as first proposed by Galeev, Rosner & Vaiana (1979, and Fig. 2.12). While the mechanism described by these authors – amplification of a seed magnetic field by differential rotation and turbulent convection – is not sufficient to explain the hard state of BHXRBs, the magneto-rotational instability (MRI) described by Balbus & Hawley (1991), can produce magnetic energy of the order of the total dissipated energy. Via buoyant transport the generated magnetic loops reach the corona where the gas pressure is lower than the magnetic pressure and the energy is released in magnetic reconnection events. The hard state of BHXRBs may be explained as being due to such a “corona-dominated” dissipation

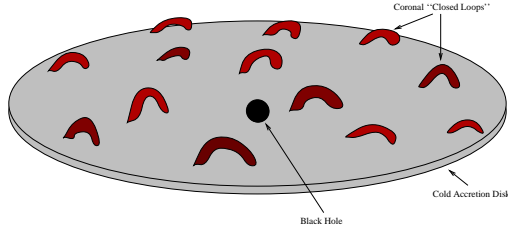


Figure 2.12: Illustration of magnetic loops above a thin accretion disk (Dove, 1997).

(Beloborodov, 2000). Since the density of the disk has to be below a certain limit in order for the MRI to work (Balbus & Hawley, 1991), there is a threshold  $\dot{M}$  for it generating reconnecting magnetic loops above the disk. For higher accretion rates the bulk of the energy is then released inside the optically thick disk and the coronal activity is suppressed, thus providing a scenario for the soft state.

### 2.2.3.1 Comptonization

In ADCs, the accretion disk is the source of seed photons which are being Comptonized by the corona and it is the medium responsible for the observed reprocessing and reflection features. Since Sunyaev & Trümper (1979) confirmed that the hard state spectrum of Cyg X-1 can be modeled with up-scattering of soft photons in a hot plasma by inverse Compton scattering, this radiation process has been assumed to be the dominant source for the hard X-ray emission from BHXRBS and AGN. It has been extensively explored analytically and numerically (e.g., by Sunyaev & Titarchuk, 1980; Coppi, 1992; Titarchuk, 1994; Hua & Titarchuk, 1995; Dove, Wilms & Begelman, 1997; Zdziarski, 1998; Malzac, Beloborodov & Poutanen, 2001; Psaltis, 2001) and numerous hard state spectra have been modeled using Comptonization models (e.g., Dove et al., 1997; Wilms et al., 1999). For a detailed description of the Comptonization physics and formulae, I refer to Wilms (1998, and references therein).

In the basic Compton scattering process, a photon of energy  $E$  collides with a stationary electron, transferring kinetic energy  $T$  to the electron and reducing its own energy to  $E'$  (Fig. 2.13), which is given by:

$$E' = \frac{E}{1 + \frac{E}{m_e c^2} (1 - \cos \theta)} \quad (2.1)$$

The differential cross section of this process and the angular distribution of the electron after the collision is given by the Klein-Nishina formula (substituting Eq. 2.1 and integrating over  $\theta$  yields the total cross section  $\sigma_{\text{es}}(E)$ , see, e.g., Rybicki & Lightman

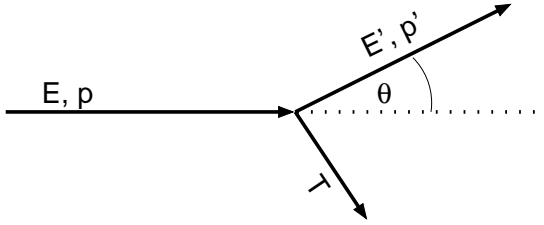


Figure 2.13: Illustration of Eq. (2.1) for Compton scattering of a photon from a stationary electron (Wilms, 1998, Fig. 2.2).

1979):

$$\frac{\sigma_{\text{es}}}{d\Omega} = \frac{3}{16\pi} \sigma_{\text{T}} \left( \frac{E'^2}{E} \right) \left( \frac{E}{E'} + \frac{E'}{E} - \sin^2 \theta \right) \quad (2.2)$$

where

$$\sigma_{\text{T}} = \frac{8\pi}{3} r_0^2 = \frac{8\pi}{3} \left( \frac{e^2}{m_e c^2} \right)^2 = 6.652 \times 10^{-25} \text{ cm}^2 \quad (2.3)$$

For low energies  $E$  the Klein-Nishina formula is approximated by the classical Thomson formula:

$$\frac{\sigma_{\text{T}}}{d\Omega} = \frac{3}{8\pi} \sigma_{\text{T}} \left( \frac{1 + \cos^2 \theta}{2} \right) \quad (2.4)$$

For higher  $E$ , Eq. (2.2) is highly dependent on  $\theta$ : the scattering is concentrated in forward direction due to relativistic beaming. In a plasma, Compton scattering from protons is suppressed by a factor of  $(m_e/m_p)^2 \sim 10^{-7}$ , as compared to Compton scattering from electrons.

In astrophysical sources, the electrons are not stationary but “hot” ( $\sim 100$  keV). Usually they are assumed to have a relativistic Maxwellian velocity distribution with a characteristic temperature,  $T_e$ :

$$N(\gamma) \sim \gamma^2 \beta \exp[-\gamma m_e c^2 / kT_e] \quad (2.5)$$

where  $\beta = v_e/c$  is the electron velocity and  $\gamma = (1 - \beta^2)^{-1/2}$  the associated Lorentz factor. In this case the incident soft photons which have energies much lower than the electrons ( $\sim 100$  eV), i.e.,  $E \ll T_e$ , are on average gaining energy from the Compton collisions. Due to the Maxwellian electron distribution this process is called *thermal* Comptonization (see, however, *non-thermal* Comptonization, page 56). The equations given above have then to be modified in order to take the electron energy into

account: While in case of stationary electrons the average energy change of the scattered photons is given by:

$$\frac{\Delta E}{E} = -\frac{E}{m_e c^2} \quad (2.6)$$

(obtained by averaging Eq. 2.1 over all  $\Omega$ ), electrons with  $kT_e < m_e c^2$  cause an average photon energy change of:

$$\frac{\Delta E}{E} = \frac{4kT_e - E}{m_e c^2} \quad (2.7)$$

confirming that the photons are on average gaining energy, as long as  $E < 4kT_e$  ( $A = 4kT_e/m_e c^2$  is called the Compton amplification factor). If the photons are moving through a plasma cloud of optical depth  $\tau_c$ , their average energy change has to be multiplied by their average number of scatterings and is given by the Compton “y-parameter”:

$$y = \frac{4kT_e}{m_e c^2} \max(\tau_c, \tau_c^2) \quad (2.8)$$

The emerging spectrum of the Comptonized photons can be derived by describing the process as a diffusion problem. In the limit of large optical depths ( $\tau_c > 1$ ) and for  $kT_e \ll m_e c^2$ , this description is provided by the Kompaneets equation for the photon occupation number  $n(E)$  (see Rybicki & Lightman, 1979). A derivation of the Comptonized photon spectrum from the Kompaneets equation can be found in Sunyaev & Titarchuk (1980). Extensions of this formalism to lower optical depths and relativistic temperatures have been presented by Titarchuk (1994) and Hua & Titarchuk (1995). Fig. 2.14 gives an example for a photon spectrum emerging from a hot Comptonizing plasma. The decomposition of the total spectrum into spectra consisting of photons that underwent 1, 2, 3, 4, and 5 Compton collisions before leaving the plasma is also shown, illustrating how the observed power law spectrum is built up by several scattering orders. If the coronal parameters are such that many photons reach energies comparable to the plasma temperature, i.e., if the Compton-y is large, photons pile up at those energies. This is the case of “saturated Comptonization”, where a broad hump develops in the spectrum at  $\sim 3kT_e$ , which – due to photon number conservation – has the form of a Wien spectrum. The total spectrum displayed in Fig. 2.14, e.g., shows such a “Wien hump”. For smaller values of the Compton-y, i.e., “unsaturated Comptonization”, the power law simply turns over in an exponential cutoff. This shape – an exponentially cut-off power law – corresponds to the observed hard state spectra.

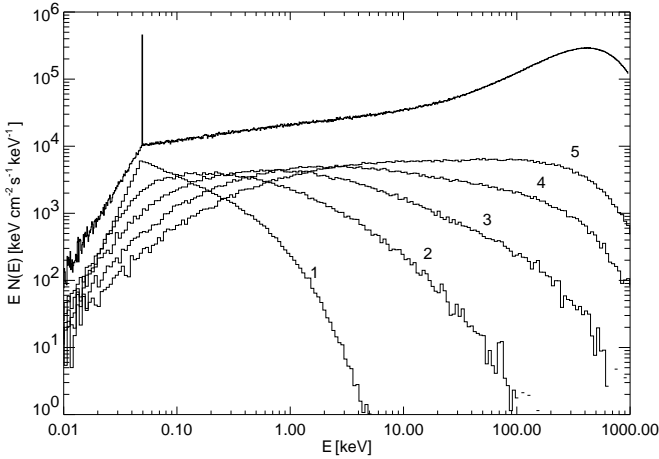


Figure 2.14: Monte Carlo simulation of spectra produced by thermal Comptonization of seed photons with an energy of  $kT_{\text{seed}} = 50 \text{ eV}$  injected at the center of a spherical plasma with a temperature of  $kT_e \sim 200 \text{ keV}$  and an optical depth of  $\tau_c = 5$ . The total emerging spectrum (top) as well as the scattering orders 1–5 are shown (Wilms, 1998, Fig. 2.4).

### 2.2.3.2 Sphere+Disk Geometry

Self-consistent ADC models on the basis of a non-linear Monte Carlo code have first been presented in a series of papers by Stern et al. (1995a), Stern et al. (1995b), and Dove, Wilms & Begelman (1997). Dove et al. (1997) apply them to the broad band hard state spectrum of Cyg X-1 and other BHXRBs. These authors found that a sandwich geometry does not allow a self-consistent description of the observed spectrum due to the following reason:

The cold accretion disk partly re-emits incident hard X-rays from the corona in a reprocessed form (see page 57 and Fig. 2.17 for more details). Like the seed photons, this radiation Compton-cools the corona, providing a coupling between the radiation field and the coronal plasma (Haardt & Maraschi, 1991, 1993; Haardt et al., 1993; Dove, Wilms & Begelman, 1997). If this coupling is taken into account, the balance between viscous heating and Compton-cooling results in a maximum possible coronal temperature  $kT_{e,\text{max}}$  for a given optical depth  $\tau_c$  and source geometry. The cooling and therefore  $kT_{e,\text{max}}$  obviously depend on the covering factor  $R = \Omega/2\pi$ , where  $\Omega$  is the angle under which the disk is seen from the corona. Since  $R = 1$  in the sandwich geometry, the cooling factor is big and the maximum possible temperature of the optically thin corona can only be as high as  $\sim 140 \text{ keV}$  (Dove, Wilms &

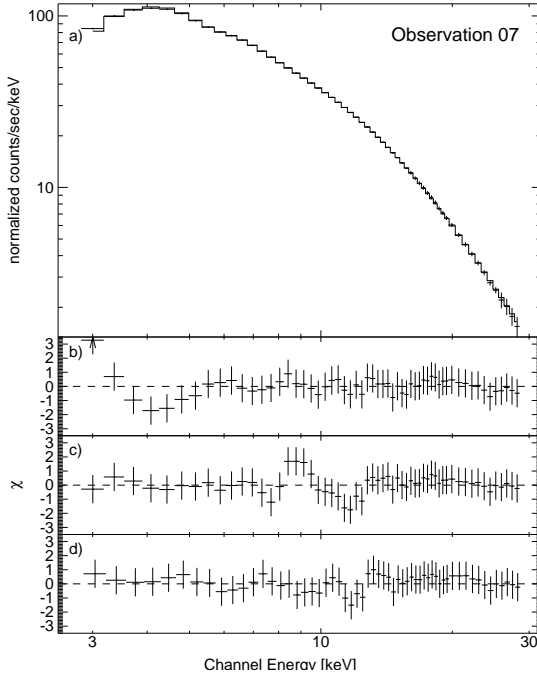


Figure 2.15: Comparison of several different spectral models for an *RXTE/PCA* observation of GX 339–4 (Wilms et al., 1999, Fig. 3b). Energy-dependent systematic errors have been taken into account. **a** Data and broken power law plus Gaussian line. **b** Contribution to  $\chi$  from the broken power law plus Gaussian line model,  $\chi_{\text{red}}^2 = 0.53$ . **c** Contribution to  $\chi$  from an ionized reflection model (`pexrav`) plus Gaussian line,  $\chi_{\text{red}}^2 = 0.48$ . **d** Contribution  $\chi$  from the sphere+disk model plus Gaussian line,  $\chi_{\text{red}}^2 = 0.30$  and  $kT_e = 28.4 \pm 0.4$  keV,  $\tau_c = 3.3 \pm 0.1$ .

Begelman, 1997), lower than the values previously obtained from hard state spectra ( $kT_e \sim 150$  keV,  $\tau_c \sim 0.3$ ). In addition a strong soft excess and strong reprocessing features are provided by the sandwich geometry, which are not observed in reality.

All these problems are solved if the ADC is “photon starved” resulting in less reprocessing, less cooling, and higher possible coronal temperatures. This is, e.g., the case for smaller covering factors  $R \sim 0.3$ , e.g., for the sphere+disk geometry where the outer thin cool disk is physically separated from the inner spherical hot plasma (Fig. 2.11, bottom). In the case of Cyg X-1 self-consistent sphere+disk fits deliver  $\tau_c \sim 1.5$  and  $kT_e \sim 90$  keV, a higher temperature than possible in the sandwich geometry for this value of  $\tau_c$  (Dove et al., 1997). Another example, this time for GX 339–4, is displayed in Fig. 2.15. Sphere+disk like geometries are now the most considered accretion geometries (see, e.g., Poutanen, Krolik & Ryde, 1997), especially since the popular ADAF models look very similar (Fig. 2.11, top, and section 2.2.4). Ionization of the reprocessing disk material might however change this picture (page 57).

### 2.2.3.3 Magnetic Flares

The main energy dissipation in the corona can be assumed to occur in localized blobs, initially producing compact X-ray flares above the corona. There is no detailed model for this magnetic flare phenomenon yet, although it has been studied for many years in the context of solar activity. However, the blob geometry (= “patchy” corona) is an alternative to the sphere+disk geometry since it can also provide the small disk covering factor  $R$  that is necessary to explain the weak reprocessing features observed in the hard state spectra of BHXRBs: Beloborodov (1999) and Malzac, Beloborodov & Poutanen (2001) recently showed that (only) if a mildly relativistic bulk velocity ( $\beta = v/c \leq 0.5$ ) away from the disk is assumed for the flare material, the observed hard state spectra can in principle be reproduced (since the flare emission is hardening with time, the  $R - \Gamma$  correlation mentioned in section 2.1.1 can be reproduced with this model). For the timing properties of flare models see section 2.3.

### 2.2.3.4 Bulk Motion Comptonization

A sphere+disk scenario where additional Comptonization physics has to be considered is the following: The thin accretion disk has at least to be disrupted at the boundary of three Schwarzschild-radii (for a non-rotating black hole) since no stable orbits exist closer to the black hole. The matter is then forced to proceed towards to black hole in almost free fall manner – the radiative forces being negligible with respect to the gravitational forces (Laurent & Titarchuk, 1999). Such converging inflows (CIs) or bulk motion Comptonization models (BMCs) are related to the ADAF models (section 2.2.4) but are listed *here* as a source of additional Comptonization physics. The effect of the bulk motion of the Comptonizing electrons on the emerging BHXRB spectra has been studied in a series of papers (Laurent & Titarchuk, 1999, 2001, and therein). It was found that BMC is in principle able to reproduce the extended power law spectra observed in the soft state up to  $\sim 500$  keV (Shrader & Titarchuk, 1998; Borozdin et al., 1999).

### 2.2.3.5 Non-thermal Comptonization

It has been argued that even bulk motion Comptonization might have difficulties to explain the unbroken soft state spectra up to  $\sim 10$  MeV (Coppi, 1999). A rather simple alternative is to allow for a hybrid Comptonizing plasma, where the electron energy distribution is approximately a relativistic Maxwellian *plus a power law tail*. Fig 2.16 shows Comptonization spectra for different compactness ratios  $l_{\text{th}}/l_{\text{nth}}$ , i.e., for different luminosity ratios ( $l \sim L/R$ , where  $R$  is the characteristic radius of the hot plasma region), of thermal to non-thermal electrons. The lower the contribution of thermal electrons, the higher is the influence of pair processes: a strong electron-positron annihilation line emerges and extended continuum emission is present. The peaking of



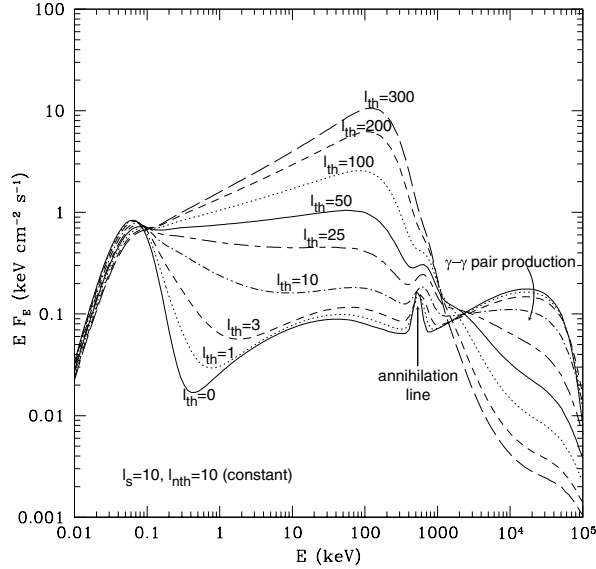


Figure 2.16: Simulated spectra emerging from a hybrid plasma with a fixed non-thermal electron compactness ( $l_{\text{nth}}=10$ ) and different values for the thermal electron compactness (Coppi, 1999, Fig. 1). The soft seed photons have a black body spectrum with a fixed compactness of  $l_s = 10$ .

the latter between 10 and 100 MeV is due to  $\gamma\text{-}\gamma$  pair production which is removing the hardest photons. A review about hybrid plasmas is presented by Coppi (1999). Such models are available as a plasma code (`eqpair`, Coppi, 1992) and have been used to model spectra of Cyg X-1 in all states (Gierliński et al., 1999; McConnell et al., 2002), especially in the soft state up to 10 MeV, as well as observations from the microquasar GRS 1915+105 (Zdziarski et al., 2001) and from GX 339-4 (Nowak, Wilms & Dove, 2002).

### 2.2.3.6 Ionization Layers

As has already been noted, the radiation reprocessed by the cool accretion disk has been used to constrain the accretion geometry (page 54). The most notable features of this emission are a Compton reflected continuum with its maximum at  $\sim 30$  keV and an iron  $K\alpha$  fluorescence line (Fig. 2.17). It was found that BHXRBS do not show the broadened iron lines which are seen in some AGN (Wilms et al., 2001) and which indicate a strong reflector very near to the black hole (e.g., Gierliński et al., 1997; Done & Życki, 1999). The strength of the reprocessed emission in BHXRBS is con-

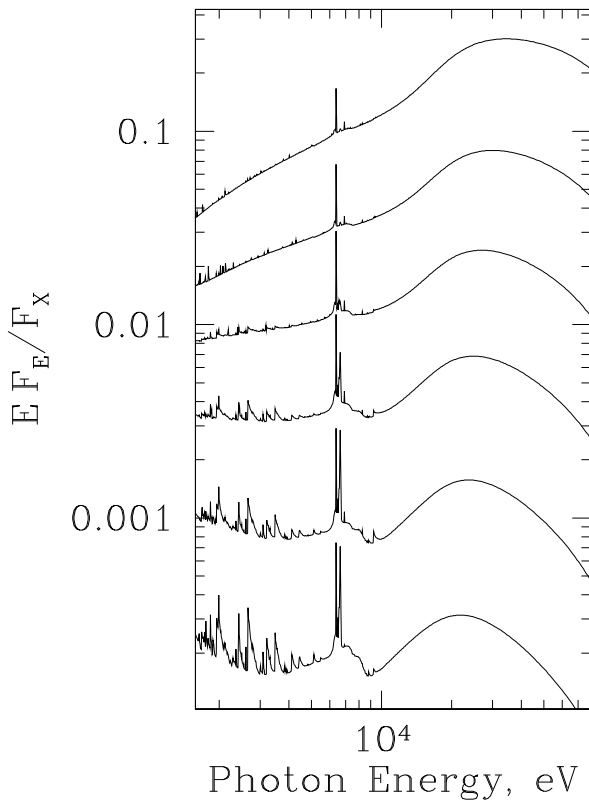


Figure 2.17: Spectra obtained from simulations of the reprocessing of an incident power law continuum (not shown) as a function of the photon index ( $\Gamma = 1.5, 1.7, \dots, 2.5$ ). Depending on the hardness of the incident spectrum, ionization layers with different temperature distributions and optical depths develop. For softer power laws stronger reflection signatures emerge (Done & Nayakshin, 2001a, Fig. 1, left panel).

sistent with a photon starved geometry (Dove et al., 1997). It has to be taken into account though that the reflection signature from the disk can be masked by complex ionization effects (Ross, Fabian & Young, 1999): For completely ionized gas, e.g., the reprocessed spectrum is only due to electron scattering and no characteristic iron feature is observed. Models including ionization are usually consistent with the observed  $R - \Gamma$  correlation described in section 2.1.1 (Young et al., 2001; Done & Nayakshin, 2001a).

While models assuming that the ionization is only radially dependent cannot reproduce the observed spectra (vertical “one zone model” Done & Nayakshin, 2001a, and therein, see, however, Young et al. 2001), it was recently found that there is a thermal ionization instability which can produce a highly ionized skin everywhere on top of the mainly neutral disk with a discontinuous but self-consistent vertical transition of the ionization state (Nayakshin & Dove, 2001; Done & Nayakshin, 2001a, and

therein). This hot skin can in principle reduce the observable reprocessing features from the disk, resulting in a small observed reflection fraction  $R$  that is not consistent with the actual geometry. The transition layer models are currently explored in terms of possible observational signatures that might nevertheless help to distinguish between geometries (Ballantyne, Ross & Fabian, 2001; Done & Nayakshin, 2001a,b).

#### 2.2.4 Advection Dominated Accretion Flows (ADAF)

In the SLE model, only a fraction of the dissipated energy remains in the hot proton component, the bulk of the energy is passed on to the electrons and radiated. Ichimaru (1977) considered a disk of such low density that the protons – which are again assumed to be preferentially heated by the accretion process (see, e.g., Quataert, 1998) – are unable to pass their energy to the electrons on the time scale of accretion. The protons advect the energy into the black hole or transport it outward in form of an outflow (Blandford & Begelman, 1999). These models have only recently been rediscovered (Narayan & Yi, 1995) and since then received much attention (for a review see Narayan, Mahadevan & Quataert, 1998). As the electron-proton collision rate increases with the density of the flow, a maximum accretion rate for which ADAFs are possible can be derived (Beloborodov, 2000):  $(\dot{M}/\dot{M}_{\text{Edd}})_{\text{max}} \sim 10\alpha^2$ , where  $\alpha < 0.1$ . As in SLEs, there is some radius  $r_{\text{tr}}$  where the standard cold accretion disk undergoes a transition to a hot two-temperature flow which emits hard X-rays by Comptonizing soft radiation in the unsaturated regime (and by Bremsstrahlung and synchrotron radiation). The geometry is thus comparable to the sphere+disk ADC (thus the same consistency arguments concerning X-ray reflection can be applied, see section 2.2.3). The  $\dot{M}$  dependence of the ADAFs, especially of  $r_{\text{tr}}$ , is their means to explain the existence of different BHXR states (Fig. 2.6). Being under-luminous, the ADAFs are applied mainly to low luminosity objects, such as Sgr A\* (Narayan et al., 1998) or X-ray nova in quiescence (see section 2.1.4 and Menou et al., 1999). However, the hard state spectra of BHXR states can also be modeled (Esin et al., 1998; Esin et al., 2001). A drawback of these models is that they do not consider any time dependence.

Many additions to the original ADAF model and discussions about whether ADAFs can really exist in nature (e.g., Dullemond & Turolla, 1998; Gu & Lu, 2000; Molteni, Gerardi & Valenza, 2001) have led to the development of a wealth of sub-classes, e.g:

**Relativistic Kerr Geometry ADAFs** (e.g., Peitz & Appl, 1997; Abramowicz, Lanza & Percival, 1997),

**ADIOS – advective (later: adiabatic) dominated inflow outflow solutions:** contain the necessity of outflows (Blandford & Begelman, 1999, see, however, Ogilvie 1999; Abramowicz, Björnsson & Igumenshchev 2000),

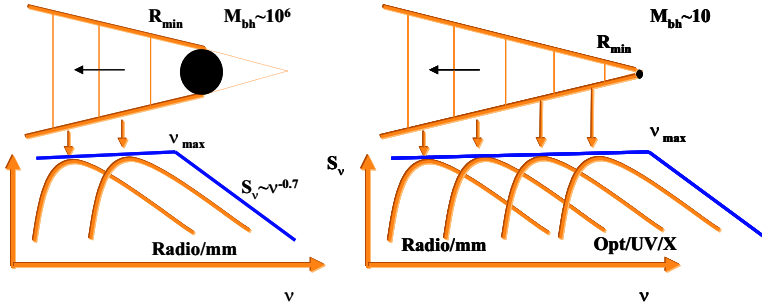


Figure 2.18: Illustration of the decomposition of a flat, optically thick radio spectrum into synchrotron emission components from different regions in a self-absorbed jet. The smallest length scale of the self-similar conical jet produces a break in the spectrum towards higher energies which can therefore be expected to scale with black hole mass. Here the situation for a black hole binary (right) and for an AGN is shown (left) (Falcke et al., 2001, Fig. 1).

**CIAOS – consistent inflow outflow solutions:** refined version of the ADIOS (Turolla & Dullemond, 2000),

**CDAFs – convection dominated accretion flows:** take into account that convection is usually strong in low  $\alpha$  ADAFs (e.g., Igumenshchev & Abramowicz, 2000; Ball, Narayan & Quataert, 2001; Machida, Matsumoto & Mineshige, 2001),

**PADAFs and WADAFs – preheated and wind ADAFs:** consider effects of heating and cooling (Park & Ostriker, 2001),

**Evaporating Coronae:** a promising model for the transition from thin disk to ADAF which is assumed to take place through a gradual (as a function of radius) evaporation (Liu et al., 1999; Meyer-Hofmeister & Meyer, 2001; Róźańska & Czerny, 2000), the evaporation initially produces a corona with a wind above the disk, which transforms into an ADAF further in.

### 2.2.5 Jet Dominated Emission

Observations in the 1990s have shown that radio emission is a ubiquitous property of BHXRBs in their hard state (Fender, 2001, and section 2.1.3). Whether a jet can be resolved or not, the observed radio cores display a flat spectrum, i.e., the frequency-dependent energy flux density  $S_\nu$  is approximately constant. Flat radio spectra can be explained with synchrotron emission of hot, relativistic electrons ( $1 < \gamma < 10000$ , power law distribution) that are moving with relativistic bulk motion ( $1 < \Gamma < 100$ )

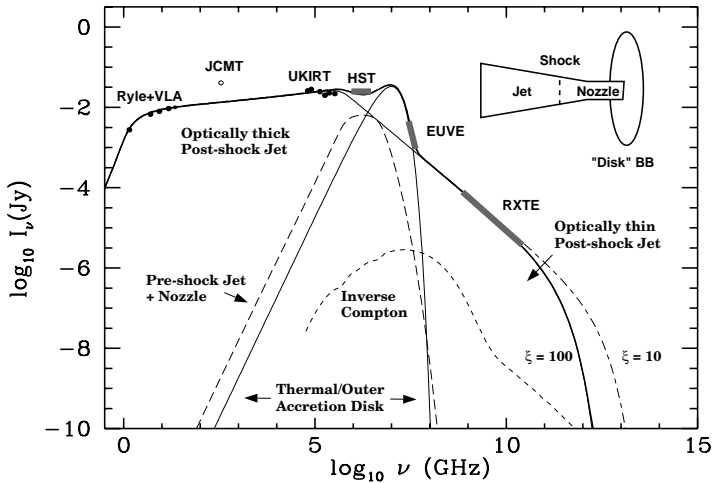


Figure 2.19: Broad band hard state spectrum of the BHXRB transient XTE J1118+480 from radio to X-ray energies. The overall shape can be well explained with synchrotron emission from different regions in a relativistic jet, a disk black body spectrum, and a comparatively small contribution due to inverse Compton scattering (Markoff, Falcke & Fender, 2001, Fig. 1).

in the standard jet model, where the overall radio spectrum is built up from emission from different regions in a self-absorbed jet (Blandford & Königl, 1979; Fender, 2001; Falcke et al., 2001, and therein). In this model the frequency  $\nu_{\text{max}}$  associated with the emission peak of each region is proportional to the distance of this region from the black hole. A question that is currently under investigation from the observational as well as from the theoretical point of view, is: how far does the synchrotron emission from the outflow extend to high energies? Fig. 2.18 illustrates that in the standard jet model a break is expected that is given by the smallest scale in the system. For BHXRBs synchrotron emission from the jet could thus contribute a considerable fraction of the observed X-ray emission (Falcke et al., 2001). It has been found that the broad band spectrum of the transient XTE J1118+480 in the hard state can indeed be described by a combination of a truncated disk, a small contribution from inverse Compton scattering, and a jet model contributing 90% of the observed power (Fig. 2.19 and Markoff, Falcke & Fender, 2001). However, whether this model generally holds for other BHXRBs in the hard state and in the same detail as achieved by Comptonization models (Fig. 2.15) remains to be seen.

### 2.3 The Importance of Timing Studies

In addition to the models discussed in the previous section, there is a class of models concentrating on explaining the hard state short term variability (Kazanas & Hua, 1999; Böttcher & Liang, 1999; Böttcher, 2001; Misra, 2000; Churazov, Gilfanov & Revnivtsev, 2001; Kotov, Churazov & Gilfanov, 2001; Poutanen, 2002, and therein), especially the observed hard state time lags (see Eq. 3.31, section 3.5). So far, these models are generally not consistently incorporated into the physical accretion models which have been described in the previous section. A phenomenological variability model that has often been used to describe the observed short term variability in terms of discrete X-ray flares “shot noise”) is described below. Further examples of this comparatively narrow and rather experimental model subset are evaluated in context of interpreting results from the Cyg X-1 monitoring campaign in chapters 4, 5, and 6.

Another class of accretion models that has received much attention in recent years is the one aiming to explain the quasi-periodic oscillations (QPOs) observed in the X-ray flux of many X-ray binaries (see, e.g., Miller, Lamb & Psaltis, 1998; Stella & Vietri, 1998; Nowak et al., 1999b; Psaltis & Norman, 2001; Caunt & Tagger, 2001). These models are mainly concentrating on understanding the strong narrow kHz oscillations that are predominantly displayed by neutron star binaries (although the microquasars most probably also show the same class of QPOs but at lower frequencies Strohmayr 2001a,b). A recent review has been given by van der Klis (2000). Since Cyg X-1 does not show these or any *strong, narrow* QPOs, I will not describe these models here, however, – as discussed in section 6.2 – our interpretation of the hard state power spectrum of Cyg X-1 in terms of broad noise components might be akin to these models.

The typical hard state short term variability shows a flat-topped PSD with an approximately  $\sim f^{-\alpha}$ ,  $\alpha = 1 - 2$ , slope towards high frequencies (section 2.1.1). Such  $f^{-\alpha}$  fluctuations are ubiquitous in nature (Press, 1978, and references therein). Magnetic flares are among the most promising mechanisms to explain such variability, an assumption that is strongly supported by the observation of  $f^{-\alpha}$  fluctuations in the solar soft X-ray emission (Ueno et al., 1997). Recent 3-d magneto-hydrodynamical simulations performed by Kawaguchi et al. (2000)<sup>4</sup> show that a magnetized accretion disk can indeed exhibit  $f^{-\alpha}$  fluctuations due to magnetic reconnection events (see also Hawley & Krolik, 2001).

Lightcurves displaying the typical hard state short term variability appear to the eye as a series of discrete short outbursts (shots). Accordingly, the so-called shot noise models have been used to describe this variability mathematically (Terrell,

<sup>4</sup>Note that these authors do not use an underlying standard  $\alpha$  accretion disk but one that is more akin to the ADAF disks described below.

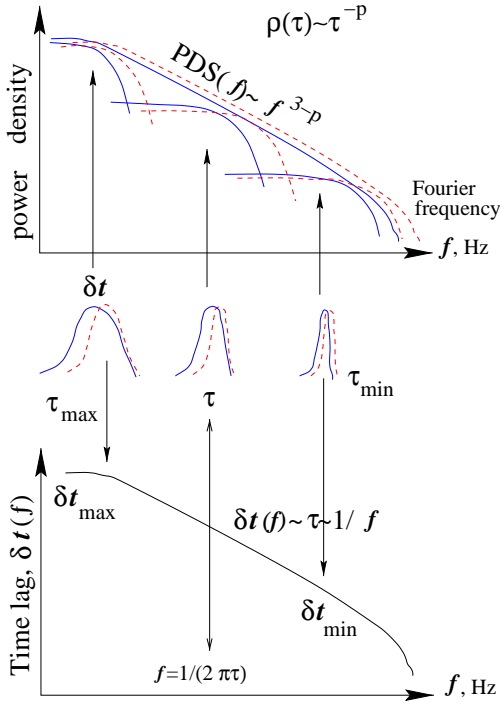


Figure 2.20: Power spectrum (top) and frequency dependent time lags (bottom) as derived from a modified shot noise model (Poutanen, 2002, Fig. 6b). Here the model of Poutanen & Fabian (1999) is illustrated, where flares are produced with a distribution  $\rho \sim \tau^{-p}$  of relaxation time scales  $\tau$ , and where the shots start soft (middle, solid) and become harder with time (middle, dashed), thus producing a positive time lag.

1972; Lochner, Swank & Szymkowiak, 1991). The original shot noise model for the BHXRB hard state consists of Poisson distributed count rate flares with zero rise time and an exponential decay with a fixed relaxation time scale  $\tau$  (Papoulis, 1991). Mostly these models have been evaluated by fitting shot noise power spectra to the observed power spectra of Cyg X-1. Since the PSD of the original shot noise model displays an asymptotic  $f^{-2}$  behavior, independent of  $\tau$ , complex combinations of relaxation time scales and shot profiles have been used over the years to reproduce the observed slope of  $\sim 1.5$  (“modified shot noise models”, see e.g., Weisskopf & Sutherland, 1978; Nolan et al., 1981; Meekings et al., 1984; Lochner, Swank & Szymkowiak, 1991). A summary of these attempts can be found in Pottschmidt (1997). In that work I was also able to show that a more generalized class of shot noise models, the linear state space models of first order (LSSM[AR1])<sup>5</sup>, can explain the overall PSD

<sup>5</sup>LSSM models are based on the stochastic autoregressive processes. They do not assume a fixed shot profile. Furthermore, LSSMs discriminate between observational noise and system inherent noise. They can also be evaluated in the time domain instead of in the frequency domain. (see König & Timmer, 1997; König, 1997, and therein, for a detailed description).

shape of Cyg X-1 – including a slope deviating from  $-2$  – with only one dynamical relaxation time scale of  $0.19 \pm 0.04$  s. Poutanen & Fabian (1999) introduce a magnetic flare model where the spectrally evolving flares are produced with a range of relaxation parameters in a pulse avalanche model in a self-organized critical state. The timing properties of this model are very similar to modified shot noise: a  $f^{-\alpha}$  PSD is obtained. How it is built up by a range of relaxation time scales is illustrated in Fig. 2.20. Interestingly, the time lags are proportional to the relaxation time scale, i.e.,  $\sim 1/f$  in this model (Fig. 2.20), which is also in rough agreement with the observation (Fig. 3.5).

With the high quality, high time-resolution data provided by *RXTE* since 1996, however, it has become more and more evident that a smooth, single process PSD with an approximate  $f^{-\alpha}$  shape is only a very rough description of the observed BHXRBS hard state variability: it has been suspected that the hard state PSD can usually be decomposed into multiple broad components (Smith et al., 1997; Berger & van der Klis, 1998; Nowak, 2000; Kalemci et al., 2001). A detailed multi-component decomposition of the hard and intermediated state PSD of Cyg X-1 is the main topic of this work. It is presented in chapter 5 and discussed in chapter 6.



## CHAPTER 3

---

### Fourier Statistics

In this chapter I summarize the mathematical formulation of the Fourier quantities which I use in chapters 4 and 5 to evaluate the short term variability in the lightcurves of Cyg X-1. The calculation of the Fourier frequency dependent power spectral density, the coherence function, and the time lags as well as their uncertainties and noise components is described. Due to the binned nature of measured lightcurve data used in this work, the discrete formulation is selected and the usual procedure to enhance the signal-to-noise-ratio of the measured quantities – averaging them over many lightcurve segments and Fourier frequencies – is also included. A review of Fourier analyses of astronomical time series concentrating on the PSD has been given by van der Klis (1989) and a series of time series analysis papers by J. D. Scargle includes the correction of the PSD for gaps in the lightcurve (Scargle, 1982, 1989). Most of the equations presented here, especially those associated with the coherence and the time lags, can be found in Vaughan & Nowak (1997) and Nowak et al. (1999a). For more details see also Bendat & Piersol (1986).

After the mathematical description in sections 3.1–3.5, examples of these Fourier quantities as measured during our monitoring campaign of Cyg X-1 (section 1.5) are presented in section 3.6. While the phenomenology of BHXRB power spectra has already been introduced in general in chapter 2, the purpose of section 3.6 is to describe the typical hard state timing properties, specifically as observed for Cyg X-1. *This section does not contain the new results from our monitoring campaign*, for those, I refer to chapters 4 and 5.

#### 3.1 *The Discrete Fourier Transform*

The variability of astronomical sources is usually expressed as a time series,  $x_h$ , of observed count rates in a certain energy band, where  $h$  denotes the number of the time bin during which the count rate was measured. In the following it is assumed that  $x_h$  consists of  $m$  evenly spaced time bins of length  $\Delta t$ . The basis of many powerful

statistics to evaluate  $x_h$  is its discrete Fourier transform  $X_j$ :

$$X_j = \sum_{h=0}^{n-1} x_h e^{2\pi i j h / m} \quad (3.1)$$

where  $i = \sqrt{-1}$ . Independent values for this complex quantity are obtained for the following frequencies, the Fourier frequencies:

$$f_j = \frac{j}{T} = \frac{j}{m\Delta t} \quad (3.2)$$

Here  $T = m\Delta t$  is the length of the lightcurve. Formally the Fourier frequencies are defined by  $j \in [-m/2, m/2]$  but for the analysis of measured lightcurves the minimally accessible frequency is given by the duration of the observation:  $j_{\min} = 1$ , i.e.,  $f_{\min} = 1/T$ . The maximally accessible frequency, the Nyquist frequency, is given by the bin time:  $j_{\max} = m/2$ , i.e.,  $f_{\max} = 1/(2\Delta t)$ . Also, measured lightcurves always contain noise, for X-ray lightcurves this is mainly counting, i.e., Poisson, noise (section 3.2.4). Since the lightcurve can be split into a signal component  $s_h$  and a noise component  $n_h$ , i.e.,  $x_h = s_h + n_h$ , this is also true for their discrete Fourier transforms:

$$X_j = S_j + N_j \quad (3.3)$$

In the following sections I describe the power spectral density (section 3.2), which is constructed from the Fourier transform of one lightcurve and the cross spectral density (section 3.3), which is derived from the Fourier transforms of two lightcurves, e.g., measured simultaneously in two different energy bands. The latter is the basis of the coherence function (section 3.4) and of the time lags (section 3.5).

## 3.2 The Power Spectral Density

### 3.2.1 Calculating and Averaging the PSD

The power spectral density (PSD) is a non-complex quantity obtained by multiplying the discrete Fourier transform and its complex conjugated quantity, i.e., the PSD is the squared magnitude of the complex Fourier transform.

$$P_j = X_j^* X_j = |X_j|^2 \quad (3.4)$$

The maximum frequency resolution of the PSD is again given by the Fourier frequencies. The power spectral density is directly related to the variance of the lightcurve (Parseval's theorem, see e.g., Schlittgen & Streitberg, 1995, page 80) in the sense that  $P_j$  gives the fraction of the total lightcurve variance that is due to variability

characterized by the frequency  $f_j$ . For practical use, several different normalizations of Eq. (3.4) exist, see below. Periodic variability, e.g., sinusoidal with a single frequency,  $x_h = \sin(2\pi f^* h \Delta t)$ , produces a  $\delta$ -peak located at this frequency,  $f^*$ , in the PSD. While the PSD is thus mainly used to conduct searches for periodic signals in lightcurves, it is clear that it can also be used to evaluate variability characterized by a continuous distribution of frequencies. In section 2.1, e.g., I showed that the short term variability of black hole X-ray binaries in all states is characterized by PSDs dominated by variability components extending over broad frequency ranges.

The statistical uncertainty of the individual, non-averaged, measured PSD values is of the order of the PSD value itself, but in case of averaging, it is reduced by the square root of the averaged independent measurements, see Eq. (3.11) below. Therefore averaging of PSD values plays an important role in the analysis of measured power spectra in order to achieve better signal-to-noise ratios (SNRs). Two different kinds of averaging can be applied: the Fourier frequencies and their corresponding PSD values can be rebinned to a new frequency grid ( $f_j \rightarrow f_k$ ) and/or the final PSD can be obtained by averaging individual PSDs each corresponding to a segment of given length of the original lightcurve. In the former case the frequency resolution is reduced, while in the latter case the minimum accessible frequency is constrained to  $1/T_{\text{seg}}$  instead of extending down to  $1/T$ . Usually, both methods are applied simultaneously. In the following angle brackets are used to denote an average over a finite number,  $M$ , of independent measurements:

$$P_k = \langle P_j \rangle = \langle P \rangle \quad (3.5)$$

In this nomenclature  $M$  is the product of  $M_{\text{seg}}$  lightcurve segments and  $M_f$  Fourier frequencies used to obtain a given  $\langle P \rangle$  value:

$$M = M_{\text{seg}} \times M_f \quad (3.6)$$

The number of averaged lightcurve segments can vary depending on the frequency range under consideration: a few long segments can be produced to reach low frequencies, while PSDs from many short segments can be averaged for maximum SNR at high frequencies. The number of averaged Fourier frequencies can of course also vary depending on which frequency bin  $f_k$  is considered. For the broad band power spectra studied in this work a logarithmic frequency rebinning ( $\Delta f/f = \text{constant}$ ) has proven to be useful. For more details see Nowak et al. (1999a) and chapter 5.

### 3.2.2 Normalizing PSD Values, Background Correction

In X-ray astronomy applications several different normalizations of the power spectral density are useful. They are applied by multiplying the original PSD by a normaliza-

tion factor  $A$ :

$$\langle P_{\text{norm}} \rangle = A \langle P \rangle \quad (3.7)$$

The most important definitions of  $A$  are the following:

$$A = \begin{cases} 1 & \text{unnormalized} \\ \frac{2}{TR} & \text{for Leahy et al. (1983) normalization} \\ \frac{2}{TRR_{\text{sig}}} & \text{for Miyamoto et al. (1992) normalization} \end{cases} \quad (3.8)$$

Above, the distinction between the total time-averaged count rate  $R = \langle x_h \rangle$  of the lightcurve and the average signal count rate  $R_{\text{sig}}$  is made. The latter is obtained by subtracting the average count rate due to the X-ray background level present in measured lightcurves,  $R_{\text{bkg}}$ :

$$R_{\text{sig}} = R - R_{\text{bkg}} \quad (3.9)$$

Only the ‘‘Miyamoto’’ normalization takes the background into account. It has to be applied for large  $R_{\text{bkg}}/R$  ratios. For the *RXTE/PCA* power spectra of Cyg X-1 presented in this work  $R \sim 1000$  cps/PCU<sup>1</sup> and  $R_{\text{bkg}} \sim 20$  cps/PCU, therefore the background correction only influences the PSD normalization on the  $\sim 2\%$  level (application to the monitoring data see chapter 5).

The unnormalized power spectral density is required to calculate higher order Fourier quantities like the coherence function (section 3.4). In ‘‘Leahy’’ normalization the PSD delivers the lightcurve variance or the squared root mean square variability,  $\text{rms}^2$ , per frequency interval, usually expressed in units of  $\text{rms}^2/\text{Hz}$ . In this case Parseval’s theorem can be written in the following simple form:

$$\text{rms}^2 = \langle x_h^2 \rangle - \langle x_h \rangle^2 = \sum_k \frac{2}{T \langle x_h \rangle} \langle P \rangle \Delta f_k \quad (3.10)$$

In this normalization the Poisson noise level is to be found at the value of 2, independent of the source count rate. The ‘‘Miyamoto’’ normalization gives the PSD in units of the squared *fractional* root mean square variability per frequency interval, i.e., the variance that each frequency contributes *in units of the average signal count rate  $R_{\text{sig}}$  of the source*. This normalization is usually given in units of  $(\text{rms}/R_{\text{sig}})^2/\text{Hz}$ . While the Miyamoto normalization allows a better comparison of systematic brightness-independent similarities between different PSDs (shape, fractional variance) and is

<sup>1</sup>The *RXTE/PCA* instrument consists of 5 proportional counter units (PCUs), see section 1.5. Note that in the context of PSD normalization the *summed count rates of all PCUs that were turned on during the observation* have to be used for  $R$ ,  $R_{\text{bkg}}$ , and  $R_{\text{sig}}$ .

therefore most often used, the effects of varying source brightness which might be of interest, e.g. when comparing PSDs from two different BHXRBs or from one BHXRB in different states, are only apparent in Leahy normalization. Note that the expression “squared rms” (or “rms amplitude” or “rms variability”) which has been used in the absolute sense of Eq. (3.10) in this section is often also used for the fractional variability, i.e., meaning  $(\text{rms}/R_{\text{sig}})^2$ .

### 3.2.3 Statistical Uncertainty of the Averaged PSD Values

If the  $x_h$  can be assumed to be approximately normally distributed (e.g., for large  $m$ , “central limit theorem”) which is generally the case, then the PSD values are  $\chi^2$  distributed with two degrees of freedom (van der Klis, 1989). For Poisson noise, the  $1\sigma$  uncertainty of an individual unbinned PSD value can be shown to be of the order of the intrinsic noise PSD value itself: In Leahy normalization Poisson noise has a mean value of 2, independent of frequency (“white noise”). Its uncertainty, being  $\chi^2$  distributed with two degrees of freedom, amounts to  $\sigma(|N_{\text{poisson},j}|^2) = \sqrt{\text{var}(|N_{\text{poisson},j}|^2)} = \sqrt{4} = 2$ . Rebinning reduces  $\sigma$  to  $2/\sqrt{M}$  and approximates a Gaussian distribution again. The corresponding statistical arguments can be adopted for the signal component of the PSD, allowing to express the uncertainty of the measured PSD values as (van der Klis, 1989):

$$\sigma \langle P \rangle = \frac{\langle P \rangle}{\sqrt{M}} \quad (3.11)$$

The same normalization factor as chosen for  $\langle P_{\text{norm}} \rangle$  must of course also be applied to the PSD uncertainty:

$$\sigma \langle P_{\text{norm}} \rangle = A \sigma \langle P \rangle \quad (3.12)$$

### 3.2.4 Noise Component of the PSD and its Deadtime Correction

In order to use the measured PSD,  $\langle |X|^2 \rangle$ , to evaluate and model the source variability, the variability contributed by non-source related noise,  $\langle |N|^2 \rangle$ , has to be determined and removed. From  $S_j = X_j - N_j$  (Eq. 3.3) the unnormalized signal component of the PSD,  $\langle |S|^2 \rangle$ , can be determined as:

$$\langle |S|^2 \rangle = \langle P \rangle - \langle |N|^2 \rangle \quad (3.13)$$

This is approximately correct, since  $X_j$  and  $N_j$  can be assumed to be uncorrelated, thus their averaged cross terms will tend to average out to zero (van der Klis, 1989). Equivalent formulae are of course valid for all normalizations. Due to the statistical uncertainty of the observed noise component, a PSD from which the theoretical noise

level has been subtracted still shows deviations from the signal component. While the expectation value of these deviations is the signal component, its uncertainty is given by the “effective noise level”,  $E$ :

$$E = \frac{1}{\sqrt{M}} \langle |N|^2 \rangle \quad (3.14)$$

As already mentioned, the noise in BHXRB X-ray lightcurves is mainly counting noise. In the different normalizations introduced in section 3.2.2, the frequency-independent Poisson noise level amounts to the following values:

$$\left\langle \left| N_{\text{poisson}} \right|^2 \right\rangle = \left| N_{\text{poisson}} \right|^2 = \begin{cases} TR & \text{unnormalized} \\ 2 & \text{for Leahy et al. (1983) normalization} \\ \frac{2}{R_{\text{sig}}} & \text{for Miyamoto et al. (1992) normalization} \end{cases} \quad (3.15)$$

However, this noise component is modified by the occurrence of deadtime in X-ray detectors, i.e. the time after an X-ray photon triggered the detector during which it cannot register any further photons. For proportional counters like the *RXTE/PCA* instrument, e.g., this is the time elapsing until the electrons generated by an X-ray photon in the detector gas are transported to the anode wires and the detector gas is neutral again. The influence of the deadtime on the counting noise is frequency-dependent (see Eqs 3.16–3.19 below). It has to be taken into account in terms of a correction of the Poisson noise level that is to be removed from the measured PSD. For an individual noise measurement in full Fourier frequency resolution this corrected noise component  $|N_j|^2$  can be written as:

$$|N_j|^2 = |N_{\text{poisson}}|^2 \left( 1 + K_{\text{dead},j} + K_{\text{instr},j} \right) \quad (3.16)$$

As reflected by this equation, the deadtime correction of  $|N_{\text{poisson}}|^2$  can generally be divided into two parts: a functionally instrument-independent contribution,  $K_{\text{dead},j}$ , which is caused by the incident X-ray photons<sup>2</sup>, and an additional, instrument-dependent contribution,  $K_{\text{instr},j}$ . In case of the *RXTE/PCA* instrument, e.g., “very large events” are registered which are causing a different noise influencing kind of deadtime since they appear as “anti-shots” in the lightcurves. They are not included in

<sup>2</sup>More precisely, by those incident X-ray photons that are taken into account in the lightcurve that is Fourier transformed (Zhang et al., 1996). This means that observed photons outside the considered energy range or, e.g., from coincident events, although they are causing the same amount of deadtime, do not have to be considered in the noise correction. This is different when correcting lightcurve count rates or spectra for deadtime, see “*RXTE Cook Book*” ([http://heasarc.gsfc.nasa.gov/docs/xte/recipes/pca\\_deadtime.html](http://heasarc.gsfc.nasa.gov/docs/xte/recipes/pca_deadtime.html))

the measured lightcurve count rates since they are known to be caused by energetic cosmic rays. A measure of these events is provided by the very large event (VLE) count rate, counting cosmic ray events depositing more than a predefined threshold energy in the detector. The measured VLE rate is delivered with each *RXTE/PCA* observation. Thus their deadtime influence can also be corrected. For the following I set

$$K_{\text{instr},j} = K_{\text{vle},j} \quad (3.17)$$

specializing on the *RXTE/PCA* instrument for describing the instrument-dependent part of the deadtime correction.

Analytically, the expectation value of the general (instrument-independent) deadtime modification of the Poisson noise has been thoroughly studied by (Zhang et al., 1995). They discriminate between two possible kinds of deadtime, the paralyzable type (every incident event causes deadtime) and the non-paralyzable type (only detected events cause deadtime). This distinction is insignificant below 10 kHz, however, and is thus not relevant for analyzing BHXRB PSDs (Jernigan, Klein & Arons, 2000). In practical applications, both types, the paralyzable (Jernigan, Klein & Arons, 2000; Nowak et al., 1999a) as well as the non-paralyzable (Zhang et al., 1996) deadtime correction have been used to correct *PCA* PSDs. Jernigan, Klein & Arons (2000) showed that the description of  $K_{\text{dead},j}$  as paralyzable deadtime influence in its basic form – i.e., not taking binning effects into account – is well suited for *PCA* observations comparable to our Cyg X-1 monitoring observations:

$$K_{\text{dead},j} = 2R_{\text{pcu}} \left[ \frac{\sin(2\pi\tau_d f_j)}{2\pi f_j} \right] \quad (3.18)$$

In this equation  $R_{\text{pcu}}$  is the observed count rate *per PCU* and  $\tau_d$  is the detector deadtime which nominally amounts to  $10 \mu\text{s}$  for the *PCA*. Note again that in case of correcting PSDs from selected energy bands,  $R_{\text{pcu}}$  consists only of those events that are part of the discrete Fourier transform, i.e.,  $R_{\text{pcu}}$  is the count rate in the selected energy band (I confirmed this statement of Zhang et al. 1996 using observations from the Cyg X-1 monitoring campaign).

The deadtime correction due to very large events in the *PCA*,  $K_{\text{vle},j}$ , can be calculated by (Zhang et al., 1996; Jernigan, Klein & Arons, 2000):

$$K_{\text{vle},j} = R_{\text{pcu}} R_{\text{vle}} \left[ \frac{\sin(\pi\tau_{\text{vle}} f_j)}{\pi f_j} \right]^2 \quad (3.19)$$

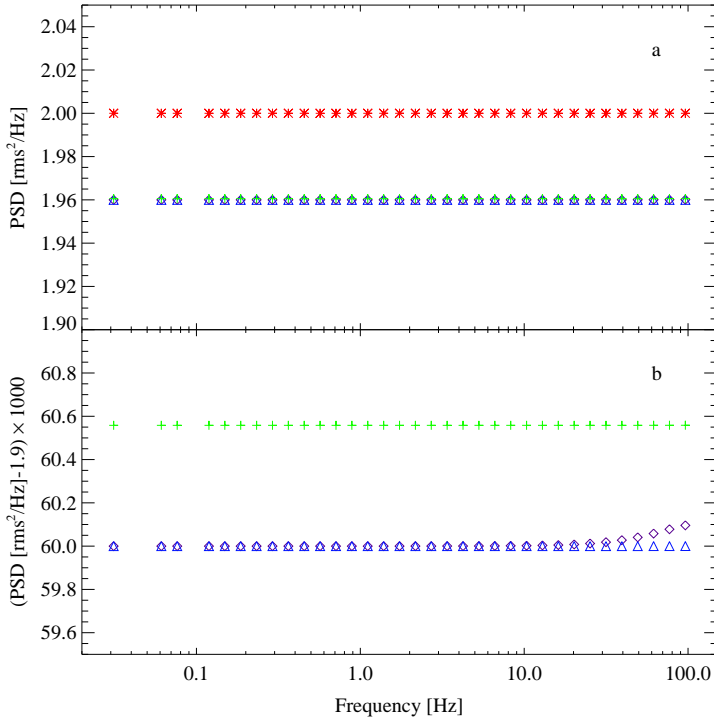


Figure 3.1: **a Red stars:** Pure Poisson noise in Leahy normalization. **Purple Diamonds:** Poisson noise with general deadtime correction; paralyzable with binning effects; Eq. 24 of Zhang et al. (1995); with  $R_{\text{pcu}} = 1000$  cps,  $\tau_{\text{d}} = 10 \mu\text{s}$ ,  $\Delta t = 2^{-8}$  s, and  $m = 8192$ . **Blue Triangles:** Poisson noise with general deadtime correction; paralyzable without binning effects; Eq. (3.18); with  $R_{\text{pcu}} = 1000$  cps, and  $\tau_{\text{d}} = 10 \mu\text{s}$ . **Green Crosses:** Same as blue triangles plus additional VLE correction; Eq. (3.19); with the additional parameters  $R_{\text{vle}} = 75$  cps, and  $\tau_{\text{vle}} = 61 \mu\text{s}$ . **b** Same quantities as shown above but with the y-scale adjusted to emphasize the (small) differences between the noise corrections. The pure Poisson noise is off the scale in this panel. In both panels all noise spectra have been frequency-rebinned to a logarithmically equidistant grid for reasons of clarity.

Here  $R_{\text{vle}}$  is the VLE count rate *per PCU* and  $\tau_{\text{vle}}$  is the deadtime caused by each very large event. The latter depends on the energy threshold that has been set for the observation in question. According to the “*RXTE Cook Book*”, four different settings are possible; the threshold of 75 keV, e.g., corresponds to  $\tau_{\text{vle}} \sim 170 \mu\text{s}$  (Zhang et al., 1996).



Eqs (3.18) and (3.19) have been tested by Jernigan, Klein & Arons (2000) using PSDs observed for the neutron star XRBs GX 17+1 and for Cyg X-1. They model the noise dominated high frequency part of the observed PSDs according to Eqs (3.16)–(3.19)<sup>3</sup> finding good agreement. Therefore, this is the description that was used for noise-subtracting most of the Cyg X-1 monitoring PSDs (see also section 5.1.2). For the more recent observations no usable VLE count rates were available, thus they were corrected taking only  $K_{\text{dead}}$  into account. In this case Eq. (24) of Zhang et al. (1995) – which also takes binning effects into account – was used, confirming again that for the Cyg X-1 PSDs there is no detectable difference to simply using Eq. (3.18) – which does not take binning into account. Fig. 3.1 illustrates the magnitude of the different noise corrections for parameters typical for Cyg X-1 in the frequency range relevant for this work, i.e., below 100 Hz: The deadtime correction reduces the noise level by  $\sim 2\%$  (Fig. 3.1a). The VLE correction only slightly increases the noise level again. This increase amounts to  $\sim 0.03\%$  of the noise level (Fig. 3.1b) and its omission does not significantly influence the PSD analyses presented in this work. The difference in the general deadtime correction according to Eq. (24) of Zhang et al. (1995) and Eq. (3.18) is even smaller (Fig. 3.1b).

### 3.3 The Cross Power Density

#### 3.3.1 Calculating and Averaging the Cross Power Density

Let  $x_{1,h}$  and  $x_{2,h}$  be two equally spaced lightcurves. In the following they are assumed to be the X-ray fluxes observed simultaneously in two different energy ranges for the same source. The cross power density (CPD) is a complex quantity obtained by multiplying the discrete Fourier transforms of the two lightcurves:

$$C_j = X_{1,j}^* X_{2,j} \quad (3.20)$$

As in case of the PSD, an average over lightcurve segments and, if desired, over frequencies is calculated for practical applications:

$$C_k = \langle C_j \rangle = \langle C \rangle \quad (3.21)$$

Contrary to  $\langle P \rangle$ ,  $\langle C \rangle$  is generally a complex quantity. To illustrate this quantity, Fig. 3.2 on page 74 presents vector representations of  $\sum C_j = M \langle C \rangle$ . The magnitude as well as the phase of this complex quantity can be used for timing analysis, leading to the coherence function and the time lag spectrum, respectively. Both allow to compare the short term variations produced in two different energy bands, i.e., to perform combined spectro-temporal analyses.

<sup>3</sup>Their model formally includes another empirical additive noise correction, however, it is consistent with zero for those two sources.

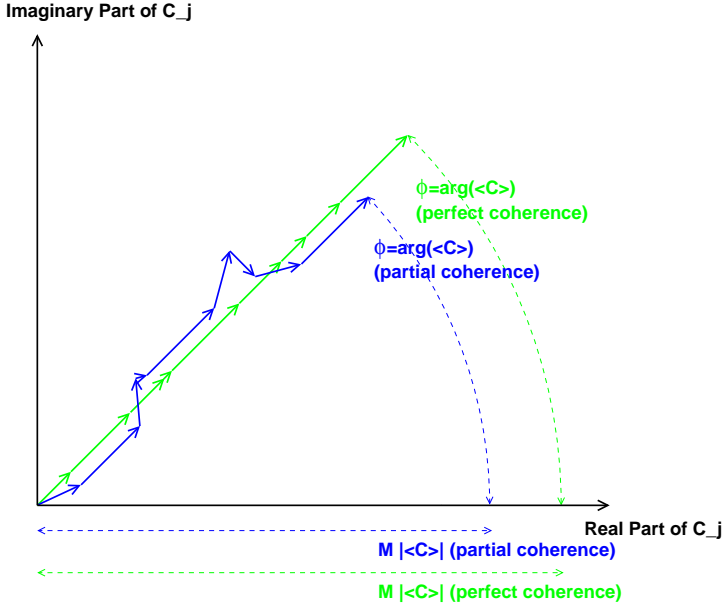


Figure 3.2: Vector representation of the CPD. The average CPD or, more precisely,  $M \langle C \rangle$ , observed for a certain frequency bin  $f_k$  is calculated by summing  $M = M_{\text{seg}} \times M_f$  individual  $C_j$  vectors. The case of perfect coherence (green,  $\gamma_k^2 = 1$ ), is compared to the case of partial coherence (blue,  $\gamma_k^2 < 1$ ). For partial coherence a decreased CPD magnitude,  $M |\langle C \rangle|$ , is observed and an uncertainty in CPD phase,  $\arg(\langle C \rangle)$ , is introduced, leading to decreased coherence values and to time lag uncertainties.

### 3.4 The Coherence Function

#### 3.4.1 Calculating the Coherence Function

The coherence function is calculated by dividing the observed squared magnitude of the average CPD,  $|\langle C \rangle|^2$ , by the *signal PSDs*,  $\langle |S_1|^2 \rangle$  and  $\langle |S_2|^2 \rangle$ , of the two lightcurves:

$$\gamma_k^2 = \frac{|\langle C \rangle|^2}{\langle |S_1|^2 \rangle \langle |S_2|^2 \rangle} \quad (3.22)$$

This means that  $|\langle C \rangle|^2$  is compared to its maximal possible value which could be reached in case of a noiseless signal for constant phase values for all  $C_j$  (Fig. 3.2, green vectors), i.e., perfect intrinsic coherence. If the measured  $C_j$  were indeed noiseless (Fig. 3.2, blue vectors)  $\gamma_k^2$  can assume values between 0 and 1. In reality, counting

noise causes a comparatively larger squared *magnitude*  $|\langle C \rangle|^2$  and thus  $\gamma_k^2 > 1$  is possible. This is true even though the random *phase* of counting noise reduces coherence. If the noise is also taken into account in the denominator (Eq. 3.33), than 1 is again the maximum possible value. The coherence is a measure of the degree of linear correlation, in the fractional mean-squared sense, between the two measured lightcurves in a given frequency bin  $f_k$  (Nowak et al., 1999a). A mathematical description of such correlations based on transfer functions can be found in Vaughan & Nowak (1997) or Bendat & Piersol (1986).

### 3.4.2 Noise Component of the Coherence

In order to perform a noise correction for  $\gamma_k^2$ , the squared magnitude of the observed average CPD has to be noise-corrected. In terms of signal and noise Fourier transforms of the two lightcurves  $|\langle C \rangle|^2$  can be written as:

$$\begin{aligned} |\langle C \rangle|^2 &= |\langle X_1^* X_2 \rangle|^2 \\ &= |\langle (S_1^* + N_1^*)(S_2 + N_2) \rangle|^2 \\ &= |\langle S_1^* S_2 \rangle + \langle S_1^* N_2 \rangle + \langle N_1^* S_2 \rangle + \langle N_1^* N_2 \rangle|^2 \end{aligned} \quad (3.23)$$

Instead of being based on  $|\langle X_1^* X_2 \rangle|^2$  – like the observed coherence  $\gamma_k^2$  – the noise-corrected signal coherence  $\gamma_{\text{sig},k}^2$  is based on  $|\langle S_1^* S_2 \rangle|^2$ . This quantity has therefore to be extracted from Eq. (3.23). Vaughan & Nowak (1997) demonstrate how this can be achieved under certain conditions by defining the auxiliary quantity  $q_k^2$ :

$$q_k^2 = \frac{1}{M} (\langle |S_1|^2 \rangle \langle |N_2|^2 \rangle + \langle |N_1|^2 \rangle \langle |S_2|^2 \rangle + \langle |N_1|^2 \rangle \langle |N_2|^2 \rangle) \quad (3.24)$$

In the following the approximate noise correction for the case of high powers and high measured coherence, as appropriate for Cyg X-1 over a large frequency range (Figs. 3.3 and 3.4), is given. The conditions of high powers and high measured coherence translate into:

$$\frac{\langle |S_{1,2}|^2 \rangle}{\langle |N_{1,2}|^2 \rangle} > \frac{B}{\sqrt{M}} \quad \text{and} \quad \gamma_k^2 > \frac{Bq_k^2}{\langle |S_1|^2 \rangle \langle |S_2|^2 \rangle} \quad (3.25)$$

If  $B$  is of the order of a few or larger, the separation of Eq. (3.24) is possible:

$$|\langle C \rangle|^2 = |\langle S_1^* S_2 \rangle|^2 + q_k^2 \quad (3.26)$$

Thus, the noise-corrected signal coherence can be written as:

$$\gamma_{\text{sig},k}^2 = \frac{|\langle C \rangle|^2}{\langle |S_1|^2 \rangle \langle |S_2|^2 \rangle} - \frac{q_k^2}{\langle |S_1|^2 \rangle \langle |S_2|^2 \rangle} = \frac{|\langle C \rangle|^2 - q_k^2}{\langle |S_1|^2 \rangle \langle |S_2|^2 \rangle} \quad (3.27)$$

### 3.4.3 Statistical Uncertainty of the Coherence Values

The interesting uncertainty for the analysis of source variability is of course the uncertainty of  $\gamma_{\text{sig},k}^2$ , the noise-corrected signal coherence (noise correction see following section). Like the uncertainty of the *noise-corrected* signal PSD<sup>4</sup>,  $\langle |S|^2 \rangle$ , which can be given as  $\langle P \rangle / \sqrt{M} = (\langle |S|^2 \rangle + \langle |N|^2 \rangle) / \sqrt{M}$ , this uncertainty consists of an intrinsic contribution sufficient only for a *noiseless* signal determination and of a noise contribution. The intrinsic coherence uncertainty is given by Bendat & Piersol (1986) as:

$$\sigma \gamma_{\text{int},k}^2 = \left( \frac{2}{M} \right)^{1/2} \frac{1 - \gamma_{\text{sig},k}^2}{|\gamma_{\text{sig},k}|} \quad (3.28)$$

In the case of high powers and high measured coherence, the uncertainty of the *noise-corrected* signal coherence,  $\sigma \gamma_{\text{sig},k}^2$ , can be approximated by the sum of the uncertainty of *noiseless* signal coherence measurements,  $\sigma \gamma_{\text{int},k}^2$ , plus additional terms due to Poisson noise (Vaughan & Nowak, 1997):

$$\sigma \gamma_{\text{sig},k}^2 = \frac{\gamma_{\text{sig},k}^2}{\sqrt{M}} \left[ \frac{2q_k^4 M}{(|\langle C \rangle|^2 - q_k^2)^2} + \frac{\langle |N_1|^2 \rangle^2}{\langle |S_1|^2 \rangle^2} + \frac{\langle |N_2|^2 \rangle^2}{\langle |S_2|^2 \rangle^2} + \frac{M(\sigma \gamma_{\text{int},k}^2)^2}{(\gamma_{\text{sig},k}^2)^2} \right]^{1/2} \quad (3.29)$$

Vaughan & Nowak (1997) also present equivalent formulae for  $\gamma_{\text{sig},k}^2$  and  $\sigma \gamma_{\text{sig},k}^2$  in the case of high powers and low measured coherence.

## 3.5 The Lag Spectrum

### 3.5.1 Calculating the Phase- and Time Lags

The argument of the cross power density  $C_j$  is the phase difference between  $X_{1,j}$  and  $X_{2,j}$ , i.e., between intensity fluctuations in the two energy bands at frequency  $f_j$ . In its averaged form (see Fig. 3.2) the phase lag is given by:

$$\phi_k = \arg(\langle C \rangle) \quad (3.30)$$

By relating the phase lag to its associated frequency,  $f_k$ , it can be converted into a time delay:

$$\delta t_k = \frac{\phi_k}{2\pi f_k} \quad (3.31)$$

---

<sup>4</sup>This is the same uncertainty as for the non-noise-corrected quantity,  $\langle P \rangle$ , itself (Eq. 3.11). Note, however, the presence of the effective noise level after noise correction (Eq. 3.14).

Both forms, the phase lag and time lag have been presented in analyses of the short term variability of BHXRBs. In this work I concentrate on the time lag, therefore the remaining equations of this chapter are given in time lag notation. Note that for practical applications  $X_{1,j}$  is associated with the softer energy band and  $X_{2,j}$  with the harder energy band. Thus a positive time lag is measured when the fluctuations in the hard emission are delayed with respect to those in the soft band and vice versa.

### 3.5.2 Noise Estimation

While measurement noise changes the expectation value of PSD values as well as of coherence values, its contribution to the phase of the CPD is completely random (Nowak et al., 1999a). It does not change the expectation value of the phase but enhances its uncertainty (see next section). Based on Poisson noise and an  $A^2 f_k^{2\alpha}$  power law PSD, Nowak et al. (1999a) develop an approximation of the noise related uncertainty that is depending on source parameters, the amount of logarithmic frequency rebinning, and the total exposure time:

$$\sigma(\delta t_k) \approx \frac{\pi^{-1} |A|^{-1}}{\sqrt{R \gamma_k^2 d \times T}} f_k^{\alpha-3/2} \quad (3.32)$$

Assuming typical source values for  $R$ ,  $\gamma_k^2$ ,  $|A|$ ,  $\alpha$ , and a given frequency bin width  $d = df/f$ , this expression can be compared to an assumed intrinsic time lag spectrum. It can thus be used to estimate the frequency range over which – for a given exposure time  $T$  – the time lags will not be noise dominated. Note that Eq. (3.33) is less suited for such a task because of the strong frequency dependence of  $g_k^2$  as compared to  $\gamma_k^2 \sim 1$ . In case of the 20 ks Cyg X-1 *RXTE/PCA* observation studied by Nowak et al. (1999a) the usable frequency range turns out to be 0.1–30 Hz. Most of the monitoring observations presented in this work correspond to a comparable but slightly smaller range (see, e.g., Fig. 3.5).

### 3.5.3 Statistical Uncertainty of the Time Lags

An uncertainty in the phase is introduced whenever there is a deviation from perfect coherence either due to partial intrinsic coherence as illustrated in Fig. 3.2 and/or due to measurement noise. The latter is providing random phase contributions to the CPD vector sum. In contrast to the situation shown in Fig. 3.2, however, measurement noise also introduces a change in the *magnitude* of the cross power density (making the noise correction of  $\gamma_k^2$  necessary, Eq. (3.29)). This has to be taken into account in the determination of the phase lag uncertainty. The definition of perfect coherence in this case includes the noise terms: the magnitude of the cross power density is compared to its *overall* maximum value  $\langle P_1 \rangle \langle P_2 \rangle$  (and not to  $\langle |S_1|^2 \rangle \langle |S_1|^2 \rangle$ ). The

uncertainty of the time delay is thus based on  $g_k^2$ , a quantity closely related to the coherence function  $\gamma_k^2$ :

$$\sigma(\delta t_k) = \frac{1}{\sqrt{M}2\pi f_k} \sqrt{\frac{1 - g_k^2}{2g_k^2}} \quad \text{where} \quad g_k^2 = \frac{|\langle C \rangle|^2}{\langle P_1 \rangle \langle P_2 \rangle} \quad (3.33)$$

### 3.6 Example: Cygnus X-1, IDL Tools

The power spectra of X-ray binaries have been studied since the early times of X-ray astronomy (e.g., by Weisskopf, Kahn & Sutherland, 1975; Weisskopf & Sutherland, 1978; Weisskopf et al., 1978) and although no physical model exists so far (section 2.3), numerous observational and model PSDs of numerous X-ray binaries have been presented. Until very recently this has not been the case for the cross-energy statistics – the coherence function and the time lags – since they require higher SNR lightcurves than PSDs. Miyamoto et al. (1988) reported frequency dependent time lags from one Ginga observation of Cyg X-1, but only the publications of Vaughan & Nowak (1997), Cui et al. (1997) and Nowak et al. (1999a) triggered the “boom” for studying these quantities. Since then, time lags (and more seldomly the coherence function) of several black hole and neutron star binaries have been presented (e.g., by Ford et al., 1999; Cui, Zhang & Chen, 2000; Reig et al., 2000; Munro et al., 2001). As I mention in section 2.3 these quantities play a crucial role in improving current accretion models. One of the main objectives of monitoring Cyg X-1 (section 1.5) – and the one this work concentrates on – has been to monitor these Fourier quantities in the hard state, when the short term variability is strongest. Chapters 4 and 5 present the monitored quantities and discuss their implication for current accretion models in detail.

In order to analyze the more than 130 *RXTE* monitoring observations of Cyg X-1 in multiple energy bands, I developed a set of programs using the “Interactive Data Language” environment (IDL 5.0). All the Fourier analysis tools used in the following are available in electronic form (<http://astro.uni-tuebingen.de/software/idl/aitlib>). The most important features of these tools are:

- Simultaneous observation times are selected from all energy bands for which lightcurves have been extracted. From the resulting lightcurves equally-binned lightcurve segments (= containing no gaps) are created.
- Averaged (over lightcurve segments and frequencies) power spectra, time lags, coherence functions are calculated in several energy bands, together with their uncertainties and noise components. In case of the PSD, a complex dead

time correction of the noise component can be performed, where additional *RXTE/PCA* or *RXTE/HEXTE* dead time effects can be included.

- All data products are stored in a standard binary data format (“xdr”), and are thus portable between machines with a different floating point representation.
- The analysis can be performed automatically for a large set of *RXTE* observations. These tools have also been applied to other sources than Cyg X-1: Kalemci et al. (2001) and Kalemci et al. (2002) use them for their timing analysis of the BHXRBs XTE J1550–564 and XTE J1650–500.
- The individual steps in the automatic analysis (e.g., the lightcurve segmenting or the PSD deadtime correction) correspond to modular tools. Many are instrument independent, i.e., they can also be used for lightcurve data from other instruments than *RXTE*.

The *RXTE/PCA* data modes were of course selected to be uniform over the monitoring campaign, allowing to define ranges of detector PHA (= pulse height analyzer) channels for the extractions that contain approximately the same count rates. Translated into absolute energy values these channel ranges correspond approximately to the energy bands 2–4.1 keV, 4.1–6.3 keV, 6.3–8.4 keV, 8.4–13.1 keV, 13.1–74 keV, and 74–100 keV, with the highest band being background dominated for Cyg X-1. For the details concerning the conversion of extracted *PCA* detector channels into physical energies see [http://heasarc.gsfc.nasa.gov/docs/xte/e-c\\_table.html](http://heasarc.gsfc.nasa.gov/docs/xte/e-c_table.html). Figs. 3.3–3.5 demonstrate the application of the described Fourier analysis tools to a typical Cyg X-1 *RXTE/PCA* monitoring observation. This is a  $\sim 6.5$  ks exposure performed on 1999 August 16, which was randomly selected as an example for a typical hard state observation. Is not special in terms of SNR or source state. Based on these figures I will summarize special features of the three Fourier statistics described earlier in this chapter as well as provide a more quantitative description of them for the case of Cyg X-1, as compared to the general hard state overview of chapter 2.

Fig. 3.3a displays the Miyamoto-normalized power spectrum (Eq. 3.7 with background correction, Eq. 3.9) in the lowest energy band (for the small energy dependence of the hard state PSD see chapter 5). Blue dots are the PSD values before, red diamonds after noise subtraction (Eq. 3.13 with deadtime correction, Eq. 3.16) and frequency rebinning (Eq. 3.5). The normalized and rebinned uncertainties are also shown (Eqs 3.11 and 3.12). In this observation the power spectrum is flat down to  $10^{-3}$  Hz and the break frequency lies around 0.3 Hz. It is clear that the decline towards higher frequencies is not simply of power law form: breaks can be identified by eye around  $\sim 3$  Hz and  $\sim 10$  Hz, and probably an additional broad component is present at  $\sim 40$  Hz. This substructure is modeled in chapter 5. The signal power

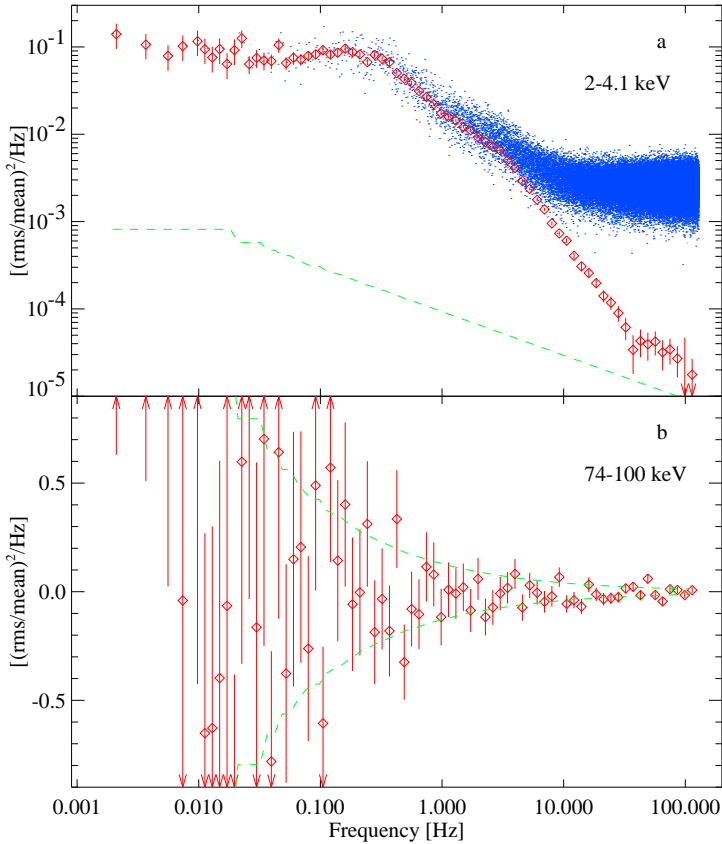


Figure 3.3: Typical power spectra observed during the Cyg X-1 monitoring campaign (1999 August 16), shown for the energy ranges **a** 2–4.1 keV and **b** 74–100 keV. In both panels the red diamonds give the *noise-corrected*, frequency-rebinned PSD values and the green dashed lines represent the effective noise level. The upper panel additionally displays the *non-noise-corrected* PSD in full Fourier frequency resolution. The error bars on the latter have been omitted for reasons of clarity. All quantities have been averaged over lightcurve segments of 512 s length each.

lies above the effective noise level for frequencies up to 100 Hz (green dashed line, Eq. 3.14). That the noise correction is in good agreement with the theoretically expected effective noise level can be seen in Fig. 3.3b: for the background dominated energy band, the PSD is expected to be noise dominated and the noise subtracted PSD



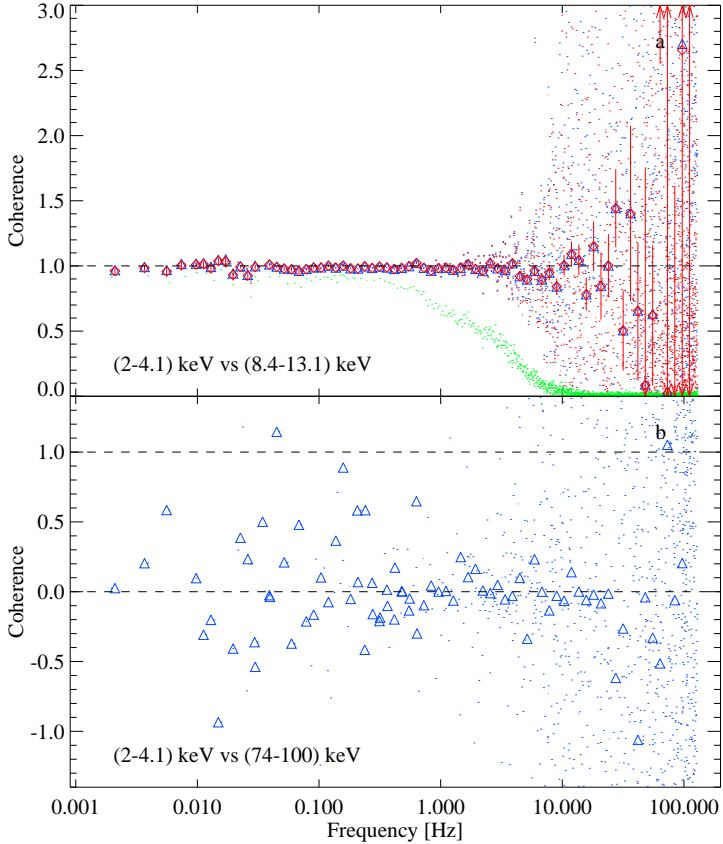


Figure 3.4: Typical coherence functions observed during the Cyg X-1 monitoring campaign (1999 August 16), **a** between the 2–4.1 keV and the 8.4–13.1 keV energy bands and **b** between the 2–4.1 keV and the 74–100 keV energy bands. Blue triangles: the frequency-rebinned, *non-noise-corrected* coherence values, Blue dots: unbinned data. In panel a the red diamonds give the frequency-rebinned, *noise-corrected* coherence values and their associated uncertainties. Its full Fourier frequency resolution is also shown (red dots). Finally, panel a contains the coherence normalized to the observed power spectra ( $g_k^2$ ) instead of to the signal powers ( $\gamma_k^2$ ). All quantities have been averaged over lightcurve segments of 32 s, 128 s, and 512 s length in the frequency ranges 0.001–0.03 Hz, 0.03–0.2 Hz, and 0.2–128 Hz, respectively.

(red diamonds) has to vary within the effective noise level (green dashed line).  
 Fig. 3.4a displays the coherence between the 2–4.1 keV and the 8.4–13.1 keV energy

bands. It is generally high, from  $\sim 0.01$  Hz up to several Hz it is consistent with perfect coherence<sup>5</sup>. For the given exposure time it can be reliably determined up to  $\sim 10$  Hz where it is still  $> 0.8$ . Red diamonds denote the noise-corrected coherence values (Eq. 3.27) with their associated uncertainties (Eq. 3.29), while blue triangles give the non-noise-corrected coherence (Eq. 3.22). Both quantities are also shown in their full Fourier frequency resolution (recall that the frequency-rebinned values *must not be obtained by simply averaging these quantities* over frequencies, see structure of Eq. 3.22). The influence of the noise correction is small: while the difference in the frequency-rebinned values cannot be seen by eye, careful inspection of the resolved dots shows that the corrected values (red) display a lower coherence. The low amount of noise correction is due to the fact that the “observed” coherence  $\gamma_k^2$  (as defined by Eq. 3.22) is in fact already partially noise corrected since the product of the *signal* PSDs,  $\langle |S_1|^2 \rangle \langle |S_2|^2 \rangle$ , is used in the denominator. In order to look at an “honest” *observed* quantity, one has to turn to  $g_k^2$  (Eq. 3.33), the quantity that also determines the uncertainty of the phase measurement. In that case the denominator is given by  $\langle P_1 \rangle \langle P_2 \rangle$ , the non-noise-corrected power spectra. For a comparison  $g_k^2$  is also shown in Fig. 3.4a (green dots, Fourier frequency resolved), making clear that the essential part of the noise correction is already incorporated in  $\gamma_k^2$ ! Fig. 3.4b shows the non-noise-corrected coherence between the 2–4.1 keV and the 74–100 keV energy band. Since the latter is the background dominated band, zero coherence is expected – which is nicely confirmed by the figure. The noise-corrected coherence is not shown in this case since Eq.s (3.27) and (3.29) are only valid for high measured coherence and high signal powers in both channels.

Fig. 3.5a displays the time lags between the 2–4.1 keV and the 13.1–74 keV energy bands. The frequency averaged values and their uncertainties as well as the full resolution are plotted (Eq.s 3.31 and 3.33). As already mentioned in chapter 2, the fluctuations of the hard X-ray emission are delayed compared to those of the soft X-ray emission. According to observations of Cyg X-1 this should be true in the canonical hard, soft, and intermediate state. There are BXRBs, e.g., the microquasars GRS 1915+105 and XTE J1550–564, where negative time lags have also been observed, however those are usually not associated with canonical states (Cui, Zhang & Chen, 2000). In case of Cyg X-1 the time lag spectrum shows a strong frequency dependence in the form of an  $\sim f^{-0.7}$  power law<sup>6</sup> decline from  $\sim 0.1$  s at 0.1 Hz down to a few milliseconds at 10 Hz. This is also roughly the frequency range accessible with our  $\sim 2$ –10 ks (after data screening) long exposures. Outside this range the time lag spectrum is noise-dominated (section 3.5.2). The exact time lag values and non-

<sup>5</sup>The slightly lower coherence at low and high frequencies in the observation presented by Nowak et al. (1999a) is not due to differences in the noise correction but is nicely reproduced by the IDL tools used here when applied to that observation

<sup>6</sup>Note that the phase lag is only weakly frequency dependent.

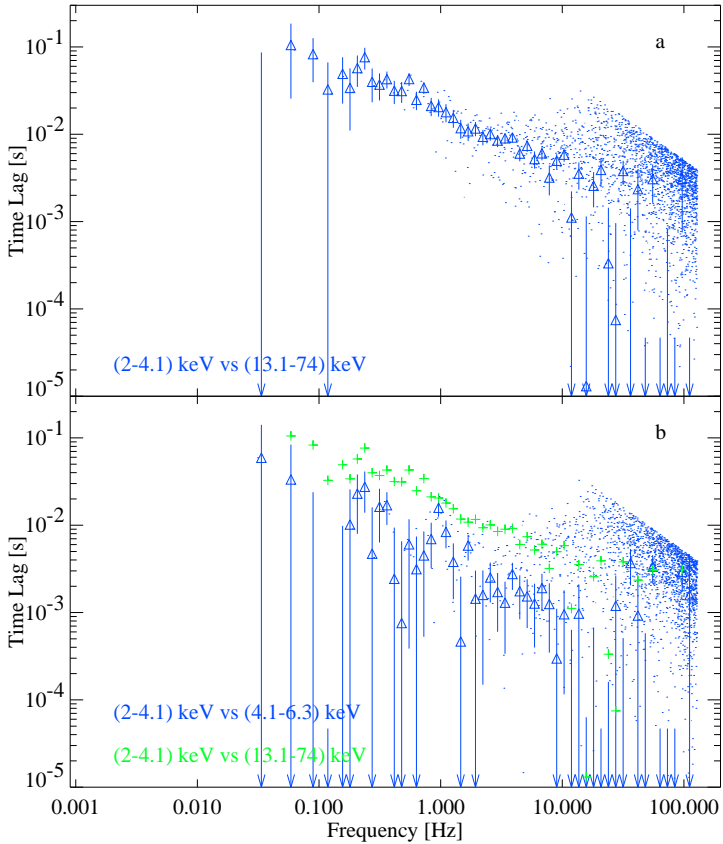


Figure 3.5: Typical time lag spectra observed during the Cyg X-1 monitoring campaign (1999 August 16), **a** between the 2–4.1 keV and the 13.1–74 keV energy bands and **b** between the 2–4.1 keV and the 4.1–6.3 keV energy bands. Panel b also redisplayes the data from panel a to allow a better comparison (green crosses). In both panels the blue triangles give the frequency-rebinned time lag values with their associated uncertainties. The blue dots represent the same quantity but in full Fourier frequency resolution. Recall that no noise correction is performed for time lag spectra. All quantities have been averaged over lightcurve segments of 128 s length each.

noise-dominated frequency intervals are of course depending on the energy bands that are considered: being based on the same low energy band (2–4.1 keV) and comparing the time lags between that band and two different high energy bands (4.1–6.3 keV and

13.1–74 keV) Fig. 3.5b demonstrates that for the larger energy gap the time lags are larger by a factor of  $\sim 4$ . Since qualitatively such a decrease can be expected if the time lags are associated with the time spent in the upscattering corona, it triggered the original interpretation in terms of Comptonization lags, although the details of the energy dependence ( $a(f) \times \ln(E_2/E_1)$  instead of  $\text{constant} \times \ln(E_2/E_1)$ ), as well as the frequency dependence (power law instead of constant) are not consistent with the usual Comptonization models (Miyamoto & Kitamoto, 1989; Nowak et al., 1999a). Note that similar to the power spectrum the time lag spectrum shows characteristic substructure (“shelves”).

The following two chapters present the results obtained from applying the timing tools described in sections 3.1–3.5 to our Cyg X-1 monitoring observations and additional public observations (1996 soft state). For each of the observations power spectra in approximately the energy bands given earlier in this section as well as coherence functions and time lags between all energy band combinations were obtained, of which Figs. 3.3–3.5 provide typical examples. Chapter 4 concentrates on the time lag evolution during the 1996 soft state and the monitoring observations of 1998. Comparing them, so far unknown state dependences were found which are presented in chapter 4 together with a possible production mechanism for enhanced lags. The following chapter 5 concentrates on modeling the power spectra observed from 1998–2002 with discrete Lorentzian components. With the results from this modeling and further temporal (time lags), spectral (power law indices), multi-wavelength (radio flux evolution), and multi-source (GX 339–4, XTE J1650–500) information, the physical scenario suggested in section 4.3 is strengthened (section 6.3). Chapter 4 is based on Pottschmidt et al. (2000), while chapters 5 and 6 are based on (Pottschmidt et al., 2002).

## CHAPTER 4

---

# Temporal Evolution of X-ray Lags in Cygnus X-1

In this chapter the results of the first year of the campaign, i.e., from the weekly  $\sim 3$  ks pointings 1998, as well as from the 1996 soft state are presented, focusing on the evolution of the X-ray time lags. Since the following is based on a publication (Pottschmidt et al., 2000) it adopts the self-contained structure as well as the “we-style” of that work. In the first section the data extraction as well the analysis methods are described as they have been applied for this subset of *RXTE* data (section 5.1). Then the temporal behavior of Cyg X-1 during 1998 is compared to that seen during the 1996 soft state (section 4.2). Specifically, we show that large X-ray lags appear to be associated with *transitions* between the soft and hard state, but *not* with the state itself. In section 4.3 we discuss implications for the accretion models in galactic black hole candidates. The conclusions of this lag study are confirmed by the results from the PSD modeling (chapter 5) and in conjunction with those results the suggested accretion scenario is further constrained in section 6.3.

### 4.1 Observations and Data Analysis

The *RXTE* data presented here were obtained with the Proportional Counter Array (*PCA*; Jahoda et al., 1996) and with the All Sky Monitor (*ASM*; Remillard et al., 1997). We used the standard *RXTE* data analysis software, ftools 4.2. A log of the observations is presented in Table 1 of Pottschmidt et al. (2000), which is available in electronic form from the Centre de Données Stellaires (CDS). The data were reduced using the procedures described in detail in our analysis of the *RXTE* observations of GX 339–4 (Wilms et al., 1999). Intervals with large background flux were removed after visually inspecting the “electron ratio”. As a result of the data screening,  $\sim 2$  ks of usable data were left for each of the 3 ks monitoring observations. We then extracted lightcurves with a resolution of 16 ms for three energy bands ( $\lesssim 4$  keV,  $\sim 8$ –13 keV, and 18.3–72.9 keV)<sup>1</sup>. The computation of the time lags for these energy bands

---

<sup>1</sup>Since the *PCA* data modes used to obtain the 1996 data differ from those used in 1998, it was impossible to use identical energy bands for all observations. The bands used to compare the 1996 data to the

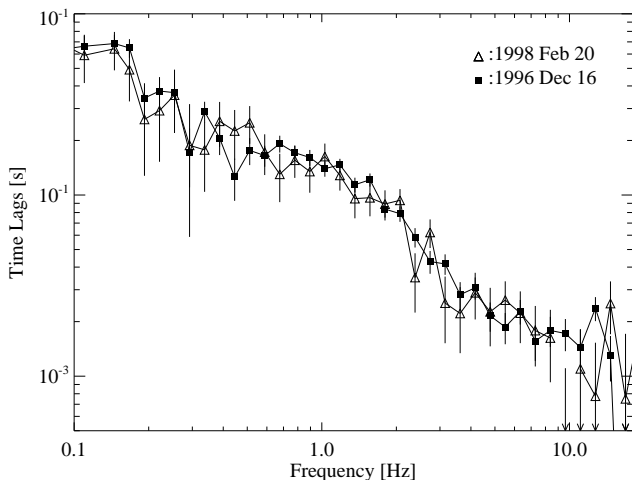


Figure 4.1: Comparison of the X-ray lag spectrum for one of the 3 ks monitoring observations of 1998 with that obtained for  $\sim 30$  ks of the *RXTE* observation of 1996 December 16. The lags have been measured between  $\lesssim 4$  keV and  $\sim 8$ –13 keV. Both examples are typical hard state observations.

follows Nowak & Vaughan (1996) and Nowak et al. (1998).

According to our previous experience, the methods used to compute the uncertainty of the time lag spectrum are applicable over a large range of source fluxes and exposure times. Since most of the 1998 observations were quite short, however, we independently verified the determination of the lag in these cases by comparing them to much longer observations. As an example, Fig. 4.1 displays the time lag spectra for two *RXTE* observations spaced by 1.25 years. Taking the much larger uncertainty from the short observation into account, the overall agreement is excellent. To further increase the signal to noise ratio in the lag determination we rebinned the X-ray lag spectrum into five frequency bands.

## 4.2 Temporal Evolution of the Lags

In Fig. 4.2 we display the evolution of the average time lag for three representative frequency bands and the *RXTE*/*ASM* count rate. The figure shows that a clear long

1998 data were the closest matches possible (the highest energy band is unavailable for some of the 1996 soft state data). The detailed bands are given in Table 1 of Pottschmidt et al. (2000) which is available from the CDS.

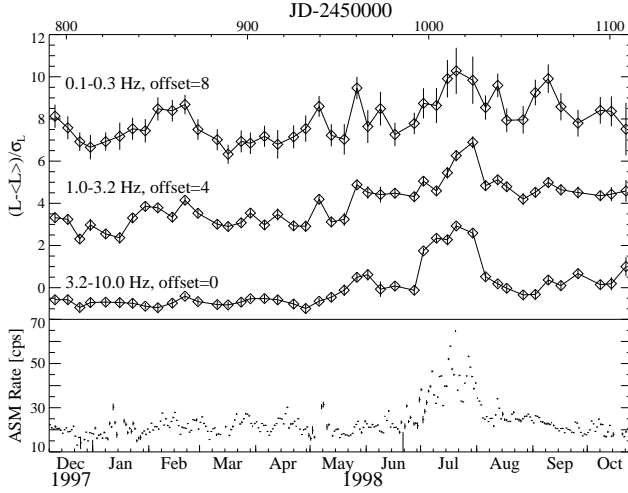


Figure 4.2: Diamonds: Temporal evolution of the average lag between  $\lesssim 4$  keV and 18.3–72.9 keV for the indicated frequency intervals. The deviation of the lag from its mean value as determined from all observations of 1998 for the respective frequency band, in units of its standard deviation is shown. Dashes: *RXTE*/ASM 2–10 keV count rate binned to a resolution of 1 d.

term variability of the lags is present during 1998. For frequencies above  $\sim 1$  Hz, the mean lag is significantly *larger* during the interval in 1998 July that is characterized by a larger ASM count rate. At lower frequencies the fractional change of the lag decreases (Fig. 4.2). This tendency is a consequence of the temporal evolution of the shape of the lag spectrum as characterized by its rough  $f^{-\alpha}$  proportionality: During 1998 July,  $\alpha \sim 0.6$ , compared to its usual value of  $\alpha \gtrsim 0.7$  (Nowak et al., 1998).

Compared to the hard state, intervals like 1998 July show an increased disk contribution to the X-ray spectrum (Zdziarski, Lubiński & Smith, 1999; Gilfanov, Churazov & Revnivtsev, 1999) and have often been associated with “failed state transitions”. One would expect the lag behavior to show the same tendency as during a successful state transition. At first glance, the 1996 data presented by Cui, Zhang & Chen (1998) suggest that we should expect the 1998 July lags to *decrease* during this interval. This contradicts our results (Fig. 4.2). We therefore went back to the 1996 soft state data and applied the same analysis as for the 1998 data. We also computed X-ray lags for two observations performed after the 1996 soft state, one in 1996 October (Dove et al., 1998; Nowak et al., 1998), as well as the one in 1996 December (Focke, 1998). Fig. 4.3 shows the absolute values of the average lag between  $\lesssim 4$  keV and  $\sim 8$ –13 keV

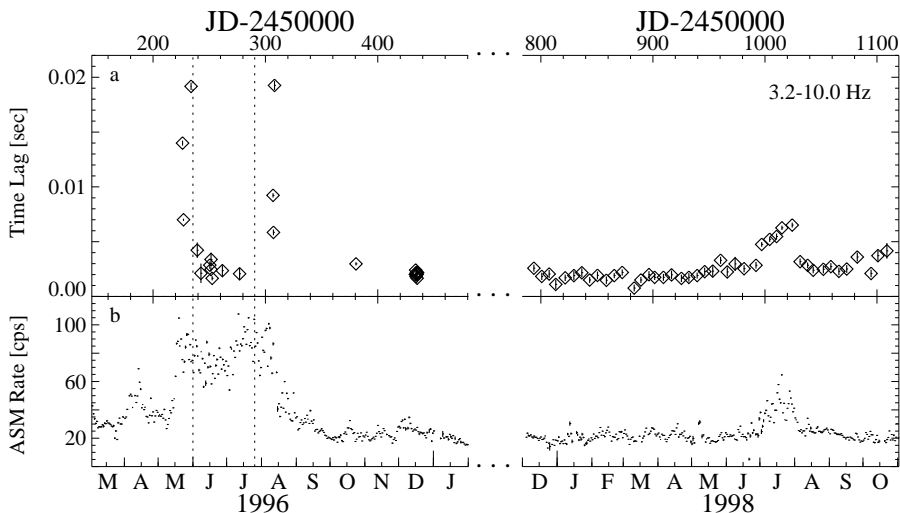


Figure 4.3: **a** Temporal evolution of the absolute value of the average lag between  $\lesssim 4$  keV and  $\sim 8$ –13 keV in the 3.2 to 10 Hz band and **b** ASM count rate for 1996 and 1998. The dotted lines denote the 1996 soft state.

for 1996 and 1998. The lags are indeed longer during the state transitions than in the soft state, however, during the soft state itself, the absolute value of the X-ray lag equals that of the hard state. In fact, the frequency dependence of the lag is very similar for the soft and hard state (Fig. 4.4b). Previous analyses of two hard state observations already suggested that the soft and hard state lags might not be so different as previously thought (Cui, 1999). Our numerous hard state monitoring observations now clearly indicate that *the X-ray lag spectrum of Cyg X-1 is rather independent of the spectral state. The enhanced lags are then associated with transition or failed transition intervals, and not with the state of the source itself.*

### 4.3 Discussion and Conclusions

In Fig. 4.4a we display examples for the whole range of lag spectra present in this analysis. Taking the shape of the typical hard state lag spectrum as a baseline, the lag is significantly longer during the 1998 July failed state transition. The frequency range from 1 to 10 Hz exhibits these changes most prominently. During the hard to soft transition in 1996 May, the lag is longer by almost a factor 10 at 6 Hz. As already shown in section 4.2, these results indicate that the magnitude and shape of the X-ray



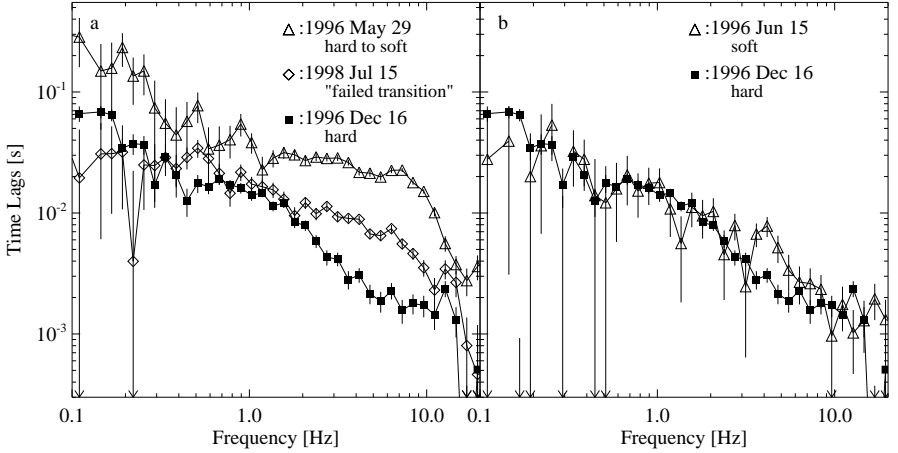


Figure 4.4: X-ray lag spectra between  $\lesssim 4$  keV and  $\sim 8$ –13 keV. **a** Comparison of the hard to soft state transition, the 1998 July transitional state, and the typical hard state. **b** Comparison of the 1996 soft state and the hard state.

lag spectrum in Cyg X-1 is related to the state transitions.

Previous models for the generation of the X-ray lags assumed more or less static media to produce the X-ray lag by scattering of seed photons in a Comptonizing medium. The size of the region required to produce the observed lags in such a model is large ( $\gtrsim 300$  gravitational radii; Nowak et al., 1999b). Such a large size simplifies models in which the soft state Compton corona is much smaller than the hard state corona, as had been initially inferred from the 1996 soft state lags and spectral shape. Indirect evidence for the change of the size of the X-ray emitting corona has also been presented by Zdziarski, Lubiński & Smith (1999), Gilfanov, Churazov & Revnivtsev (1999), and commented on by di Matteo & Psaltis (1999), with the latter authors suggesting an upper limit for the hard state coronal radius of  $\sim 30$  gravitational radii. Zdziarski (1998) suggested that in the hard state of GX 339–4 there is a correlation between the X-ray power law photon index and the fraction of this power law that is reflected by cold material. Specifically, they suggested that softer power laws implied greater reflection, which implies smaller coronae in certain models. Within the hard state, softer power laws are associated with higher luminosities, implying again that the corona is shrinking as the source goes from the hard to the soft state. Our data clearly show that the soft and hard state lag spectra are very similar. This makes the geometrical interpretation of the lags in terms of Comptonization models alone difficult. We therefore need to look for other models to explain the observed lags. In

the following we present a qualitative picture, based on recent observational results. Note, however, that a detailed theoretical model is beyond the scope of this chapter.

In recent years, evidence has emerged that the state transitions are not solely an X-ray phenomenon. Studies of Cyg X-1 and GX 339–4 have revealed that in the hard state the X-ray and radio behavior is correlated (Brocksopp et al., 1999a; Corbel et al., 2000). In GX 339–4, there is strong evidence that the source is radio quiet during the soft state (Fender et al., 1999). At least in one case, optically thin radio flares accompanied the state transition. In Cyg X-1, no radio data are available for the soft state. The end of the 1996 soft state as well as the 1998 July “failed state transition”, however, coincided with radio flares (Zhang, Cui & Chen, 1997; Brocksopp et al., 1999a). Such flaring events are typically associated with the ejection of a synchrotron emitting cloud from the central, X-ray emitting region (Corbel et al., 2000; Fender et al., 1999).

We suggest that the scattering of primary X-rays in ejected material may be responsible for the enhanced transition X-ray time lags in Cyg X-1: In the hard state, a stable, presumably partially collimated, radio emitting outflow (“jet”) exists, while the soft state shows no outflow (Brocksopp et al., 1999a). During the formation and (failed) destruction of the jet, when radio flaring is observed, outflows that are uncollimated and much larger than those of the hard state might be present. Assuming that the hard state lag spectrum is produced in the accretion disk (which still poses a problem for most models; Nowak et al., 1999b) and that the rather weak hard state jet does not significantly affect these intrinsic lags, the prolonged lags during the transitions could be produced in these large ejected outflows. Additional scattering might also be responsible for the reduced X-ray coherence that was reported by Cui, Zhang & Chen (1998) for the 1996 state transitions. Such a model wherein a fraction of the observed lags is created near the base of a radio emitting jet or wind has been previously suggested in analogy to blazar jet emission models (van Paradijs 1999, priv. comm., see also Fender et al., 1999). The state change following the flaring/ejection could then lead to a new accretion disk configuration with different X-ray spectral emission characteristics, different power spectra, but similar inherent lag spectrum.

## CHAPTER 5

---

### **Modeling PSDs of Cygnus X-1 & More**

In chapter 5 the *RXTE/PCA* pointings of the Cyg X-1 monitoring campaign up to 2001 November are analysed on the background of the *RXTE/ASM* lightcurves and the daily radio fluxes as measured by the Ryle telescope. This work concentrates on describing the variability properties of Cyg X-1 by modeling the power spectrum (PSD) of each pointing, on extending the Fourier-frequency dependent time lag studies already presented in chapter 4, and on the results of basic spectral modeling. Its goal is to characterize the accretion flow in the hard state. As in chapter 4, the overall self-contained structure of the associated publication (Pottschmidt et al., 2002) is adopted, as well as the “we-style” of that work.

The chapter is organized as follows: In section 5.1 the observations used, the data screening, the computation of the power spectra, and the procedure of fitting multiple Lorentzian profiles to the power spectra are described, as well as additional diagnostics that were applied. Then the results are presented, starting with the long term evolution of the power spectra and other observed parameters (section 5.2), followed by a detailed discussion of all observed flaring events/failed state transitions (section 5.3). Further discussions and conclusions can be found in the first three sections of chapter 6 (also based on Pottschmidt et al., 2002), starting with a summary of the new observational facts gained from the monitoring campaign (section 6.1). Since the method of Lorentzian decomposition has recently been successfully applied to the power spectra of several other neutron star and black hole binaries, our fit results are then compared to those findings (section 6.2). Finally, the accretion scenario based on the vertical expansion of the inner corona during transitions which has already been suggested in chapter 4 is motivated in more detail in section 6.3.

## 5.1 Observations and Data Analysis

### 5.1.1 The RXTE Monitoring Observations of Cygnus X-1

The *RXTE* data presented here were obtained with the Proportional Counter Array (*PCA*; Jahoda et al., 1996) and with the All Sky Monitor (*ASM*; Levine et al., 1996), using the pointed *RXTE* observation programs P30157 (1998), P40099 (1999), and P50110 (2000–2001). We used the standard *RXTE* data analysis software, *FTOOLS*, Version 5.0, to create lightcurves with a time resolution of  $2^{-6}$  s (P30157) or  $2^{-8}$  s (P40099, P50110) in multiple energy bands. The energy bands extracted for P30157 and P40099/P50110 present the closest match possible for the available data modes (see Table 5.1), and include the bands used in our analysis of the X-ray time lags (Pottschmidt et al., 2000, 2001). With a few exceptions noted below, the PSD analyses presented here were performed using summed lightcurves in the  $\sim 2$  keV to 13.1 keV energy range.

The P30157 data set (weekly monitoring in 1998 with a nominal exposure time of 3 ks per observation) is the same that was used previously for the study of the evolution of X-ray time lags (Pottschmidt et al., 2000, 2001) and the evolution of X-ray spectra (Smith, Heindl & Swank, 2002). The data set P40099 (biweekly monitoring in 1999 with a nominal exposure time of 10 ks per observation) presented here has also been included in the time lag study of Pottschmidt et al. (2001). The P50110 data (biweekly monitoring with a nominal exposure time of 20 ks per observation) have not been published before. Starting in 1999, simultaneous observations at radio wavelengths performed with the Ryle telescope in Cambridge, U.K., are also part of the campaign. In addition, daily radio fluxes were obtained with the Ryle telescope (Fig. 5.3g).

For all observations, high resolution lightcurves and X-ray spectra were generated using standard screening criteria: a pointing offset of  $< 0.^\circ 01$ , a SAA exclusion time of 30 minutes<sup>1</sup>, and a source-elevation of  $> 10^\circ$ . At times of low source luminosity, when the “electron ratio”, i.e., a measure for the particle background in the *PCA*, was not influenced by the source itself, we also imposed a maximum “electron ratio” of 0.1. Good-time intervals (GTIs) were then created for all available PCU combinations, and from those suitable GTIs were selected for extracting high time-resolution data for the data modes and energy bands given in Table 5.1. For each GTI file, we generated the background spectrum using the *FTOOL* `pcabackest` and the “sky-VLE” background model. The background in a given energy band was then taken into account in determining the PSD normalization.

As a result of the data screening,  $\sim 2$  ks of usable data were left for each of the P30157 observations and  $\sim 7$  ks for P40099 and P50110. Note that due to *RXTE*

<sup>1</sup>For a source as bright as Cyg X-1 this is a very conservative criterion.

Table 5.1: Energy bands and data modes used.

	PSD	lag/coherence	
		low	high
<hr/>			
PCA Epoch 3: data taken until 1999 March 22			
data mode B_16ms_46M_0_49_H			
channels	0–35	0–10	23–35
energy [keV]	~2–13.1	~2–4.1	8.4–13.1
<hr/>			
PCA Epoch 4: data taken after 1999 March 22			
data mode B_2ms_8B_0_35_Q			
channels	0–30	0–10	20–30
energy [keV]	~2–13.1	~2–4.6	8.4–13.1
<hr/>			

scheduling constraints the full nominal exposure time was only rarely reached. Observation dates and exposure times are included in Table A on pages 137 to 149 in the appendix.

### 5.1.2 Computation of the Power Spectra

The computation of the power spectra for all energy bands given in Table 5.1 follows Nowak et al. (1999a) and Nowak (2000).

For the P30157 data set, PSDs in the 0.002 to 32 Hz range were computed, while the P40099 and P50110 PSDs reach up to 128 Hz. This discrepancy arises from the different maximum time resolutions of the binned data modes that are available for these data sets (see Table 5.1). We decided to use the binned modes with their comparatively moderate time resolutions, because they allow us to study several different energy bands (see section 5.3) which cannot be done with the “single bit” data modes (250  $\mu$ s time resolution) that are also available.

All PSDs used in this chapter are presented in the normalization of Belloni & Hasinger (1990) and Miyamoto et al. (1992), where the PSD integrated over a certain frequency interval equals the square of the relative contribution of that frequency interval to the total rms noise of the source. Where possible, we adjusted the normalization to the background corrected count rate. The observational deadtime corrected Poisson noise was subtracted before the normalization. See Vikhlinin, Churazov & Gilfanov (1994) and Zhang et al. (1995) for a discussion of the deadtime influence on the PSD in general, Jernigan, Klein & Arons (2000) and Zhang et al. (1996) for the case of the *PCA* detector, and Revnivtsev, Gilfanov & Churazov (2000) for an application to *PCA* measurements of Cyg X-1 above 100 Hz. For most observations we used the first two components of Eq. (6) of Jernigan, Klein & Arons (2000), namely the approximation of the “general paralyzable deadtime influence” (Zhang

et al., 1995, Eq. (24)) plus the deadtime caused by “Very Large Events” (characterized by the PCA VLE count rate). For frequencies  $< 100$  Hz the correction of the noise level due to these two components amount to only a few percent. Higher order corrections or a fit of these components to the PSDs as applied by Jernigan, Klein & Arons (2000) or Revnivtsev, Gilfanov & Churazov (2000) are therefore not necessary here. We note that the discussed features in the PSDs have rms amplitudes well above the typical deadtime structures (see, e.g., Fig. 5 of Jernigan, Klein & Arons 2000 or Fig. 4 of Revnivtsev, Gilfanov & Churazov 2000).

A slightly different PSD normalization and deadtime correction has been applied to all observations performed after 2000 May 12, when the epoch of enhanced PCU 0 background count rates started. Here, a good background model was not yet available and thus we could not background correct the PSDs. This correction is only on the order of a few percent and does not influence appreciably our results (we note that this problem is, however, a serious problem for sources with a low count rate; Kalemci et al., 2001). Furthermore, as we do not have access to the VLE count rates from individual PCUs, it becomes impossible to correct the PSD for the VLE specific deadtime. Therefore, we only applied the general non-paralyzable deadtime correction.

For each observation we created three PSDs by averaging the individual PSDs from lightcurve segments with durations of 512 s, 128 s, and 32 s. Logarithmic frequency rebinning was performed on the same frequency grid for each of the three resulting PSDs. This grid ranges from  $2^{-9}$  to  $2^5$  (or  $2^7$ ) Hz ( $\sim 0.002$  to 32 [or 128] Hz), with different  $df/f$  values for different frequency ranges: 25 logarithmically spaced bins were used from 0.001 Hz–0.1 Hz, 50 bins from 0.1–20 Hz, and 5(15) bins from 20–32(128) Hz. The final PSD was then created by selecting for each grid bin the highest signal to noise value among the three PSDs.

### 5.1.3 Modeling the Power Spectra

As was shown by Nowak (2000), multiple Lorentzian profiles can provide a good description of the typical hard state variability of Cyg X-1 and GX 339–4 in the 0.001–100 Hz range. Inspired by this success, we applied multiple Lorentzian profiles to model the PSDs from our monitoring campaign and generally obtained good fits (see Table A and the typical examples displayed in Fig. 5.1 and Fig. 5.2). Note that power spectra obtained during the soft state, e.g., during the 1996 soft state, are not well fit with the multi-Lorentzian model (see also sections 5.3.4 and 5.3.5 below). Our fitting approach uses standard  $\chi^2$  minimization with the uncertainty of the free fit parameters determined using the usual prescription of Lampton, Margon & Bowyer (1976). Unless noted otherwise, we give the uncertainty in terms of  $1\sigma$  errors.

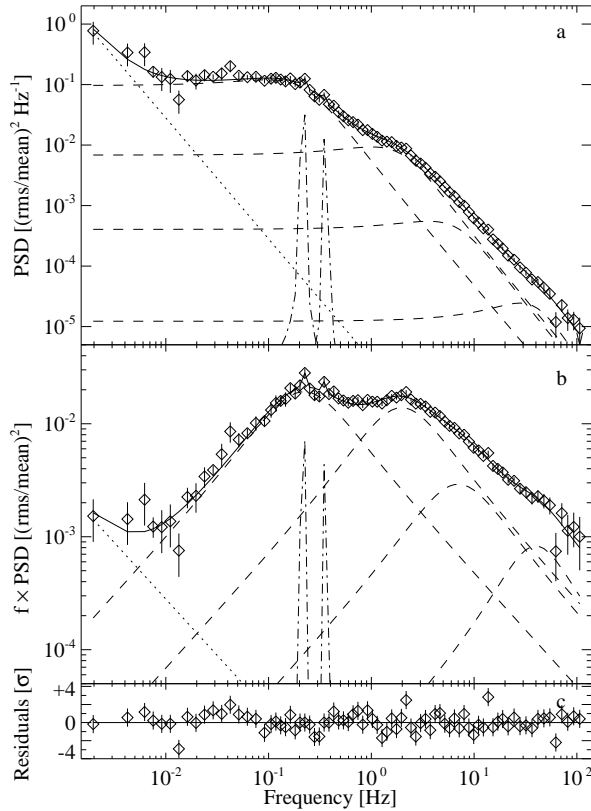


Figure 5.1: **a)** Best fit (solid line) to a typical 0.002–128 Hz hard state power spectrum of Cyg X-1 (P40099/18, 14off, 1999 September 13, diamonds) using multiple Lorentzians. The fit was performed for the energy range from  $\sim 2$  to 13.1 keV. It includes four broad (dashed lines) plus two narrow (dash-dotted lines) Lorentzian profiles and a power law component (dotted line). **b)** The same as above but here the PSD has been multiplied by frequency to illustrate the peak frequencies of the broad noise components (see section 4.3 for a discussion of the importance of these frequencies). **c)** Residuals between data and model in units of the standard deviation of the PSD data.

We describe the power spectra as the sum of Lorentzian profiles of the form:

$$L_i(f) = \pi^{-1} \frac{R_i^2 Q_i f_i}{f_i^2 + Q_i^2 (f - f_i)^2} \quad (5.1)$$

where  $f_i$  is the resonance frequency of the Lorentzian,  $Q_i \sim f_i / \Delta f_{i,\text{HWHM}}$  its quality

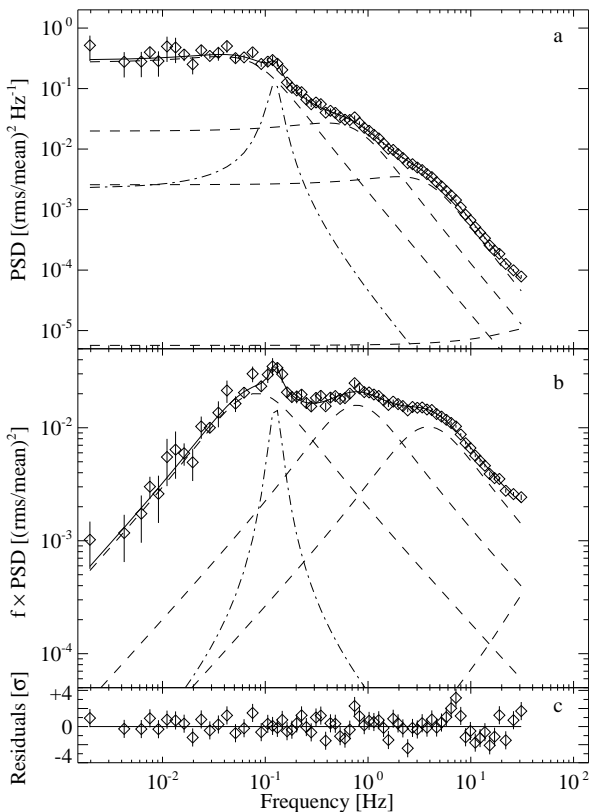


Figure 5.2: **a–c** Another typical fit, in this case to one of the P30157 observations (No. 11, 1998 February 20) in the 0.002–32 Hz frequency range. The best fit consists of four broad and one narrow Lorentzian profiles.

factor, and  $R_i$  its normalization constant. Integrating this profile over the frequency range from zero to infinity gives its total rms amplitude:

$$\text{rms}_i = R_i \left( \frac{1}{2} - \frac{\tan^{-1}(-Q_i)}{\pi} \right)^{1/2} \quad (5.2)$$

A further important quantity of the Lorentzian is its peak frequency, i.e., the frequency



where its contribution to the total rms variability is at its maximum:

$$v_i = f_i \left( \frac{1}{Q_i^2} + 1 \right)^{1/2} \quad (5.3)$$

As it was recently found that  $v_i$  seems to be the important parameter in terms of frequency correlations (Nowak, 2000; Nowak et al., 2001; van Straaten et al., 2002), we will use  $v_i$ , and not  $f_i$ , to describe the location of each Lorentzian, unless specifically noted otherwise.

Alternative models for the lowest frequency Lorentzian, such as using a zero centered Lorentzian, i.e., a shot noise component featuring a single relaxation time scale, may in principle provide fits of comparable quality (note that in the case of the observation analyzed by Nowak, 2000, a zero centered Lorentzian provided a significantly worse fit). The multi-Lorentzian fits, however, provide the most uniform description as well as the possibility to compare the noise components with those found in neutron star binaries (see section 4.3).

In almost all of our PSDs, four broad Lorentzians are apparent (Figs. 5.1 and 5.2) which we call  $L_1$ ,  $L_2$ ,  $L_3$ , and  $L_4$ . The fourth broad component,  $L_4$ , is usually present above 32 Hz and has also been noted by Revnivtsev, Gilfanov & Churazov (2000), Nowak (2000) and possibly in other sources by van Straaten et al. (2002). In the P30157 data set only its low frequency part can be seen. However, with the knowledge from the P40099 and P50110 data sets, we constrained its shape, especially its approximate width, and included this component in the P30157 models. We will discuss the issue of possible systematic errors resulting from this approach later.

We generally achieved a good fit using four broad Lorentzian components,  $L_1$ – $L_4$ , with typical peak frequencies of  $\sim 0.2$  Hz,  $\sim 2$  Hz,  $\sim 6$  Hz, and  $\sim 40$  Hz. As we will see below, these values vary considerably with time (compare, e.g., Fig. 5.1b and Fig. 5.2b). In our first modeling attempts we left the  $Q$ -factors of the Lorentzians as free parameters. They were found to vary considerably from observation to observation:  $Q_1$ ,  $Q_2$ , and  $Q_3$  ranged from  $\sim 0.05$ – $1.4$ ,  $Q_4$  was even less constrained. However, later experiments showed that fixing each  $Q$ -value to a representative value for each broad component does not significantly alter the fit results. This can be expected, since the broad components overlap over large frequency intervals (Figs. 5.1b and 5.2b). We therefore set  $Q_1 = 0.5$ ,  $Q_2 = 0.6$ ,  $Q_3 = 0.6$ , and  $Q_4 = 1.0$  for all fits. This resulted in a good description of most PSDs. There are only 22 cases out of the total 130 PSDs where the fit significantly improved when one or more of the  $Q$ -factors were treated as a free parameter. In these cases, which mainly coincided with the “failed state transitions” further discussed in section 5.3 below, we accepted the model with a variable  $Q$  as the best fit. For the low signal to noise *energy resolved* PSDs of the P30157 data we fixed  $Q_4$  and  $f_4$  to their best-fit value of the non energy resolved PSD.

In addition to  $L_1$  through  $L_4$ , a power law of the form

$$\text{PL}(f) = R_{\text{pl}} f^{-\alpha_{\text{pl}}} \quad (5.4)$$

is required in  $\sim 40\%$  of the observations. The majority of these power laws is required to reduce the residuals below  $\sim 0.01$  Hz. They have a typical slope of  $\sim 1.3$  and a normalization of  $\sim 10^{-4}$ . We note that the power law slope  $\alpha_{\text{pl}}$  cannot be well determined, since it is defined by only a few frequency bins. This results in an observed anti-correlation between  $\alpha_{\text{pl}}$  and the power law normalization  $R_{\text{pl}}$ , which we view as being largely systematic in nature. In some instances, however, the power law is the main contributor to the total rms amplitude. As we show below (section 5.3), these observations mainly coincide with “failed state transitions”. Generally, these observations are the same where we also had to leave the  $Q$ -values of the Lorentzians a free parameter. This can be expected as the contribution of the power law at higher frequencies slightly contaminates the other fit parameters.

In agreement with Nowak (2000), we often see additional subtle but statistically significant substructures. Sometimes these structures are sharp (Figs. 5.1 and 5.2) or weak and broad. In this case, further Lorentzian components ( $L_{\text{add},i}$ ) were added to the basic PSD continuum. We generally retained these components if their addition resulted in a significant improvement of the best fit  $\chi^2$ , or if they were very clearly present in the PSDs<sup>2</sup>. Residuals at frequencies slightly higher than the peak frequency of  $L_1$  tended to be narrow. We modeled these features with one or two narrow Lorentzians,  $L_{\text{add},1}$  and  $L_{\text{add},2}$  (see Fig. 5.1 and Fig. 5.2; typically both features are required, with the peak frequency of  $L_{\text{add},2}$  being slightly lower than  $\nu_2$ , while the peak frequency of  $L_{\text{add},1}$  is slightly above  $\nu_1$ ). Typical peak frequencies for these QPOs range from 0.1 to 0.6 Hz, and one might speculate about their relationship to the horizontal branch oscillation peaks in neutron star X-ray binaries (Wijnands & van der Klis, 1999, Table 4). In addition, below  $L_1$  a broad, weak ( $\lesssim 2\sigma$ ) residual at  $\sim 0.03$  Hz was often seen, which we designate  $L_{\text{add},3}$ . The total contribution of  $L_{\text{add},1}$ ,  $L_{\text{add},2}$ , and  $L_{\text{add},3}$  to the total rms is on the order of a few percent at most.

Using this modeling approach, we obtained values for the reduced  $\chi^2$  in the range of 1–2. The best-fit parameters of all 130 observations are given in electronic form in Table A. Most of the remaining systematic residuals in these fits are probably

<sup>2</sup>As mentioned in section 5.1.2, the PSDs are logarithmically rebinned to give a good description of the continuum power. This rebinning often had the result that the narrow features were confined to only one or two frequency bins. As a result, their modeling with a Lorentzian could not improve the  $\chi^2$ , although the feature is clearly present in the unbinned power spectrum. To be at least able to note the presence of such a feature, we nevertheless included them in the fit; however, only their frequency and power can be constrained, while their width, as represented by the  $Q$ -value, can only be described as ‘narrow’. These features will generally have  $Q \gtrsim 100$  in Table A. Because of these complications, we also do not give any formal uncertainty for the narrow Lorentzians in Table A.

due to the fact that the broad noise components have a more complex shape than a simple Lorentzian profile and/or that sub-harmonics are present. This is especially true for  $L_2$ , which is often associated with  $\lesssim 2\sigma$  residuals in the  $\sim 1\text{--}2\text{ Hz}$  range (see also Nowak, 2000). The broad low-frequency residual  $L_{\text{add},3}$  and other residuals at frequencies below  $\nu_1$  might also be due to this effect. A further source of weak systematic residuals might be our choice of  $Q$ -factors.

After obtaining the final best fit we computed the total rms variability amplitude relative to the mean count rate by summing the contributions of all power spectral fit components. The best fit Lorentzian profiles were integrated from zero to infinity (Eq. 5.2), while the power law contribution was obtained by integrating the power law over the frequency range from  $10^{-3}\text{ Hz}$  to  $200\text{ Hz}$ . Because of the different time resolution of the extracted light curves this approach is more systematic than the direct measurement of the rms variability from the X-ray data.

#### 5.1.4 Time Lags, Coherence, and Spectral Modeling

Although the emphasis of this paper is on the evolution of the short term timing properties of Cyg X-1 in terms of the PSD, it is obviously important to also characterize the source in terms of other quantities.

For black hole candidates, the X-ray light curves in two energy bands are similar to each other. However, the X-ray light curve in a higher energy band generally lags that measured in a lower energy band. This X-ray time lag depends on the Fourier frequency. A measure for the similarity of the X-ray light curves in these two bands is given by their coherence, which is again Fourier frequency dependent. We compute both quantities using the formulae given by Nowak et al. (1999a). As we have shown previously, an especially interesting quantity is the average X-ray time lag in the  $3.2\text{--}10\text{ Hz}$  band (Pottschmidt et al., 2000), which we will use to quantify the X-ray lag.

To obtain a description of the X-ray photon spectrum, we describe each source spectrum as the sum of a power-law spectrum with photon index  $\Gamma$  and a multi-temperature disk black body after Makishima et al. (1986), characterized by the temperature at the inner edge of the accretion disk,  $kT_{\text{in}}$ . To this continuum, a reflection spectrum after Magdziarz & Zdziarski (1995) is added. For this paper we concentrate on the X-ray spectrum below  $\sim 20\text{ keV}$  by ignoring the HEXTE data. Such an empirical model is sufficient to roughly describe the most important spectral parameters. A full study of the evolution of the broad-band X-ray spectrum that includes the HEXTE data and models the source spectrum in terms of the Comptonization models of Dove et al. (1997), Coppi (1999), and Poutanen & Svensson (1996) will be presented in a forthcoming paper (Gleissner et al., 2002).

Table 5.2: Average values and standard deviations of the rms amplitudes,  $\text{rms}_i$ , the peak frequencies,  $\nu_i$ , and the frequency ratios,  $\nu_i/\nu_j$ , for the four broad noise components ( $i, j = 1, \dots, 4$ ). The values are derived for different time episodes surrounding the 1998 May change and the 1998 July failed state transition. For the P30157 data the highest peak frequency,  $\nu_4$ , is biased (see text) and is therefore not quoted in this table.

	P30157 (1–18) <sup>a</sup> before	P30157 (19–28)	P30157 (29–32)	P30157 (33–52) post	P40099/P50110 <sup>b</sup> 1999–2001
	1998 April	1998 May/June	1998 July flare	1998 July	
$\text{rms}_{\text{tot}}$ [%]	36±1	32±3	28.2±0.2	29±1	29±2
$\text{rms}_1$ [%]	23±2	20±1	20±1	19±4	20±4
$\text{rms}_2$ [%]	20±1	20±1	19±1	18±1	18±1
$\text{rms}_3$ [%]	17±1	13±3	–	10±2	6±4
$\text{rms}_4$ [%]	4±1	4±3	7±1	3±2	5±1
$\nu_1$ [Hz]	0.08±0.02	0.16±0.07	0.45±0.07	0.25±0.06	0.33±0.12
$\nu_2$ [Hz]	0.6±0.1	1.1±0.5	3.5±0.5	1.7±0.4	2.6±0.9
$\nu_3$ [Hz]	3.6±0.3	5.2±1.3	–	6.4±1.0	8.4±2.0
$\nu_4$ [Hz]					41±8
$\nu_2/\nu_1$	7.3±1.1	7.0±0.7	7.7±0.7	7.0±0.5	7.8±1.3
$\nu_3/\nu_1$	44.0±6.4	35.6±8.4	–	27.7±4.5	30.0±5.3
$\nu_4/\nu_1$					141±65
$\nu_3/\nu_2$	6.0±0.9	5.1±1.2		4.0±0.7	3.9±0.6
$\nu_4/\nu_2$					18.2±7.2
$\nu_4/\nu_3$					5.1±1.4

<sup>a</sup> observation number within the P30157 data set

<sup>b</sup> the averages for P40099 and P50110 include several failed state transitions.

## 5.2 Evolution of the Power Spectrum

In this section we will discuss the overall behavior of the PSD of Cyg X-1 since 1998. The evolution of the best fit PSD parameters, the X-ray time lag, and the X-ray coherence function, as well as the photon index,  $\Gamma$ , from the spectral fits, the 15 GHz radio flux, and the *RXTE/ASM* count rate are shown in Fig. 5.3. Both the radio flux and the *ASM* count rate have been rebinned to a resolution corresponding to the orbital period of the HDE 226868/Cyg X-1 system ( $P_{\text{orb}} = 5.599829(16)$  d, see Brocksopp et al., 1999b; LaSala et al., 1998). This rebinning removes the effect of the well known orbital variation of the X-ray and radio flux (Pooley, Fender & Brocksopp, 1999; Brocksopp et al., 1999a; Wen, Cui & Bradt, 2001) such that long term changes become more apparent. Due to the rebinning, however, many short flares that are not due to the orbital modulation are smoothed out. We therefore present the

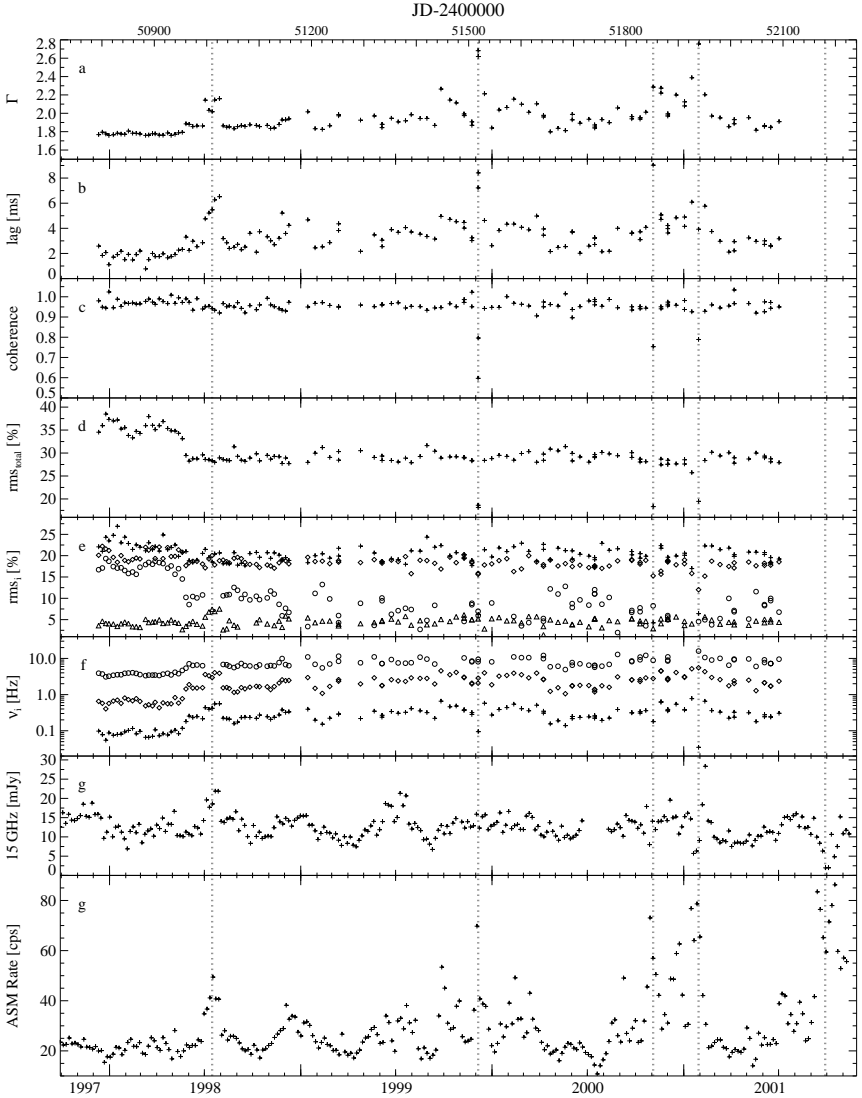


Figure 5.3: Spectral and timing parameters of Cyg X-1 from 1998–2001. The dotted vertical lines mark special observations discussed in section 5.3. The radio flux and the ASM rate have been rebinned to  $\sim 5.6$  d, the orbital period of Cyg X-1.

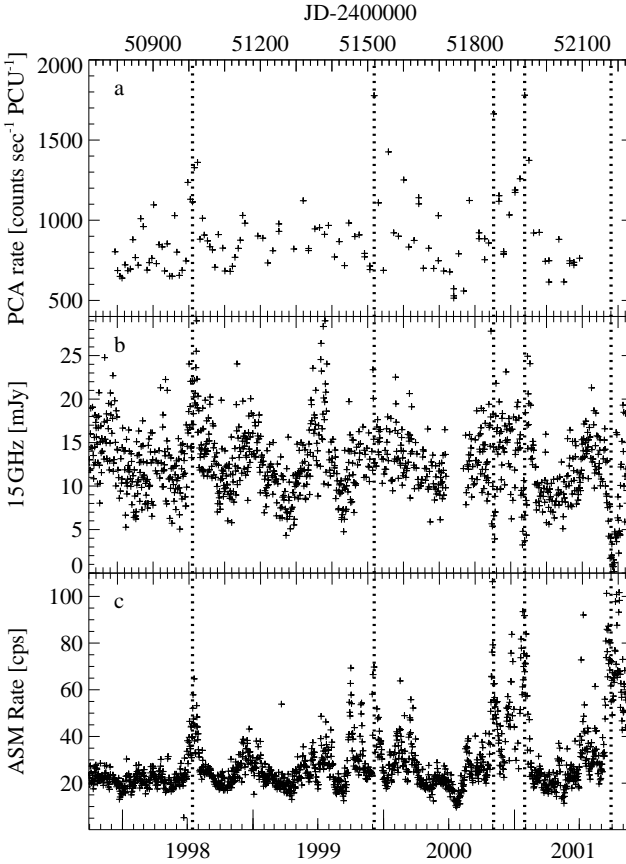


Figure 5.4: **a)** *RXTE*/*PCA* count rate (2.5–20 keV) for each pointing, as well as **b)** *RXTE*/*ASM* count rate and **c)** 15 GHz radio flux, both binned to a resolution of 1 d to show the variability on timescales that are smaller than the orbital timescale.

radio and *ASM* data again in Fig. 5.4 with a higher time resolution, together with the *RXTE*/*PCA* count rate determined from the monitoring observations. Not unexpectedly, the *ASM* and *PCA* rates are well correlated, although their correlation is not perfect due to their different energy bands and the X-ray spectral variability.

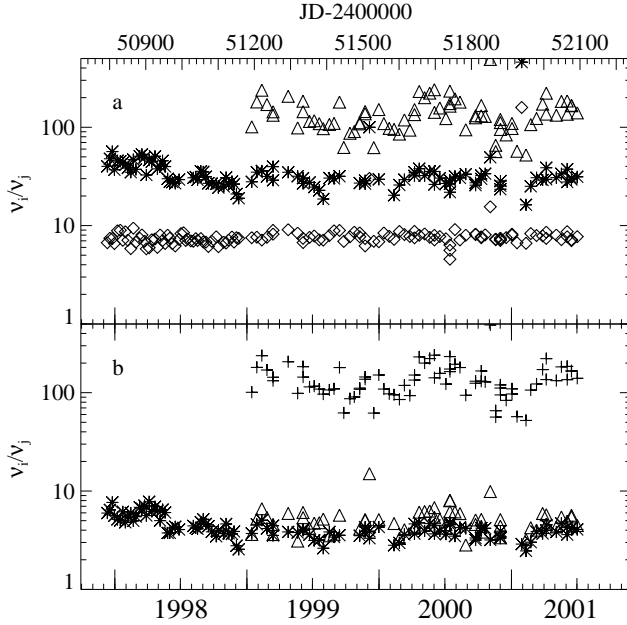


Figure 5.5: Constancy of the peak frequency ratios over the monitoring campaign. **a)** Diamonds:  $v_2/v_1$ , stars:  $v_3/v_1$ , triangles:  $v_4/v_1$ . **b)** Stars:  $v_3/v_2$ , triangles:  $v_4/v_2$ , crosses:  $v_4/v_3$ .

### 5.2.1 The Two Hard States

The most striking result of our fits is the bimodal behavior of the total rms amplitude (Fig. 5.3d): Starting in 1998 mid-April, the overall variability of Cyg X-1 on short timescales showed a decrease of  $\sim 7\%$ , from an average rms amplitude of  $36 \pm 1\%$  to  $29 \pm 1\%$ . At the same time, the power law index of the X-ray spectrum slightly softened from  $\sim 1.75$  to  $\sim 1.85$ , the characteristic frequencies of  $L_1$  through  $L_3$  shifted to higher values, and the X-ray time lag increased. Furthermore, a larger fraction of observations requires the power law component below  $\sim 0.01$  Hz. Apart from further “X-ray flares”, which we will describe in section 5.3, Cyg X-1 has remained in this softer and less variable (on short time-scales) X-ray state. Table 5.2 summarizes the main properties of the PSD before, during, and after the 1998 changes.

The parameters for the X-ray spectrum and timing behavior measured before 1998 May are very similar to the canonical hard state values for this source. Our campaign shows that these values have not been reached since then, i.e., *since 1998 May*,

*Cyg X-1* is exhibiting a behavior that is atypical compared to previously observed hard states of this source. In the following we describe these changes in further detail.

The change of the total rms can be mainly attributed to the behavior of  $L_3$  as seen in Fig. 5.3e: while the rms values of  $L_1$  and  $L_2$  stay roughly constant,  $L_3$  declines from its pre-May strength of  $\sim 17\%$  to  $10\pm 3\%$ , i.e., almost half of its original strength<sup>3</sup>. Especially during the X-ray flare in 1998 July,  $L_3$  cannot be detected at all. Since these events,  $L_3$  has mainly been present at a level between  $\sim 5\%$  and  $\sim 10\%$  rms, and was sometimes not detected at all. Typical examples for pre- and post-1998 May power spectra are shown in Figs. 5.2 and 5.1, respectively. These figures clearly show the decrease in strength of  $L_3$ , especially in the panels where the PSD has been multiplied with frequency.

In addition to this large change in strength, the whole PSD shifts to higher frequencies (Table 5.2). The two lowest peak frequencies,  $\nu_1$  and  $\nu_2$  increase by a factor of  $\sim 3$  during the change, while  $\nu_3$  increases by a factor of  $\sim 2$ . This behavior is not mirrored by the peak frequency of  $L_4$ . The sharp drop from about 60 Hz to 40 Hz at the end of P30157 in  $\nu_4$  is due to the biasing of its value caused by the low frequency cutoff of our data. We note that although the peak frequencies change, their ratios are remarkably constant over the whole campaign – in fact, the 1998 May event is only barely discernible in the evolution of the frequency ratios (Fig. 5.5).

The nature of the change in the hard state timing behavior can be clearly seen when the variations in the variability amplitudes and peak frequencies are considered together. Fig. 5.6 on page 105 shows the dependence of the normalization constant,  $R_i$ , of each broad component on the associated peak frequencies,  $\nu_i$ , for our data. Regions in Fig. 5.6 where the data point density is higher are due to the hard state behavior before and after 1998 April.

Several interesting features are apparent in Fig. 5.6. The three lowest frequencies,  $\nu_1$  through  $\nu_3$ , form a continuum from about  $5 \cdot 10^{-2}$  Hz to 20 Hz. For all three Lorentzians, the normalization of the Lorentzian correlates with its peak frequency – higher  $\nu_i$  also imply a lower normalization. Furthermore, in those frequency regions, where several Lorentzians can be found, e.g., around 0.5 Hz for  $\nu_1$  and  $\nu_2$ , and around 5 Hz for  $\nu_2$  and  $\nu_3$ , their normalizations seem to be the same. We stress that this is not due to a misidentification of the Lorentzians as these are always clearly distinguishable in the observations presented here. There are two distinct regions of the  $R_i$ - $\nu_i$  correlation: below  $\sim 3$  Hz, where the figure is dominated by  $L_1$  and  $L_2$ , and above 3 Hz, where  $L_3$  dominates. Clearly,  $\nu_3$  and  $R_3$  are much more strongly correlated than the parameters for the low frequency Lorentzians. We note that the sharpness of this

<sup>3</sup>Due to the high frequency cutoff of the P30157 data, the parameters of  $L_4$  are difficult to constrain during 1998. We found no indication for a bimodal behavior of this component, however, the large uncertainty of the fit parameters does not allow us to make any definitive statements.



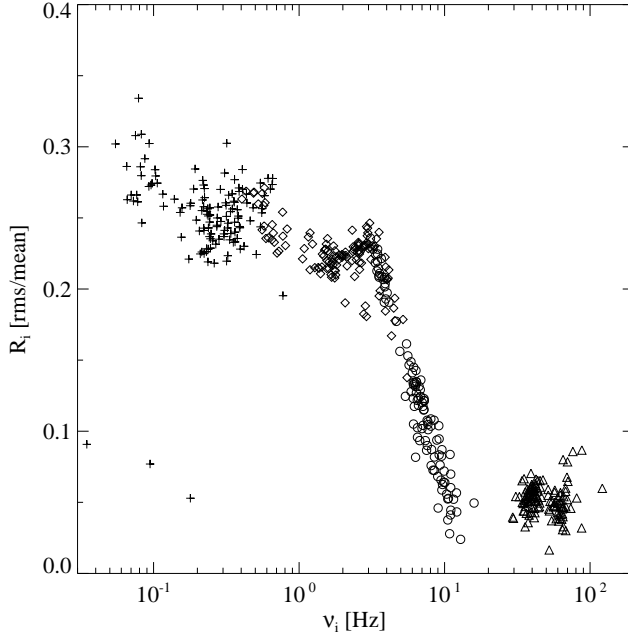


Figure 5.6: Normalization of the four broad noise components,  $R_i$ , versus their peak frequencies,  $v_i$ . The different plot symbols are attributed to the same components as in Fig. 5.3.

correlation might in principle have been influenced by the 32 Hz maximum frequency of our 1998 data set. However, the strong  $R_3$ - $v_3$  correlation is also present when only considering the P40099 and P50110 data. We speculate that these correlations are similar to the effect first seen by Belloni & Hasinger (1990) in terms of their broken power-law analysis of the PSDs of Cyg X-1, where the break frequency of the PSD is correlated with the total source rms variability. In our Lorentzian decomposition,  $v_1$  is roughly equivalent to the break frequency and shows a similar behavior. What is new, and not yet understood, however, is the behavior of  $L_3$ .

Finally, the highest peak frequency component,  $L_4$  (triangles), is clearly distinct from the lower frequency features and shows a different behavior. Its peak frequency and normalization are comparatively stable. The clustering of the data at 40 and 60 Hz again reflects the fact that  $v_4$  has been systematically over-estimated during P30157. During P40099 and later, however, no systematic changes are seen in  $v_4$ , although our data should have been sensitive to such changes.

We now discuss the properties of the Lorentzians in terms of other measured quantities (Fig. 5.7). The distinct behavior of the Lorentzians when plotted against the

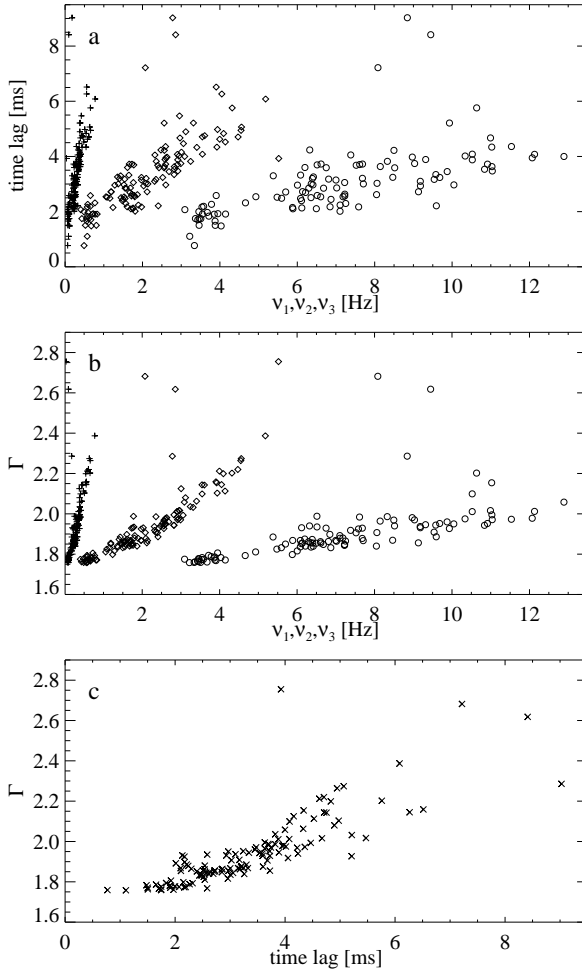


Figure 5.7: Correlations **a)** between the average time lag in the band between 2–4 keV and 8–13 keV and the peak frequencies  $\nu_1$ ,  $\nu_2$ , and  $\nu_3$  of the lower three Lorentzians, **b)** between the photon index,  $\Gamma$ , of the X-ray spectrum and  $\nu_1$  through  $\nu_3$ , and **c)** between  $\Gamma$  and the X-ray time lag. The symbols in panels a and b correspond to those used in Fig. 5.3.

X-ray photon spectral index,  $\Gamma$ , and the X-ray time lag gives us further confidence in the individual identifications of the Lorentzians. Both the X-ray time lag and the peak frequencies  $\nu_1$  through  $\nu_3$  are clearly correlated with  $\Gamma$ : softer photon spectra

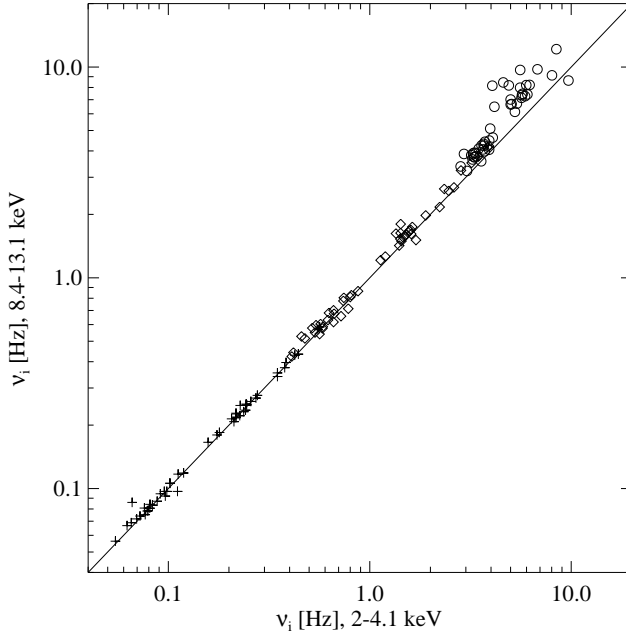


Figure 5.8: Peak frequencies of  $L_1$ ,  $L_2$ , and  $L_3$  as determined for the energy band from  $\sim 2$ –4.6 keV versus the peak frequency for the energy band from 8.4–13.1 keV. The symbols correspond to those used in Fig. 5.3.

imply a shift of the PSD towards higher frequencies and also higher X-ray time lags (Fig. 5.7b and c). There is a clear correlation between the average time lag and the Lorentzian peak frequencies (Fig. 5.7a). Although such a correlation between photon index and frequency has been noted with more limited data sets (di Matteo & Psaltis, 1999; Gilfanov, Churazov & Revnivtsev, 1999; Revnivtsev, Gilfanov & Churazov, 2000; Nowak et al., 2001), this is the first time that the simultaneous correlation with time lags has been found for Cyg X-1. A similar behavior has been seen in a more limited hard state data set of GX 339–4 (Nowak et al., 2001).

We note that there is no strong energy dependency of the power spectrum shape during the normal hard state phases. As an example, Fig. 5.8 shows the correlation between the peak frequency of  $L_1$ ,  $L_2$ , and  $L_3$  for the two energy bands for the 1998 data. To within their error bars, the peak frequencies of  $L_1$  and  $L_2$  are identical for these bands. The peak frequency of  $L_3$  is higher by about 30% in the hard energy band, a trend that continues when analyzing light curves in even harder energy bands.

### 5.3 Failed State Transitions and the 2001 October Soft State

In this section we study in detail the behavior of Cyg X-1 during the “flares” apparent in Fig. 5.3. During these events, the rms amplitude decreases, the strength of the power law contribution relative to the Lorentzians increases, and the X-ray spectrum softens. Generally, the X-ray time lag also shows values that are much higher than those seen before and after the flare, and the coherence function drops. PSDs measured during several of these events are shown in Fig. 5.9. These examples are significantly different from the “standard PSD shape” for the hard state as defined in Figs. 5.1 and 5.2.

We previously showed that measurements of the frequency dependent time lags between the  $\sim 2\text{--}4\text{ keV}$  and the  $\sim 8\text{--}13\text{ keV}$  lightcurves can provide further insight into the state of the source (Pottschmidt et al., 2000). Based on observations of the 1996 soft state transition, we found that during *transitional phases* between the soft and the hard state, the lag – averaged over the frequency band from 3.2 to 10 Hz – increases significantly. After the source fully enters the soft state, the time lag values drop to the the same level as observed in the hard state. We also found that during the *ASM* count rate flares of the 1998/1999 data, the X-ray lag increased as well. For the 1998 July event, for example, we measured a time lag of  $\sim 7$  ms in the above frequency band, which is higher than that during the normal hard state, but smaller than that during the transitions to and from the 1996 soft state ( $\sim 20$  ms). Because of these similarities with real state transitions from the hard state into the soft state and back, we called the *ASM* flares “failed state transitions” – during these events, the source changes its behavior compared to the normal hard state, but a full soft state is not reached, at least not on the sampling timescale of our *RXTE* monitoring. The continuation of the monitoring provides further examples for such “failed state transitions”: On 1999 December 05 and 2000 November 03, we measure a time lag of  $\sim 8$  ms and  $\sim 9$  ms, respectively (Fig. 5.3b), which is even higher than the measured 1998 July time lag, however, as we show below, the soft state was not reached during these times.

The availability of the different timing quantities for all monitoring observations allows us to connect changes of time lag with those in the power spectrum and the coherence function. As we already mentioned above, the changing behavior of the time lag is strongest in the 3.2–10 Hz band (Pottschmidt et al., 2000). The main contributions to the total rms variability in this frequency range are due to  $L_2$ , and to a lesser extent due to  $L_3$ . These two components are also the only broad noise components that are clearly present in the 1999 December 05 and 2000 November 03 power spectra (Fig. 5.9b and d). This seems also to be true for the transition to the soft state in 1996 (Fig. 2 of Pottschmidt et al. 2001; see also Belloni et al. 1996). Since the time lag behavior does not seem to reflect the transient behavior of the

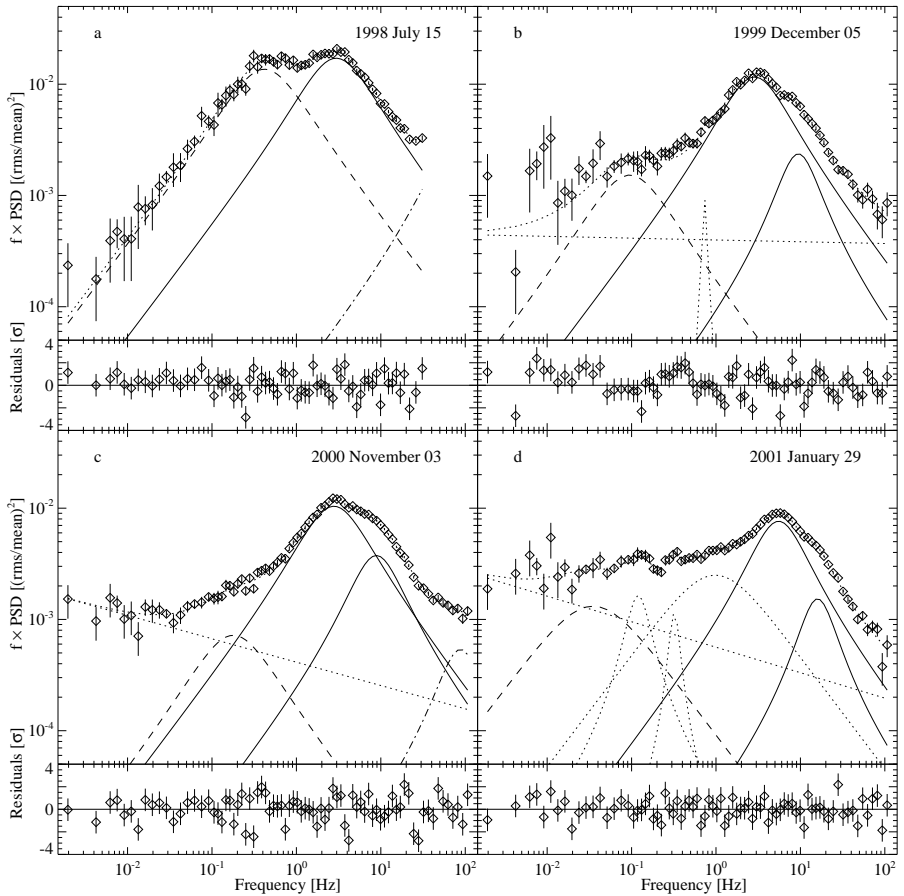


Figure 5.9: **a–d**) Examples of power spectra during failed state transitions that deviate significantly from the typical hard state shape as defined by Figs. 5.1 and 5.2. The best fit broad noise components are distinguished by their line styles: dashed:  $L_1$ , solid:  $L_2$  and  $L_3$ , dash-dotted:  $L_4$ . The remaining components and the total best fit are dotted. The observation dates are given in the plot, they are also marked by dotted lines in Figs. 5.3 and 5.4.

$L_3$  component, and since the frequency range showing the enhanced lags is more consistent with that of  $L_2$ , we tentatively identify the enhanced time lag during failed state transitions as being mainly due to  $L_2$ . Since the soft state itself shows neither

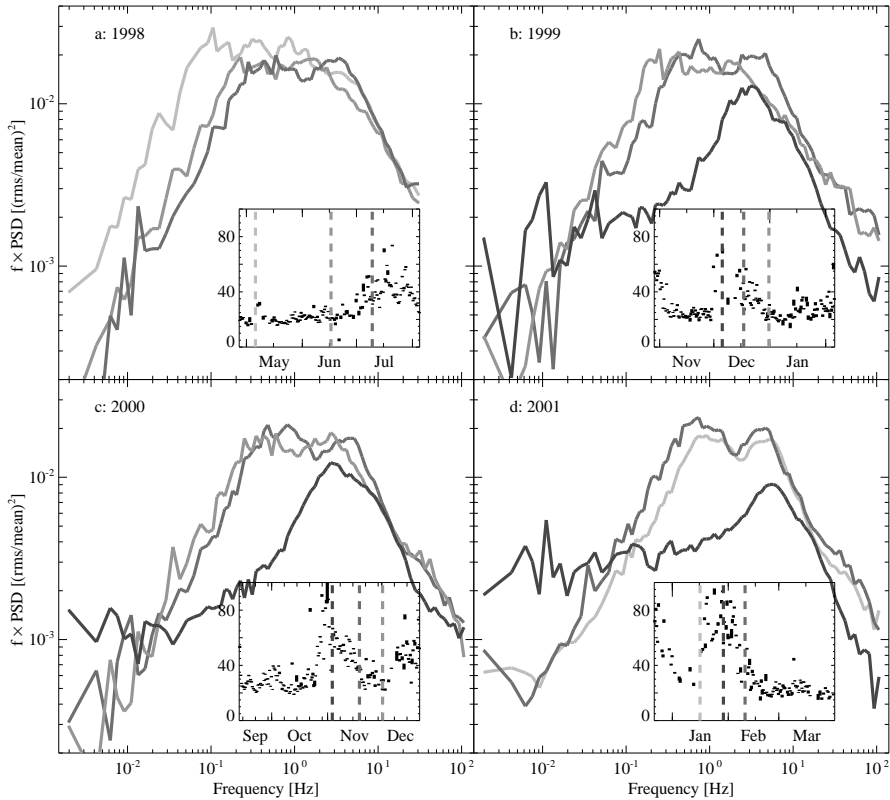


Figure 5.10: Evolution of the power spectra over the flaring events seen in the ASM lightcurve. Their location in the ASM lightcurve is indicated in the insets. The panels show the data from **a)** 1998 July, **b)** 1999 December, **c)** 2000 October/November, and **d)** 2001 January/February.

these broad noise components nor enhanced time lags, this identification provides a self-consistent picture.

Further information on the flares comes from inspecting the evolution of the PSD and the other timing quantities over the individual flares. In the following, therefore, we will describe these changes for each of the flares. For space reasons, we concentrate on the three clear “failed state transitions” that we mentioned above and that are indicated by the dashed lines in Figs. 5.3 and 5.4. Additional smaller deviations from the normal hard state behavior, including increased lags, were also seen in several

other observations, e.g., in 1999 September, in 2000 March, and in 2000 December. These events are associated with flaring episodes as well, however, our observations did not sample the change of the PSD, and we will not describe them further.

Finally, during two further events of our monitoring campaign, Cyg X-1 was seen to enter the soft state. This happened in 2001 October and possibly also in 2001 January. These events are also indicated with dashed lines in Figs. 5.3 and 5.4. The behavior before and after these soft states was similar to that during the “failed state transitions”, thus providing further evidence for the claim that the underlying physical mechanism of the “failed state transitions” is the same as that causing real transitions into the soft state. After describing the “failed state transitions” in more detail (sections 5.3.1 through 5.3.3), therefore, we will connect them with these soft states (sections 5.3.4 and 5.3.5).

### 5.3.1 1998 July

Over the course of the 1998 July flare, we identify five monitoring observations that appear to belong to the failed state transition in the sense that enhanced time lags are observed. In these five cases  $L_3$  is missing, while it is present again in the neighboring observations. The peak frequencies of  $L_1$  and  $L_2$  are significantly enhanced (Fig. 5.3f). An additional power law component has to be added only in the first of these five observations. An example PSD from this episode, and its best fit components, are shown in Fig. 5.9a.

The sequence of the evolution of the shape of the PSD as it enters into the flare (Fig. 5.10a) clearly shows the overall shift to higher frequencies and the vanishing of the third broad noise component. The transition back into the more usual hard state mirrors that of the transition into this flaring period. After 1998 July, however,  $L_3$  does not recover fully to its previously observed strength in the quiet hard state (see section 5.2).

The energy resolved analysis of the power spectra over the 1998 July event shows that there is some energy dependency of the rms variability amplitude. Before the event, the rms variability amplitude of  $L_3$  increased with photon energy that is, the PSD was flatter at higher energy bands as is typical for the hard state (Nowak et al., 1999a). During the flare, when the spectrum was soft, the rms variability amplitude decreased with energy. This is best illustrated in the behavior of  $L_1$ , where the total power in this component before the 1998 July event has a rather small energy dependence (Fig. 5.11, solid lines), while it is strongly energy dependent during the flare (Fig. 5.11, dashed lines).

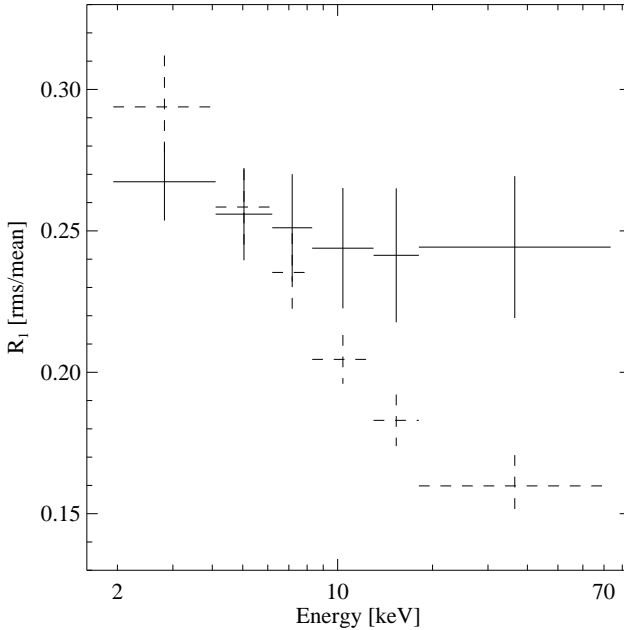


Figure 5.11: Change of normalization of  $L_1$  as a function of energy during the first half of 1998. Solid lines: Average of the normalization of  $L_1$ ,  $R_1$ , for observations P30157/19 through 28, *before* the 1998 July failed state transition. Dashed lines: Average of  $R_1$  for observations P30157/29 through 33, *during* the 1998 July event.

### 5.3.2 1999 December

The 1999 December PSDs (Fig. 5.10b) measured before and after 1999 December 05 are similar to the PSDs measured in 1998 July. The PSD measured on 1999 December 05, however, looks different: it exhibits a strong power law component, nearly lacks  $L_1$ ,  $L_2$  is strongly dominant, and the presence of  $L_3$  is clearly revealed, albeit at the weak levels typical of PSDs observed after 1998 May. At the same time the time lag is very high ( $\sim 8$  ms) and the X-ray coherence drops to 0.6. The inset of Fig. 5.10b shows that this PSD was observed near the maximum count rate of the flare. The subsequent monitoring observation during the decline of the outburst, however, shows a double-peaked profile that is very similar to that observed during the 1998 failed state transition, the X-ray lag decreases and the coherence is close to unity. This trend continues into the observation following the end of the outburst (Obs. 3 of Fig. 5.10b).

A similar PSD shape and X-ray spectral parameters to that of 1999 December 05 had been seen previously by Belloni et al. (1996), who hypothesized that they saw



Cyg X-1 in an “intermediate state” similar to those seen in GS 1124–68 (Nova Muscae 1991; Ebisawa et al., 1994; Miyamoto et al., 1994) and GX 339–4 (Méndez & van der Klis, 1997). In these objects, this “intermediate state” is typically seen during transitions between the soft and the hard state. Being near the peak of the ASM lightcurve, the 1999 December 05 observation therefore represents an evolutionary state further away from the hard state than the double-peaked PSDs discussed for the 1998 July flare. Such double peaked PSDs are only observed during the decline of the ASM lightcurve after the 1999 December 05 intermediate state observation.

### 5.3.3 2000 November

A similar sequence of PSD evolution to that described in section 5.3.2 was observed again in 2000 November (Fig. 5.10c). Here, the failed state transition of 2000 November 03 (Fig. 5.9c) shows an average time lag, coherence function, and power spectrum that are very similar to the lag, coherence, and PSD observed on 1999 December 05. The PSD is again dominated by  $L_2$  and  $L_3$  and shows a strong power law contribution. The remaining two Lorentzians,  $L_1$  and  $L_4$ , can also be detected. Fig. 5.12 shows the evolution of the PSD through the flare in terms of the Lorentzian decomposition, which mimics that of the 1999 December event (see also Figs. 5.10b and c): The 2000 November 03 observation was also made near the flux maximum of the outburst and has a PSD resembling the “intermediate state” of 1999 December 05, a quite large X-ray lag ( $\sim 8$  ms) and a decreased coherence, while the neighboring monitoring observations display the characteristic double-peaked PSD, a more normal lag of  $\sim 3$  ms, and the coherence function is back to  $\sim 1$ .

### 5.3.4 2001 October: A Short Soft State

The latest remarkable event of the monitoring campaign covered here was observed during 2001 September through November. As we will show here, this was the first time since 1996 that Cyg X-1 again exhibited a full soft state behavior in the X-rays and in the radio emission.

During 2001 September, the *RXTE*/*ASM* rate rose from its typical 20–30 cps to  $\sim 100$  cps, with precursor flares in July and August (Fig. 5.13). Reaching its peak in mid-September, the soft X-ray flux declined again and is now (2001 December), after some additional flaring in October, at a lower but still enhanced *ASM* level of approximately 60 cps. However, in contrast to previous flares, this time a clear reduction of the radio emission was also observed, with almost zero flux for about one week in the beginning of October (Fig. 5.13). After that time the radio emission slowly turned on again, although continued flaring in both the radio and the X-ray was observed. The combination of the strong *ASM* flux and the missing radio emission is typical for a soft state.

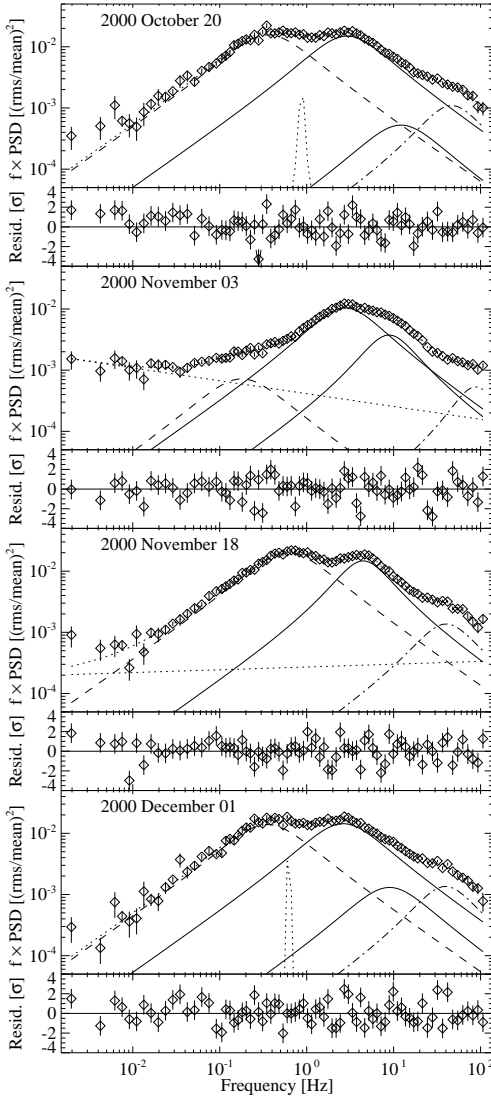


Figure 5.12: Evolution of the PSD during the monitoring observations of 2000 November. The style of the best fit components is the same as that in Fig. 5.9.

Further evidence for a soft state comes from the pointed *RXTE* observations performed in 2001 October. In Fig. 5.14 we show the PSDs and time lags for two of our monitoring observations, taken on 2001 October 20 and 2001 November 3 (see dashes in Fig. 5.13). We compare these data with typical data from failed state transi-

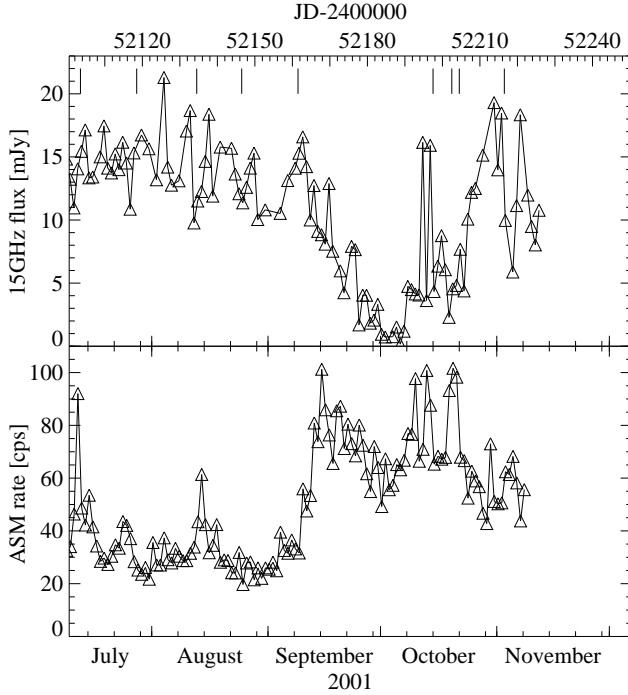


Figure 5.13: *RXTE*/*ASM* count rate and 15 GHz flux of Cyg X-1 during the fall of 2001. The dashes denote the time of pointed those *RXTE* observations that were part of our monitoring campaign.

tions as well as with data from the 1996 soft state and with typical hard state data. On 2001 October 20, the PSD had a clear  $f^{-1}$  shape, turning over at  $\sim 10$  Hz. The X-ray time lag was comparable with that measured during the standard hard state (Fig. 5.14) and the X-ray coherence was close to unity. The time lag behavior, the unity coherence, and the PSD shape are typical for the soft state (Cui et al., 1997; Pottschmidt et al., 2000). The X-ray spectrum of the 2001 October 20 *PCA* observation in the 3–20 keV range can be very well described by the empirical soft state spectrum of Cui et al. (1997), i.e., the sum of a black body and a broken power law. The broken power law has a photon index of  $\Gamma_1 = 2.78 \pm 0.03$  below, and  $\Gamma_2 = 2.10 \pm 0.02$  above the break energy of  $E_b = 11.1 \pm 0.1$  keV ( $\chi^2 = 27.5$  for 31 degrees of freedom, assuming an energy independent systematic uncertainty of 0.3%, a reasonable value for the current calibration of the *PCA*). The temperature of the black body is measured to  $kT_{\text{BB}} = 0.36 \pm 0.03$  keV, it contributes 20% to the total 2–10 keV flux of

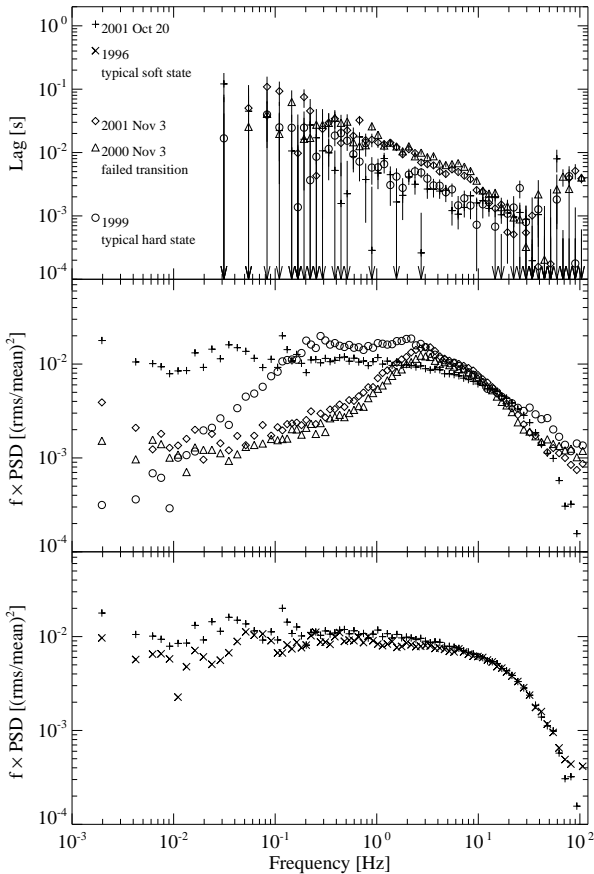


Figure 5.14: Time lags and PSD for the short soft state of 2001 Oct compared with other typical soft state, hard state, and failed state transition data.

$3.6 \times 10^{-8} \text{ erg cm}^{-2} \text{ s}$ . These spectral parameters are similar to those of the 1996 soft state (Cui et al., 1997), although the observed 2–10 keV flux is a factor  $\sim 2$  higher. We note that the 2001 October 20 data require an additional and very broad iron line at 6.4 keV (equivalent width  $\sim 440 \text{ eV}$  with a Gaussian width  $\sigma = 0.9 \pm 0.1 \text{ keV}$ ) that had not been seen in 1996.

On 2001 October 22, however, we see that the PSD slightly deviates from this soft state PSD. The X-ray spectrum is still well described by the empirical soft state model. During the next monitoring observation, on 2001 November 3, the PSD showed an “intermediate state” shape similar to that during the failed state transitions of 1999 November and 2000 December (section 5.3), with the  $L_1$  component missing and an increased power law component. Also pointing towards a transitional

behavior are the increased time lag and the reduced X-ray coherence. Both the PSD and the X-ray time lag are similar to the behavior measured on 2000 November 03, one year before the 2001 soft state (see Fig. 5.14). The X-ray spectrum is much harder and can be well described by the hard state spectral model.

We conclude that Cyg X-1 was transiting back into the hard state as of 2001 November and that the source spent only a short time, near the end of 2001 October, in a “classic” soft state. These observations clearly show that the change from the soft state to the transitional state can happen very quickly, within a few days at most. We note that nearly halfway between the October 20 soft state observation and the November 03 transitional state observation, a simultaneous *Chandra/RXTE* pointed observation was performed (PI: W. Cui). It will be interesting to see whether the *RXTE* data point more towards a soft state or a transitional state (although near zero radio flux states have been missed with all *Chandra* observations taken to date). Our observations here of the usual “failed state transition” behavior surrounding a clear though brief (in terms of radio and X-ray spectral properties, as well as X-ray variability properties) soft state lends further credence to our identification of the *ASM* flares seen since 1996 as being “failed state transitions”, as opposed to being brief “soft states”. (We note that our radio monitoring has been more frequent than our pointed X-ray observations, and this is the first clear indication of the soft state in both the radio and the X-rays since the radio monitoring began.)

### 5.3.5 2001 January: A Possible Soft State

We conclude this section with a discussion of another possible soft state which occurred in 2001 January. The evolution of the PSD shown in Fig. 5.10d displays again the vanishing of  $L_1$  and  $L_4$ , with an “intermediate state” PSD observed on 2001 January 29. From the point of view of our monitoring campaign, this behavior would have led us to classify this flare as yet another aborted state transition. In addition to our *RXTE* monitoring, however, further pointed *RXTE* observations were performed in early 2001, that had a much better sampling than our campaign. The analysis of these data by Cui, Feng & Ertmer (2002) shows PSDs that are similar to those seen here, with the exception of the data taken on 2001 January 28. Both the timing and spectral behavior are very similar to the 1996 soft state, leading Cui, Feng & Ertmer (2002) to claim a possible short soft state of Cyg X-1.

We note that in addition to the X-ray properties, the radio flux was also peculiar in 2001 January. During the end of 2001 January, the radio flux first dropped to about 30% of its typical value of  $\sim 15$  mJy, before a radio flare was seen (Figs. 5.3g and 5.4). In contrast to the 1996 and the 2001 November soft states, however, Cyg X-1 was always detected in the radio, indicating that the system had not settled into the soft state as it did in 1996 and 2001 November. In fact, our monitoring observation of 2001 January 29 shows again the transitional PSD. As in 2001 November, therefore,

the switch from the soft state (if it can truly be labeled a soft state) back into the intermediate state occurred within one day.

## CHAPTER 6

---

### Summary, Conclusions, and Outlook

#### 6.1 Summary

The rapid high energy variability of galactic black holes is still not understood. However, the behavior of the PSD and the time lags during our campaign gives some clue as to its origin.

The most important result of this thesis is that the shape of the PSD during the hard state and during the intermediate state can be productively interpreted with the decomposition of the PSD into the four broad Lorentzians and one power law. In contrast to earlier analyses, we were able to show that the decomposition holds for a very wide range of source parameters, even though the contributions of the power law and the Lorentzians are very different in the different states. *This result adds further weight to the claim that the Lorentzians are not just a convenient description of the PSD (merely more successful than the approximation of a broken power law), but that instead the Lorentzian components are the fundamental building blocks of the PSD of Cyg X-1, and thus possibly also of the PSDs of other black hole candidates.*

Furthermore, there are two fundamental results from our campaign on the long term variability of the source. The first result is that the change of the general long term behavior of Cyg X-1 from a “quiet hard state” to a “flaring hard state”, with frequent intermittent failed state transitions after 1998 May, coincided with a change in the PSD shape and amplitude. After 1998 May,  $L_3$  was clearly much weaker than before. At the same time, the whole PSD shifted towards higher frequencies in a way that preserved the ratio between the peak frequencies, a larger fraction of PSDs showed low frequency noise, the X-ray lag increased, and the average X-ray spectrum softened. The tendency for a softening of BHC spectra to correlate with a frequency shift of the main QPO features has also been seen in other sources (di Matteo & Psaltis, 1999; Gilfanov, Churazov & Revnivtsev, 1999; Revnivtsev, Gilfanov & Churazov, 2000; Kalemci et al., 2001; Nowak et al., 2001), and thus might be considered an intrinsic feature of *all* BHCs.

The second result of our campaign concerns the change in the PSD shape during the X-ray flares. We interpret these flares as transitions from the hard state via the intermediate state into the soft state. Most of these transitions “failed”, i.e., the transition stopped before the soft state was reached. That the “failed transitions” are caused by the same physical mechanism as the normal transitions into the soft state was shown by the two instances during the campaign where a brief soft state was observed (Sects. 5.3.4 and 5.3.5). In these cases, before the soft state was reached and after it was left again, the source behavior was indistinguishable from the behavior during the “failed transitions”.

On the way into the intermediate state,  $L_2$  and  $L_3$  almost remained constant, while  $L_1$  – and, to a lower significance, also  $L_4$  – became remarkably weaker. At the same time, the X-ray spectrum softened and the whole PSD shifted to higher frequencies. Furthermore, the X-ray time lag increases in the 3.2–10 Hz frequency band during the transitions and the coherence function decreases. *This is the frequency band where the PSD is dominated by the  $L_2$  and, to a lesser extent, the  $L_3$  components.* In those cases where the soft state was reached, the X-ray lag spectrum and the coherence function during the soft state were found to be very similar to that of the normal hard state, while the PSD, in contrast to the typical hard state, showed its characteristic  $f^{-1}$  shape with a cutoff at  $\sim 10$  Hz. During the soft state, no radio emission was detected. Such a detailed study of the hard state and transitions has to date only been possible for Cyg X-1. We note, however, that observations with a sparser coverage show similar behavior for GX 339–4 (Nowak et al., 2001) and for XTE J1650–50 (Kalemci et al., 2002).

## 6.2 Relationship between Neutron Star and Black Hole Frequencies

Apart from the analysis of Nowak (2000), Lorentzian modeling has also been used for describing the power spectra of neutron star sources. In an extensive analysis of data from 4U 0614+09 and 4U 1728–34, van Straaten et al. (2002) find that one to six Lorentzians are required to obtain a good description of the PSDs of these sources. A slight complication when comparing these results to ours is that van Straaten et al. (2002) use *zero frequency centered* Lorentzians, i.e., shot noise profiles, and not Lorentzians with non-zero center frequencies. As we describe in Sect. 5.1.3, our choice appears to result in a slightly lower  $\chi^2$ . Despite the different fit functions, however, the behavior of the maximum frequencies in both cases is still comparable. In terms of ascending  $\nu$ , van Straaten et al. (2002) call  $L_1$  and  $L_2$  the band-limited noise and zero-centered Lorentzian,  $L_3$  the low-frequency Lorentzian, and  $L_4$  the hectohertz Lorentzian. The “correct” identification of these components is difficult. For example,  $L_1$  and  $L_2$  are not present together in all data sets such that one might misin-



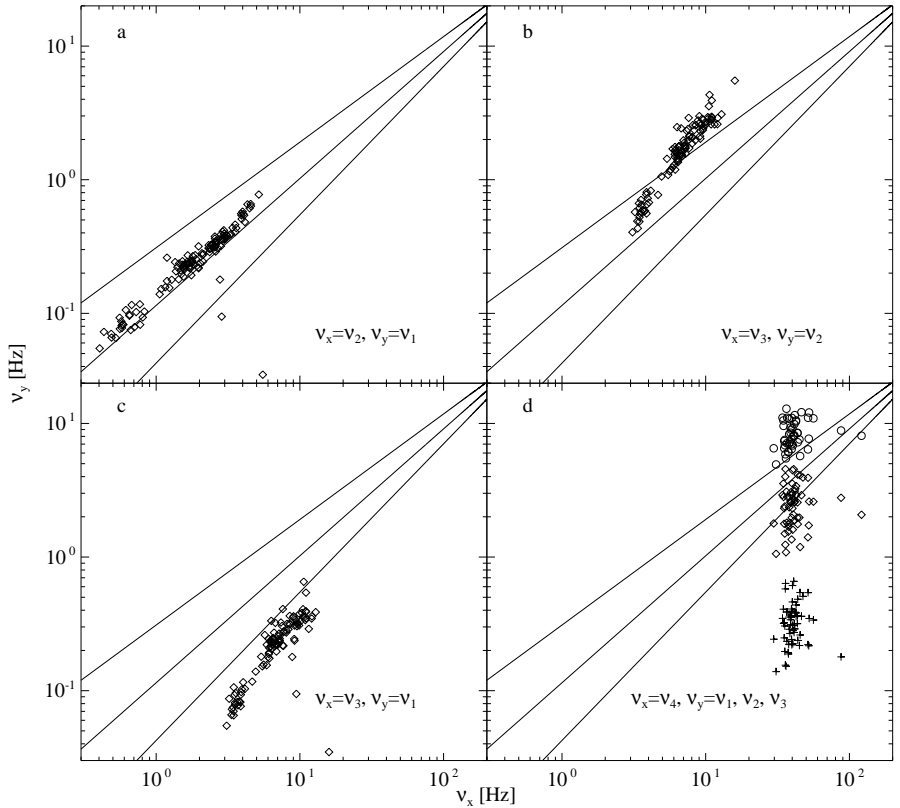


Figure 6.1: Correlations between the peak frequencies of the broad noise components,  $L_1$ – $L_4$  and the frequency correlations discussed by Psaltis, Belloni & van der Klis (1999, solid lines are  $\nu_y = 42\text{Hz}(\nu_x/500\text{Hz})^{0.95 \pm 0.16}$ ). **a**)  $\nu_1$  versus  $\nu_2$ , **b**)  $\nu_2$  versus  $\nu_3$ , **c**)  $\nu_1$  versus  $\nu_3$ . **d**)  $\nu_1$  (crosses),  $\nu_2$  (diamonds), and  $\nu_3$  (circles) versus the highest peak frequency,  $\nu_4$ . Only data taken in P40099 and P50110 are shown in panel d to avoid biasing due to the 32 Hz frequency cutoff in the P30157 data.

terpret the band limited noise as the zero-centered Lorentzian. Similar problems also apply for Cyg X-1: had the spacing of our observations during the (failed) state transitions been coarser, we would not have been able to correctly identify the Lorentzians during the state transitions.

At higher frequencies, additional Lorentzians are required to describe the kilohertz Lorentzians in neutron star sources, however, their connection to the PSDs of BHCs is

less clear. Nowak (2000) argue tentatively that  $L_4$  could be identified with the upper kilohertz QPO, however, the observed behavior of this component by van Straaten et al. (2002) casts some doubt on this interpretation.

There are two main correlations among frequency components that have been claimed for neutron star and black hole sources. Wijnands & van der Klis (1999) have pointed out a correlation between the PSD break frequency and the low frequency QPO of X-ray binaries. These two frequencies might be related to  $\nu_1$  and  $\nu_2$  in our classification scheme. Psaltis, Belloni & van der Klis (1999) have pointed out a correlation between the low frequency QPO and the lower frequency kHz QPO, i.e., frequencies that could be identified with  $\nu_2$  and  $\nu_3$  in our scheme. The latter correlation especially relies on identifying these features in multiple sources. The origin of these correlations is unknown.

In Fig. 6.1 we plot various combinations of one frequency versus another, and show that with the exception of  $\nu_4$  all frequency combinations show some sort of correlation (this is just a consequence of the constancy of the frequency ratios shown in Fig. 5.5). Given the above two cited correlations, the one that fits these data best is the correlation described by Psaltis, Belloni & van der Klis (1999), albeit applied to the  $\nu_1$  versus  $\nu_2$  correlation. We note, however, that in this particular range of frequencies, the  $\nu_1$  versus  $\nu_2$  correlation cited by Wijnands & van der Klis (1999) is numerically not very different than the  $\nu_2$ - $\nu_3$  correlation of Psaltis, Belloni & van der Klis (1999). Likewise, the  $\nu_2$ - $\nu_3$  data presented here are marginally consistent with the correlation discussed by Psaltis, Belloni & van der Klis (1999). Although the individual components discussed here span more than a decade in frequency, this is not large enough a range to identify unambiguously given features with the three decade wide correlations hypothesized and discussed by Psaltis, Belloni & van der Klis (1999). Still, correlations among the frequency components clearly do exist, and point to possible physical scenarios, as we further discuss below.

### 6.3 A Possible Physical Scenario

We now discuss the empirical evidence from our campaign in terms of more physical models for the accretion process in a black hole system. The hard state X-ray spectrum is thought to be caused, at least in part, by soft photons from the accretion disk which are Compton upscattered in a hot electron gas (Sunyaev & Trümper, 1979; Dove et al., 1998; Poutanen & Svensson, 1999, and references therein). In this picture, state transitions are caused by the disappearance of this Comptonizing medium. The cause for this disappearance is unknown, however, due to the luminosity difference between the hard and the soft state, many workers have assumed that the Compton corona is produced by some physical process which can work only at mass

accretion rates below a certain threshold rate such as the magnetorotational instability (Balbus & Hawley, 1991), advection (Esin, McClintock & Narayan, 1997), or some kind of coronal outflow (Merloni & Fabian, 2002; Blandford & Begelman, 1999, and references therein). A similar picture of changing coronal properties should also hold true within the hard state itself – although the Compton corona exists throughout the hard state, phases where a different X-ray spectrum and PSD are observed might well correspond to different coronal geometries (Nayakshin, Rappaport & Melia, 2000; Liu et al., 1999; Esin, McClintock & Narayan, 1997; Smith, Heindl & Swank, 2002, e.g.). Such a change in the coronal configuration could explain the reduction of the  $L_3$  component after 1998 May, as is also evidenced by an overall softening of the spectrum since that time.

We note that for Cyg X-1 the luminosity difference between the hard and soft state is rather small ( $\sim 35\%$ ; Zhang et al., 1997a). Furthermore, a power law component is always seen during the soft state. This suggests that the soft state in Cyg X-1 might not be a “normal” soft state as that seen in other black holes, but rather closer to the “very high state”. Furthermore, there are cases where the soft state has not a higher luminosity but a lower luminosity than the hard state. For GRS 1758–258, an intermediate state has even been observed at a higher luminosity than the hard state, while the soft state appears to be at a much lower luminosity (Smith et al., 2001). A possible explanation for these deviations from the canonical picture of the soft state having a much higher luminosity than the high state might be an hysteresis effect (Miyamoto et al., 1995), however, we note that regardless of the physical cause for deviations the observational evidence still points towards changes in the accretion disk geometry.

That the accretion disk geometry changed around 1998 May might also be the cause for the shift of the peak frequencies towards higher frequencies observed during that time. Even in prior analyses where PSDs of BHC have been described in terms of power law fits and “shot noise models” (Lochner, Swank & Szymkowiak, 1991, and references therein), it has been presumed that the characteristic frequencies can be attributed to time scales of the accretion disk. Churazov, Gilfanov & Revnivtsev (2001) have argued that PSD “breaks” are related to the size scale at which the accretion flow transits from a thin disk into a geometrically thin, hot inner corona. Di Matteo & Psaltis (1999) have argued that the dynamic range over which such a transition varies is somewhat limited since the observed frequencies themselves, although variable and correlated with spectral hardness, only span a limited range. Since flow frequencies scale as  $\delta v/v \sim (H/R)^2$  (e.g., di Matteo & Psaltis, 1999, and references therein), if the Lorentzians are associated with resonant effects within the accretion disk, they must originate from a region that is geometrically thicker than the thin accretion disk, i.e., a comparably extended region such as the accretion disk corona.

A simplified analysis of the characteristic frequencies of such a transition region

has been presented by Psaltis & Norman (2001). These authors note that if the outer disk acts as a “noise source”, the transition region acts as a “filter”, and the inner corona acts as a “response” which processes the filtered noise into observable X-ray variability, then one expects to observe a number of quasi-periodic features. These features would be related to radial, vertical, acoustic, rotational, etc., oscillations of the transition region. Many of these frequencies would be expected to scale as  $R_T^{-3/2}$ , where  $R_T$  is the transition region radius. More recently, Nowak et al. (2001) have shown that such a scaling might exist for hard state observations of GX 339–4. Specifically, they show that in “sphere and disk” coronal models, the “coronal compactness” – where higher compactness,  $\ell_c$ , means harder spectra – scales as  $\ell_c \sim R_T$ . Furthermore, the characteristic PSD frequencies, measured in a manner similar to that used to describe the Cyg X-1 PSDs presented here, scale as  $\ell_c^{-3/2}$ . Both Cyg X-1 and GX 339–4, in their hard states, show that spectral softening is correlated with higher PSD frequencies, although we have yet to characterize the Cyg X-1 spectra in terms of the coronal models presented by Nowak et al. (2001). Such an analysis is currently underway (Gleissner et al., 2002).

Further hints towards attributing at least some of the Lorentzians to the Compton corona come from the PSD behavior during the transitions into the intermediate or the soft state. We hypothesize that the variability causing  $L_1$  and possible  $L_4$  is also associated with the accretion disk corona, since these components – like the corona – appear to vanish during the transition. Since  $L_2$  and  $L_3$  remain present in the 3.2–10 Hz band, we are tempted to attribute the increased X-ray time lag in this frequency band to these components. As discussed by Nowak (2000), the overall measured time lag may in reality be a composite of time lags inherent to each individual PSD component. Whereas the composite time lag might be fairly small, the time lags associated with the individual PSD components might be somewhat larger (specifically, see Fig. 5 of Nowak, 2000). The fairly long intrinsic time lags of these individual PSD components would only be revealed in the absence of the other PSD components. Such a picture might explain the larger X-ray time lag during state transitions: Here, the  $L_2$  and  $L_3$  components, which sit in the 3.2–10 Hz band, contribute a larger *relative* fraction of the total source variability. If their intrinsic lag is larger, a larger lag would be observable during state transitions when the contribution of  $L_1$  and  $L_4$  is reduced. We note that such a picture of a “composite X-ray time lag” is somewhat suggested by the observational shape of the time lag spectrum, where “jumps” between different frequency bands of roughly constant time lag seem to correspond to the overlap regions of the broad Lorentzians (Nowak et al., 1999b; Poutanen, 2002; Pottschmidt et al., 2000).

While the origin of the time lag is not yet understood, it is possible that the time lag is somehow related to a characteristic length scale of the medium which produces the observed photons. If this is true, then the larger lags during state transitions may

be showing that some part of the source geometry changes and becomes larger during the transitions. It is important to note that although there is no radio emission during the soft state, there does seem to be a slight increase of the radio flux at least *during* some of successful transitions into and out of the soft state (Corbel et al., 2000; Zhang et al., 1997b). Furthermore, intermittent, rapid radio flaring activity also seems to be associated with the (failed) transitions (Pooley, priv. comm.).

In general, we see that the time lags are correlated with the PSD frequencies and correlated with the photon index,  $\Gamma$  (Fig. 5.7a in Sect. 5.2). For GX 339–4, spectral fits with the coronal model of Coppi (1999) – where a spherical corona with seed photons distributed throughout it according to the diffusion equation is modeled – suggest an *increasing* radius with a softening spectrum (Nowak et al., 2001), consistent with a geometric interpretation of increased time lags. Nowak et al. (2001) therefore argued for a jet-like model for the hard state of GX 339–4 where the radius of the *base* of the jet followed the radius-frequency correlations suggested by the “sphere and disk” coronal model (i.e., smaller *base* radius yielding softer spectra), while the *vertical* extent of the corona/jet followed the correlations suggested by the Coppi coronal model (i.e., more vertically extended coroneae yielding softer spectra). Thus, frequencies might be generated at the base of the jet, while time lags could be generated via propagation along the jet. Given the similar, but much more detailed, correlations observed here in Cyg X-1 it is tempting to ascribe the same type of model to these data. Whether the analogy to GX 339–4 holds in detail will depend upon the results of detailed coronal model fits (Gleissner et al., 2002).

Along these lines, based mainly on observations of microquasars, Fender (2001) and Fender et al. (1999) have recently attempted to unify the radio and X-ray observations into a geometrical picture of the region surrounding the central black hole. We have previously suggested that the enhanced X-ray lags during the “flares” observed in Cyg X-1 seem to add credibility to this picture (Pottschmidt et al., 2001). During the normal hard state, there is a weak outflow of material from the region surrounding the black hole. This outflow is responsible for producing the observed synchrotron radio emission. We think it likely that the base of this outflow coincides with the accretion disk “corona” that produces the hard state X-ray spectrum and is, given the results above, also responsible for part of the observed X-ray variability. During the “flares”, part of the corona gets ejected. Thus the mass of the radio outflow is temporarily enhanced, increasing the radio luminosity. As the corona is disturbed, whatever resonant mechanism producing the  $L_1$  and possibly also the  $L_4$  variability will be disturbed, resulting in a decrease of its contribution to the total rms variability. Furthermore, if this “corona” is “stretched” because of the ejection, it seems likely that a temporary increase in the X-ray lags should be associated with the outflow as the characteristic length scales increase. During the soft state, the corona has fully vanished such that no radio outflow is observed and the X-ray spectrum is soft. If  $L_2$

and  $L_3$  are produced at the corona-disk interface, they also vanish.

This very rough picture leaves many detailed questions open, such as the explanation for the strong domination of the  $f^{-1}$  power law during the soft state, its cutoff frequency, the generation of the intrinsic lag of the Lorentzians, or the physical mechanisms responsible for the PSD itself. However, we believe that monitoring campaigns such as this one, that are able to assess the long term, systematic changes in accreting systems, will continue to constrain the parameters of the observed physical systems and will enable us to switch from describing the “accretion disk weather” towards understanding the “accretion disk climate”. Equally importantly, X-ray astronomy is entering a phase of high spectral resolution observations with such instruments as *Chandra* and *XMM-Newton*. The nature of these instruments does not allow detailed and intensive monitoring campaigns such as this one. However, given the continued operation of the *RXTE/ASM* and judicious use of simultaneous pointed *RXTE* observations, campaigns such as this will allow these individual high resolution observations to be placed within their proper ‘global’ context.

## 6.4 Outlook

At least two main areas of research will still be explored in the next few years using the Cyg X-1 monitoring data: first it is obvious from what has been discussed in this chapter that detailed spectral modeling in the X-ray regime using physical accretion models can be expected to be very revealing. There are several codes available incorporating comparatively new physical ideas about accretion that have never before been evaluated using such a large sample of observations, e.g.: the code of Coppi (1992) which is also taking a non-thermal Comptonizing plasma component into account (section 2.2.3.5), the relativistic disk model of Gierliński, Maciolek-Niedzwiecki & Ebisawa (2001) to model the soft state (section 2.2.1.1), and the jet emission model of Markoff, Falcke & Fender (2001, section 2.2.5). All these ideas could be incorporated into the self-consistent accretion disk corona model that has been realized in form of a Monte Carlo code by Dove, Wilms & Begelman (1997) and their predecessors.

The second major area that has still to be investigated is a more detailed cross correlation analysis of the high time resolution X-ray and radio lightcurves. A preliminary analysis that I performed on the simultaneous data of 1999 revealed no obvious correlation on time scales of 20 s to 20 min. However, a more careful analysis also including the recent (failed) state transitions has yet to be done.

Apart from those scientific questions, a worthwhile endeavor would be to make the results of the temporal, spectral, cross-correlation, etc. analyses available for the scientific community on the web via a dedicated database.

All the tasks described so far have always been planned as possible parallel and follow-up projects of the timing analyses performed for this thesis. In this context Dipl. Phys. Thomas Gleissner has recently started to work on the Cyg X-1 monitoring data for his PhD thesis.

In addition, several other uses for the Cyg X-1 monitoring data can be thought of that promise interesting results:

- Searching for signatures of the long timescale modulation of  $\sim 150$  d in the pointed X-ray data and checking their consistency with precession models. While this had originally been a major objective of the campaign, the recent unstable source behavior shifted the focus to the failed state transitions instead. However, understanding the long timescales is still an issue, and for a start a possible procedure to separate the  $\sim 150$  d (precession) timescale from a  $\sim 200$  d flaring timescale has been developed by Sara Benlloch (priv. comm.).
- Recently, Uttley & McHardy (2001) discovered a strong, positive, linear correlation between the X-ray flux of XRBs and its standard deviation, on long (weeks–months) and short ( $< 1$  s) timescales. They observed this behavior in individual black hole and neutron star binary lightcurves as well as for AGN (on the corresponding longer time scales). Thus it seems to be a very basic feature of accretion. However, the underlying physics are still unknown. One model that can qualitatively produce such a correlation is the one of Kotov, Churazov & Gilfanov (2001) which is based on the work of Lyubarskii (1997). Meanwhile the existence of this correlation could be confirmed for all the hard state observations in the Cyg X-1 monitoring campaign (Gleissner et al., 2002). During state transitions it apparently loses its linearity (Gleissner et al., 2002). Performing a Fourier analysis on the temporal evolution of the standard deviation has the potential to constrain the radial extension of the innermost emission region (Uttley, priv. comm.).
- Also recently, a strong correlation has been found between the X-ray and optical high time-resolution lightcurves of the BHXRB XTE J1118+480 (Kanbach et al., 2001). This property of BHXRBs has never been studied and modeled before. In the light of the new results, simultaneous X-ray and optical monitoring of Cyg X-1 providing high time resolution should be aspired. This goal might involve an extension of the *RXTE* monitoring into the next AO(s).

I am sure that especially with the public availability of the analyses results on the web this list will grow. I hope that in the future many people will find the data and results from the Cyg X-1 monitoring campaign useful for their work and that maybe those data will eventually enable us to model the accretion disk climate around black holes.

## Bibliography

---

- Abramowicz, M., Björnsson, G., & Pringle, J., (eds.) 1998, *Theory of Black Hole Accretion Discs*, (Cambridge: Univ. Cambridge Press)
- Abramowicz, M. A., Björnsson, G., & Iguemshchev, I. V., 2000, *PASJ*, 52, 295
- Abramowicz, M. A., Lanza, A., & Percival, M. J., 1997, *ApJ*, 479, 179
- Agol, E., Krolik, J., Turner, N., & Stone, J., 2001, *ApJ*, 558, 543
- Böttcher, M., 2001, *ApJ*, 553, 960
- Bałucińska-Church, M., Church, M. J., Charles, P. A., Nagase, F., LaSala, L., & Barnard, R., 1997, *MNRAS*, 311, 861
- Balbus, S. A., & Hawley, J. F., 1991, *ApJ*, 376, 214
- Ball, G. H., Narayan, R., & Quataert, E., 2001, *ApJ*, 552, 221
- Ballantyne, D. R., Ross, R. R., & Fabian, A. C., 2001, *MNRAS*, 327, 10
- Belloni, T., 2001, in *X-ray Emission from Accretion onto Black Holes*, ed. T. Yaqoob, J. H. Krolik, published electronically at <http://www.pha.jhu.edu/groups/astro/workshop2001/>
- Belloni, T., et al., 1999, *ApJ*, 527, 345
- Belloni, T., & Hasinger, G., 1990, *A&A*, 227, L33
- Belloni, T., Klein-Wolt, M., Méndez, M., van der Klis, M., & van Paradijs, J., 2000, *A&A*, 355, 271
- Belloni, T., Méndez, M., King, A. R., van der Klis, M., & van Paradijs, J., 1998, in Scarsi et al. (1998), 330
- Belloni, T., Méndez, M., van der Klis, M., Hasinger, G., Lewin, W. H. G., & van Paradijs, J., 1996, *ApJ*, 472, L107
- Beloborodov, A. M., 1999, *ApJ*, 510, L123
- Beloborodov, A. M., 2000, in Poutanen & Svensson (1999), 295
- Bendat, J. S., & Piersol, A. G., 1986, *Random Data: Analysis and Measurement Procedures*, (New York: Wiley), 2<sup>nd</sup> edition
- Berger, M., & van der Klis, M., 1998, *A&A*, 340, 143
- Bisnovatyi-Kogan, G. S., 1999, in *Observational Evidence for the Black Holes in the Universe*, (Dordrecht: Kluwer), 1
- Bisnovatyi-Kogan, G. S., & Blinnikov, S. I., 1977, *A&A*, 59, 111
- Blandford, R. D., & Begelman, M. C., 1999, *MNRAS*, 303, L1
- Blandford, R. D., & Königl, A., 1979, *ApJ*, 232, 34
- Bolton, C. T., 1972, *Nature*, 235, 271
- Borozdin, K., Revnivtsev, M., Trudolyubov, S., Shrader, C., & Titarchuk, L., 1999, *ApJ*, 517, 367
- Böttcher, M., & Liang, E. P., 1999, *ApJ*, 511, L37
- Bowyer, S., Byram, E. T., Chubb, T. A., & Friedman, H., 1965, *Science*, 147, 394
- Boyd, P. T., Smale, A. P., Homan, J., Jonker, P. G., van der Klis, M., & Kuulkers, E., 2000, *ApJ*, 542, L127
- Braes, L. L. E., & Miley, G. K., 1971, *Nature*,



- 232, 246
- Brocksopp, C., Fender, R. P., Larianiov, V., Lyuty, V. M., Tarasov, A. E., Pooley, G. G., Paciesas, W. S., & Roche, P., 1999a, *MNRAS*, 309, 1063
- Brocksopp, C., Jonker, P. G., Fender, R. P., Groot, P. J., van der Klis, M., & Tingay, S. J., 2001, *MNRAS*, 323, 517
- Brocksopp, C., Tarasov, A. E., Lyuty, V. M., & Roche, P., 1999b, *A&A*, 343, 861
- Casares, J., & Charles, P. A., 1994, *MNRAS*, 271, L5
- Caunt, S. E., & Tagger, M., 2001, *A&A*, 367, 1095
- Chevalier, C., & Ilovaisky, S. A., 1998, *A&A*, 330, 201
- Churazov, E., Gilfanov, M., & Revnivtsev, M., 2001, *MNRAS*, 321, 759
- Colbert, E., & Ptak, A., 2002, *ApJ*, in press (astro-ph/0204002)
- Coppi, P. S., 1992, *MNRAS*, 258, 657
- Coppi, P. S., 1999, in Poutanen & Svensson (1999), 375
- Corbel, S., Fender, R. P., Tzioumis, A. K., Nowak, M., McIntyre, V., Durouchoux, P., & Sood, R., 2000, *A&A*, 359, 251
- Cowley, A. P., 1992, *ARA&A*, 30, 287
- Cowley, A. P., et al., 1991, *ApJ*, 381, 526
- Cowley, A. P., Schmidtke, P. C., Hutchings, J. B., & Crampton, D., 1994, *ApJ*, 429, 826
- Cui, W., 1999, in Poutanen & Svensson (1999), 102
- Cui, W., Feng, Y.-X., & Ertmer, M., 2002, *ApJ*, 564, L77
- Cui, W., Heindl, W. A., Rothschild, R. E., Zhang, S. N., Jahoda, K., & Focke, W., 1997, *ApJ*, 474, L57
- Cui, W., Zhang, S. N., & Chen, W., 1998, *ApJ*, 492, L53
- Cui, W., Zhang, S. N., & Chen, W., 2000, *ApJ*, 531, L45
- Cui, W., Zhang, S. N., Focke, W., & Swank, J. H., 1997, *ApJ*, 484, 383
- di Matteo, T., & Psaltis, D., 1999, *ApJ*, 526, L101
- Done, C., & Życki, P. T., 1999, *MNRAS*, 305, 457
- Done, C., & Nayakshin, S., 2001a, *ApJ*, 546, 419
- Done, C., & Nayakshin, S., 2001b, *MNRAS*, 328, 616
- Dove, J. B., 1997, *Ph.D. thesis*, University of Colorado, Boulder
- Dove, J. B., Wilms, J., & Begelman, M. C., 1997, *ApJ*, 487, 747
- Dove, J. B., Wilms, J., Maisack, M., & Begelman, M. C., 1997, *ApJ*, 487, 759
- Dove, J. B., Wilms, J., Nowak, M. A., Vaughan, B., & Begelman, M. C., 1998, *MNRAS*, 289, 729
- Dullemond, C. P., & Turolla, R., 1998, *ApJ*, 503, 361
- Ebisawa, K., et al., 1994, *PASJ*, 46, 375
- Eikenberry, S. S., Matthews, K., Morgan, E. H., Remillard, R. A., & Nelson, R. W., 1998, *ApJ*, 494, L61
- ESA, 1997, *The Hipparcos and Tycho Catalogues*, Vol. ESA SP-1200, (Noordwijk: ESA Publication Division)
- Esin, A. A., McClintock, J. E., Drake, J. J., Garcia, M. R., Haswell, C. A., Hynes, R. I., & Munro, M. P., 2001, *ApJ*, 555, 483
- Esin, A. A., McClintock, J. E., & Narayan, R., 1997, *ApJ*, 489, 865
- Esin, A. A., Narayan, R., Cui, W., Grove, J. E., & Zhang, S.-N., 1998, *ApJ*, 505, 854
- Falcke, H., Beckert, T., Markoff, S., Koerding, E., Bower, G. C., & Fender, R., 2001, in *Lighthouses of the Universe*, ed. R. Sunyaev, M. Gilfanov, E. Churazov, (Heidelberg: Springer)
- Fender, R., 2001, in *Relativistic flows in Astrophysics*, ed. A. W. Guthmann, M. Georganopoulos, K. Manolakou, A. Markowitz, (Heidelberg: Springer), in press (astro-ph/0109502)

- Fender, R., et al., 1999, *ApJ*, 519, L165
- Fender, R. P., 2001, *MNRAS*, 322, 31
- Fender, R. P., Garrington, S. T., McKay, D. J., Muxlow, T. W. B., Pooley, G. G., Spencer, R. E., Stirling, A. M., & Waltman, E. B., 1999, *MNRAS*, 304, 865
- Fender, R. P., & Kuulkers, E., 2001, *MNRAS*, 324, 923
- Filippenko, A. V., Leonard, D. C., Matheson, T., Li, W., Moran, E. C., & Riess, A. G., 1999, *PASP*, 111, 969
- Filippenko, A. V., Matheson, T., Leonard, D. C., Barth, A. J., & van Dyk, S. D., 1997, *PASP*, 109, 461
- Focke, W. B., 1998, *Ph.D. thesis*, University of Maryland, College Park, Md.
- Ford, E. C., van der Klis, M., Méndez, M., van Paradijs, J., & Kaaret, P., 1999, *ApJ*, 512, L31
- Frank, J., King, A., & Raine, D., 1992, *Accretion Power in Astrophysics*, (Cambridge: Univ. Cambridge Press), 2<sup>nd</sup> edition
- Friend, D. B., & Castor, J. I., 1982, *ApJ*, 261, 293
- Frontera, F., et al., 2001, *ApJ*, 561, 1006
- Galeev, A. A., Rosner, R., & Vaiana, G. S., 1979, *ApJ*, 229, 318
- Garcia, M. R., McClintock, J. E., Narayan, R., Callanan, P., Barret, D., & Murray, S. S., 2001, *ApJ*, 553, L47
- Gierliński, M., Maciolek-Niedzwiecki, A., & Ebisawa, K., 2001, *MNRAS*, 325, 1253
- Gierliński, M., Zdziarski, A. A., Done, C., Johnson, W. N., Ebisawa, K., Ueda, Y., Haardt, F., & Philips, B. F., 1997, *MNRAS*, 288, 958
- Gierliński, M., Zdziarski, A. A., Poutanen, J., Coppi, P. S., Ebisawa, K., & Johnson, W. N., 1999, *MNRAS*, 309, 496
- Gies, D. R., & Bolton, C. T., 1982, *ApJ*, 260, 240
- Gies, D. R., & Bolton, C. T., 1986a, *ApJ*, 304, 371
- Gies, D. R., & Bolton, C. T., 1986b, *ApJ*, 304, 389
- Gies, D. R., et al., 2002, *ApJ*, in press (astro-ph/0206253)
- Gilfanov, M., Churazov, E., & Revnivtsev, M., 1999, *A&A*, 352, 182
- Gilfanov, M., Churazov, E., & Revnivtsev, M., 1999, *A&A*, 252, 182
- Gleissner, T., Pottschmidt, K., Wilms, J., Nowak, M. A., Heindl, W. A., Smith, D. M., & Staubert, R., 2002, *A&A*, in preparation
- Greiner, J., Cuby, J. G., & McCaughrean, M. J., 2001, *Nature*, 414, 522
- Greiner, J., Morgan, E. H., & Remillard, R. A., 1996, *ApJ*, 473, L107
- Griffiths, R. E., & Seward, F. D., 1977, *MNRAS*, 180, 75
- Gu, W., & Lu, J., 2000, *ApJ*, 540, L33
- Haardt, F., Done, C., Matt, G., & Fabian, A. C., 1993, *ApJ*, 411, L95
- Haardt, F., & Maraschi, L., 1991, *ApJ*, 380, L51
- Haardt, F., & Maraschi, L., 1993, *ApJ*, 413, 507
- Harlaftis, E., Collier, S., Horne, K., & Filippenko, A. V., 1999, *A&A*, 341, 491
- Harlaftis, E. T., Horne, K., & Filippenko, A. V., 1996, *PASP*, 108, 762+
- Harmon, B. A., Deal, K. J., Paciesas, W. S., Zhang, S. N., Robinson, C. R., Gerard, E., Rodríguez, L. F., & Mirabel, I. F., 1997, *ApJ*, 477, L85
- Hawking, S. W., 1988, *A Brief History of Time*, (Toronto: Bantam)
- Hawking, S. W., & Ellis, G. F. R., 1973, *The Large Scale Structure of Space-Time*, (Cambridge: Univ. Cambridge Press)
- Hawley, J. F., 2001, *ApJ*, 554, 534
- Hawley, J. F., & Balbus, S. A., 1991, *ApJ*, 376, 223
- Hawley, J. F., Balbus, S. A., & Stone, J. M., 2001, *ApJ*, 554, L49

- Hawley, J. F., & Krolik, J. H., 2001, *ApJ*, 548, 348
- Heindl, W. A., & Smith, D. M., 2002, in *X-rays at Sharp Focus: Chandra Science Symposium*, ed. E. M. Schlegel, S. Vrtilik, (San Francisco: Astron. Soc. Pacific), in press (astro-ph/0107469)
- Herrero, A., Kudritzki, R. P., Gabler, R., Vilchez, J. M., & Gabler, A., 1995, *A&A*, 297, 556
- Hjellming, R. M., & Wade, C. M., 1971, *ApJ*, 168, L21
- Homan, J., Wijnands, R., van der Klis, M., Belloni, T., van Paradijs, J., Klein-Wolt, M., Fender, R., & Méndez, M., 2001, *ApJ*, 132, 377
- Hua, X.-M., & Titarchuk, L., 1995, *ApJ*, 449, 188
- Ichimaru, S., 1977, *ApJ*, 214, 840
- Igumenshchev, I. V., & Abramowicz, M. A., 2000, *ApJ*, 130, 463
- Igumenshchev, I. V., Abramowicz, M. A., & Narayan, R., 2000, *ApJ*, 537, L27
- Jahoda, K., Swank, J. H., Giles, A. B., Stark, M. J., Strohmayer, T., Zhang, W., & Morgan, E. H., 1996, in *EUUV, X-Ray, and Gamma-Ray Instrumentation for Astronomy VII*, ed. O. H. Siegmund, (Bellingham, WA: SPIE), 59
- Janiuk, A., Życki, P. T., & Czerny, B., 2000, *MNRAS*, 314, 364
- Jernigan, J. G., Klein, R. I., & Arons, J., 2000, *ApJ*, 530, 875
- Kalemci, E., et al., 2002, *ApJ*, in preparation
- Kalemci, E., Tomsick, J. A., Rothschild, R., Pottschmidt, K., & Kaaret, P., 2001, *ApJ*, 563, 239
- Kanbach, G., Straubmeier, C., Spruit, H. C., & Belloni, T., 2001, *Nature*, 414, 180
- Kawaguchi, T., Mineshige, S., Machida, M., Matsumoto, R., & Shibata, K., 2000, *PASJ*, 52, L1
- Kazanas, D., & Hua, X.-M., 1999, *ApJ*, 519, 750
- Kemp, J. C., 1983, *IAU Circ.* 3780
- Kemp, J. C., Karitskaya, E. A., Kumsiashvili, M. I., Lyuty, V. M., Khruzina, T. S., & Cherepashchuk, A. M., 1987, *Sov. Astron.*, 31, 170
- Kitamoto, S., Miyamoto, S., Tanaka, Y., Ohashi, T., Kondo, Y., Tawara, Y., & Nakagawa, M., 1984, *PASJ*, 36, 731
- Kley, W., & Li, D. N. C., 1993, *ApJ*, 397, 600
- Kong, A. K. H., McClintock, J. E., Garcia, M. R., Murray, S. S., & Barret, D., 2002, *ApJ*, 570, 277
- König, M., 1997, Dissertation, Eberhard-Karls-Universität Tübingen
- König, M., & Timmer, J., 1997, *A&AS*, 124, 589
- Kotov, O., Churazov, E., & Gilfanov, M., 2001, *MNRAS*, 327, 799
- Kubota, A., Mizuno, T., Makishima, K., Fukazawa, Y., Kotoku, J., Ohnishi, T., & Tashiro, M., 2001, *ApJ*, 547, L119
- Lampton, M., Margon, B., & Bowyer, S., 1976, *ApJ*, 208, 177
- Laplace, P. S., 1795, *Le Système du Monde*, Vol. II. Des Mouvements Réels des Corps Célestes, (Paris)
- Laplace, P. S., 1799, in *Allgemeine Geographische Ephemeriden*, Vol. 4(1), (Weimar), (engl. trans. in Hawking & Ellis (1973))
- LaSala, J., Charles, P. A., Smith, R. A. D., Bałucińska-Church, M., & Church, M. J., 1998, *MNRAS*, 301, 285
- Laurent, P., & Titarchuk, L., 1999, *ApJ*, 511, 289
- Laurent, P., & Titarchuk, L., 2001, *ApJ*, 562, L67
- Leahy, D. A., Darbro, W., Elsner, R. F., Weiskopf, M. C., Sutherland, P. G., Kahn, S., & Grindlay, J. E., 1983, *ApJ*, 266, 160
- Levine, A. M., Bradt, H., Cui, W., Jernigan, J. G., Morgan, E. H., Remillard, R., Shirey, R. E., & Smith, D. A., 1996, *ApJ*, L33–L36

- Li, H., Colgate, S. A., Wendroff, B., & Liska, R., 2001, *ApJ*, 551, 874
- Liang, E. P., & Nolan, P. L., 1984, *Space Sci. Rev.*, 38, 353
- Liang, E. P. T., & Price, R. H., 1977, *ApJ*, 218, 247
- Liu, B. F., Yuan, W., Meyer, F., Meyer-Hofmeister, E., & Xie, G. Z., 1999, *ApJ*, 527, L17
- Lochner, J. C., Swank, J. H., & Szymkowiak, A. E., 1991, *ApJ*, 376, 295
- Lutz, J. H., & Lutz, T. E., 1972, *AJ*, 77, 376
- Lyubarskii, Y. E., 1997, *MNRAS*, 292, 679
- Machida, M., Matsumoto, R., & Mineshige, S., 2001, *PASJ*, 53, L1
- Magdziarz, P., & Zdziarski, A. A., 1995, *MNRAS*, 273, 837
- Makishima, K., Maejima, Y., Mitsuda, K., Bradt, H. V., Remillard, R. A., Tuohy, I. R., Hoshi, R., & Nakagawa, M., 1986, *ApJ*, 308, 635
- Malzac, J., Beloborodov, A. M., & Poutanen, J., 2001, *MNRAS*, 326, 417
- Markoff, S., Falcke, H., & Fender, R., 2001, *A&A*, 372, L25
- McClintock, J. E., Garcia, M. R., Caldwell, N., Falco, E. E., Garnavich, P. M., & Zhao, P., 2001, *ApJ*, 551, L147
- McClintock, J. E., & Remillard, R. A., 1986, *ApJ*, 308, 110
- McConnell, M. L., et al., 2002, *ApJ*, 572, 984
- Meekings, J. F., Wood, K. S., Hedler, R. L., Byram, E. T., Yentis, D. J., Chubb, T. A., & Friedman, H., 1984, *ApJ*, 278, 288
- Méndez, M., & van der Klis, M., 1997, *ApJ*, 479, 926
- Menou, K., Esin, A. A., Narayan, R., Garcia, M. R., Lasota, J.-P., & McClintock, J. E., 1999, *ApJ*, 520, 276
- Merloni, A., & Fabian, A. C., 2002, *MNRAS*, 332, 165
- Merloni, A., Fabian, A. C., & Ross, R. R., 2000, *MNRAS*, 313, 193
- Meyer-Hofmeister, E., & Meyer, F., 2001, *A&A*, 380, 739
- Michell, J., 1784, *Phil. Trans. Roy. Soc. London*, 74, 35, (presented 27 November 1783)
- Miller, K. A., & Stone, J. M., 2000, *ApJ*, 534, 398
- Miller, M. C., Lamb, F. K., & Psaltis, D., 1998, *ApJ*, 508, 791
- Mirabel, I. F., Dahwan, V., Chaty, S., Rodríguez, L. F., Martí, J., Robinson, C. R., Swank, J., & Geballe, T. R., 1998, *A&A*, 330, L9
- Mirabel, I. F., Paul, J., Cordier, B., Morris, M., & Wink, J., 1991, *A&A*, 251, L43
- Mirabel, I. F., & Rodríguez, L. F., 1994, *Nature*, 371, 46
- Mirabel, I. F., & Rodríguez, L. F., 1998, *Nature*, 392, 673
- Mirabel, I. F., & Rodríguez, L. F., 1999, *ARA&A*, 37, 409
- Misra, R., 2000, *ApJ*, 529, L95
- Mitsuda, K., et al., 1984, *PASP*, 36, 741
- Miyamoto, S., & Kitamoto, S., 1989, *Nature*, 342, 773
- Miyamoto, S., Kitamoto, S., Hayashida, K., & Egoshi, W., 1995, *ApJ*, 442, L13
- Miyamoto, S., Kitamoto, S., Iga, S., Hayashida, K., & Terada, K., 1994, *ApJ*, 435, 398
- Miyamoto, S., Kitamoto, S., Iga, S., Negoro, H., & Terada, K., 1992, *ApJ*, 391, L21
- Miyamoto, S., Kitamoto, S., Mitsuda, K., & Dotani, T., 1988, *Nature*, 336, 450
- Molteni, D., Gerardi, G., & Valenza, M. A., 2001, *ApJ*, 551, L77
- Muno, M. P., Morgan, E. H., & Remillard, R. A., 1999, *ApJ*, 527, 321
- Muno, M. P., Remillard, R. A., Morgan, E. H., Waltman, E. B., Dhawan, V., Hjellming, R. M., & Pooley, G., 2001, *ApJ*, 556, 515
- Murdin, P., & Webster, B. L., 1971, *Nature*, 233, 110
- Narayan, R., Garcia, M. R., & McClintock,

- J. E., 2001, in Proc. IX Marcel Grossmann Meeting, ed. V. Gurzadyan, R. Jantzen, R. Ruffini, (Singapore: World Scientific), in press (astro-ph/0107387)
- Narayan, R., Mahadevan, R., Grindlay, J. E., Popham, R. G., & Gammie, C., 1998, *ApJ*, 492, 554
- Narayan, R., Mahadevan, R., & Quataert, E., 1998, in Abramowicz, Bjornsson & Pringle (1998), 148
- Narayan, R., & Yi, I., 1995, *ApJ*, 452, 710
- Nayakshin, S., & Dove, J. B., 2001, *ApJ*, 560, 885
- Nayakshin, S., Rappaport, S., & Melia, F., 2000, *ApJ*, 535, 798
- Ninkov, Z., Walker, G. A. H., & Yang, S., 1987a, *ApJ*, 321, 438
- Ninkov, Z., Walker, G. A. H., & Yang, S., 1987b, *ApJ*, 321, 425
- Nolan, P. L., et al., 1981, *ApJ*, 246, 494
- Novikov, I. D., 1995, *Black Holes and the Universe*, (Cambridge: Univ. Cambridge Press)
- Nowak, M. A., 1995, *PASP*, 107, 1207
- Nowak, M. A., 2000, *MNRAS*, 318, 361
- Nowak, M. A., Dove, J. B., Vaughan, B. A., Wilms, J., & Begelman, M. C., 1998, in Scarsi et al. (1998), 302
- Nowak, M. A., & Lehr, D. E., 1998, in Abramowicz, Bjornsson & Pringle (1998), 233
- Nowak, M. A., & Vaughan, B. A., 1996, *MNRAS*, 280, 227
- Nowak, M. A., Vaughan, B. A., Wilms, J., Dove, J. B., & Begelman, M. C., 1999a, *ApJ*, 510, 874
- Nowak, M. A., Wagoner, R. V., Begelman, M. C., & Lehr, D. E., 1997, *ApJ*, 477, L91
- Nowak, M. A., Wilms, J., & Dove, J. B., 2002, *MNRAS*, 332, 856
- Nowak, M. A., Wilms, J., Heindl, W. A., Pottschmidt, K., Dove, J. B., & Begelman, M. C., 2001, *MNRAS*, 320, 316
- Nowak, M. A., Wilms, J., Vaughan, B. A., Dove, J. B., & Begelman, M. C., 1999b, *ApJ*, 515, 726
- Oda, M., 1977, *Space Sci. Rev.*, 20, 757
- Ogilvie, G. I., 1999, *MNRAS*, 306, L9
- Orosz, J. A., Bailyn, C. D., McClintock, J. E., & Remillard, R. A., 1996, *ApJ*, 468, 380+
- Orosz, J. A., et al., 2002, *ApJ*, 568, 845
- Orosz, J. A., Jain, R. K., Bailyn, C. D., McClintock, J. E., & Remillard, R. A., 1998, *ApJ*, 499, 375+
- Orosz, J. A., et al., 2001, *ApJ*, 555, 489
- Papoulis, A. P., 1991, *Probability, Random Variables and Stochastic Processes*, (New York: McGraw-Hill), 3<sup>rd</sup> edition
- Park, M., & Ostriker, J. P., 2001, *ApJ*, 549, 100
- Peitz, J., & Appl, S., 1997, *MNRAS*, 286, 681
- Piran, T., 1978, *ApJ*, 221, 652
- Pooley, G. G., Fender, R. P., & Brocksopp, C., 1999, *MNRAS*, 302, L1
- Pottschmidt, K., 1997, *Diplomarbeit, Eberhard-Karls-Universität Tübingen*
- Pottschmidt, K., Wilms, J., Nowak, M. A., Heindl, W. A., Smith, D. M., & Staubert, R., 2000, *A&A*, 357, L17
- Pottschmidt, K., et al., 2002, *A&A*, submitted (astro-ph/0202258)
- Pottschmidt, K., Wilms, J., Staubert, R., Nowak, M. A., Heindl, W. A., & Smith, D. M., 2001, *Adv. Space Res.*, 28, 493
- Poutanen, J., 1998, in Abramowicz, Bjornsson & Pringle (1998), 100
- Poutanen, J., 2002, *MNRAS*, 332, 257
- Poutanen, J., & Fabian, A. C., 1999, *MNRAS*, 306, L31
- Poutanen, J., Krolik, J. H., & Ryde, F., 1997, *MNRAS*, 292, L21
- Poutanen, J., & Svensson, R., 1996, *ApJ*, 470, 249
- Poutanen, J., & Svensson, R., (eds.) 1999, *High Energy Processes in Accreting Black Holes*, ASP Conf. Ser. 161, (San Francisco:

- Astron. Soc. Pacifi c)  
 Press, W. H., 1978, *Comments Astrophys.*, 7, 103
- Prestwich, A., Kaaret, P., Zezas, A., Fabbiano, P., Lira, P., & Ward, M., 2001, *Chandra News*, 8, 1
- Priedhorsky, W. C., Terrell, J., & Holt, S. S., 1983, *ApJ*, 270, 233
- Pringle, J. E., 1976, *MNRAS*, 177, 65
- Psaltis, D., 2001, *ApJ*, 555, 786
- Psaltis, D., Belloni, T., & van der Klis, M., 1999, *ApJ*, 520, 262
- Psaltis, D., & Norman, C., 2001, *ApJ*, submitted (astro-ph/0001391)
- Quataert, E., 1998, *ApJ*, 500, 978
- Różańska, A., & Czerny, B., 2000, *A&A*, 360, 1170
- Reig, P., Belloni, T., van der Klis, M., Méndez, M., Kylafis, N. D., & Ford, E. C., 2000, *ApJ*, 541, 883
- Remillard, R. A., 2001, in *Evolution of Binary and Multiple Stars*, ed. P. Podsiadlowski, S. Rappaport, A. King, F. D'Antona, L. Burderi, (San Francisco: Astron. Soc. Pacifi c), 503
- Remillard, R. A., Morgan, E. H., McClintock, J. E., Bailyn, C. D., Orosz, J. A., & Greiner, J., 1997, in *Proc. 18th Texas Symposium*, ed. A. Olinto, J. Frieman, D. Schramm, (World Scientific Press), 750
- Revnitsev, M., Gilfanov, M., & Churazov, E., 2000, *A&A*, 363, 1013
- Revnitsev, M. G., Trudolyubov, S. P., & Borozdin, K. N., 2000, *MNRAS*, 312, 151, Erratum: *MNRAS* 315, 655
- Ross, R. R., Fabian, A. C., & Young, A. J., 1999, *MNRAS*, 306, 461
- Rothschild, R. E., et al., 1998, *ApJ*, 496, 538
- Rybicki, G. B., & Lightman, A. P., 1979, *Radiative Processes in Astrophysics*, (New York: Wiley)
- Scargle, J. D., 1982, *ApJ*, 263, 835
- Scargle, J. D., 1989, *ApJ*, 343, 874
- Scarsi, L., Bradt, H., Giommi, P., & Fiore, F., (eds.) 1998, *The Active X-ray Sky: Results from BeppoSAX and Rossi-XTE*, Nuclear Physics B Proc. Supp., Elsevier Science)
- Schlittgen, R., & Streitberg, B. H. J., 1995, *Zeitreihenanalyse*, (München, Wien: R. Oldenbourg), 6<sup>th</sup> edition
- Schmutz, W., Geballe, T. R., & Schild, H., 1996, *A&A*, 311, L25
- Schwarzschild, K., 1916, *Sitzber. Dtsch. Akad. Wiss. Berlin, Math. Phys. Tech. Kl.*, 189
- Shahbaz, T., van der Hooft, F., Casares, J., Charles, P. A., & van Paradijs, J., 1999, *MNRAS*, 306, 89
- Shakura, N. I., 1972, *AZh*, 49, 921, (1973, *Sov. Astr.* 16,756)
- Shakura, N. I., & Sunyaev, R. A., 1973, *A&A*, 24, 337
- Shapiro, S. L., Lightman, A. P., & Eardley, D. M., 1976, *ApJ*, 204, 187
- Shapiro, S. L., & Teukolsky, S. A., 1983, *Black Holes, White Dwarfs, and Neutron Stars*, (New York: Wiley)
- Shields, G. A., McKee, C. F., Lin, D. N., & Begelman, M. C., 1986, *ApJ*, 306, 90
- Shrader, C., & Titarchuk, L., 1998, *ApJ*, 499, L31
- Smith, D. M., Heindl, W. A., Markwardt, C. B., & Swank, J. H., 2001, *ApJ*, 554, L41
- Smith, D. M., Heindl, W. A., Swank, J., Leventhal, M., Mirabel, I. F., & Rodriguez, L. F., 1997, *ApJ*, 489, L51
- Smith, D. M., Heindl, W. A., & Swank, J. H., 2002, *ApJ*, 569, 362
- Soria, R., Wu, K., Page, M. J., & Sakelliou, I., 2001, *A&A*, 365, L273
- Spruit, H. C., 2001, in *The neutron star – black hole connection*, ed. C. Kouveliotou, J. Ventura, E. van den Heuvel, (Dordrecht: Kluwer), (astro-ph/0003144)
- Stella, L., & Vietri, M., 1998, *ApJ*, 492, L59
- Stern, B. E., Begelman, M. C., Sikora, M., &

- Svensson, R., 1995a, MNRAS, 272, 291
- Stern, B. E., Poutanen, J., Svensson, R., Sikora, M., & Begelman, M. C., 1995b, ApJ, 449, L13
- Stirling, A., de la Force, C., Spencer, R., Garrett, M., Fender, R., & Ogle, R., 2001, MNRAS, 327, 1273
- Strohmayer, T. E., 2001a, ApJ, 552, L49
- Strohmayer, T. E., 2001b, ApJ, 554, L169
- Sunyaev, R., & Revnivtsev, M., 2000, A&A, 358, 617
- Sunyaev, R. A., & Titarchuk, L. G., 1980, A&A, 86, 121
- Sunyaev, R. A., & Trümper, J., 1979, Nature, 279, 506
- Svensson, R., 1998, in Abramowicz, Bjornsson & Pringle (1998), 284
- Tanaka, Y., & Lewin, W. H. G., 1995, in X-ray Binaries, ed. W. H. G. Lewin, J. van Paradijs, E. P. J. van den Heuvel, (Cambridge: Univ. Cambridge Press), 126
- Terrell, N. J., 1972, ApJ, 174, L35
- Thorne, K. S., 1994, Black Holes and Time Warps, (New York, London: Norton)
- Titarchuk, L., 1994, ApJ, 434, 570
- Turolla, R., & Dullemond, C. P., 2000, ApJ, 531, L49
- Ueno, S., Mineshige, S., Negoro, H., Shibata, K., & Hudson, H. S., 1997, ApJ, 484, 920
- Uttley, P., & McHardy, I. M., 2001, MNRAS, 323, L26
- van der Klis, M., 1989, in Timing Neutron Stars, ed. H. Ögelman, E. P. J. van den Heuvel, (Dordrecht: Kluwer Academic Publishers), 27
- van der Klis, M., 1995, in X-ray Binaries, ed. W. H. G. Lewin, J. van Paradijs, E. P. J. van den Heuvel, (Cambridge: Univ. Cambridge Press), 252
- van der Klis, M., 2000, ARA&A, 38, 717
- van Straaten, S., van der Klis, M., di Salvo, T., Belloni, T., & Psaltis, D., 2002, ApJ, 568, 912
- Vasiliev, L., Trudolyubov, S., & Revnivtsev, M., 2000, A&A, 362, L53
- Vaughan, B. A., & Nowak, M. A., 1997, ApJ, 474, L43
- Vikhlinin, A., Churazov, E., & Gilfanov, M., 1994, A&A, 287, 73
- Voloshina, I. B., Lyuty, V. M., & Tarasov, A. E., 1997, Astron. Let., 23, 293
- Wade, C. M., & Hjellming, R. M., 1972, Nature, 235, 271
- Weisskopf, M. C., Kahn, S. M., & Sutherland, P. G., 1975, ApJ, 199, L147
- Weisskopf, M. C., & Sutherland, P. G., 1978, ApJ, 221, 228
- Weisskopf, M. C., Sutherland, P. G., Katz, J. I., & Canizares, C. R., 1978, ApJ, 223, L17
- Wen, L., Cui, W., & Bradt, H. V., 2001, ApJ, 546, L105
- Wen, L., Cui, W., Levine, A. M., & Bradt, H. V., 1999, ApJ, 525, 968
- White, N. E., & van Paradijs, J., 1996, ApJ, 473, L25
- Wijnands, R., & van der Klis, M., 1999, ApJ, 514, 939
- Wilms, J., 1998, *Ph.D. thesis*, Universität Tübingen, Tübingen
- Wilms, J., Nowak, M. A., Dove, J. B., Fender, R. P., & Matteo, T. D., 1999, ApJ, 522, 460
- Wilms, J., Nowak, M. A., Pottschmidt, K., Heindl, W. A., Dove, J. B., & Begelman, M. C., 2001, MNRAS, 320, 327
- Wilms, J., Reynolds, C., Begelman, M., Reeves, J., Molendi, S., Staubert, R., & Kendziorra, E., 2001, MNRAS, 328, L27
- Wu, H., Xue, S., Xia, X., Deng, Z., & Mao, S., 2002, ApJ, in press (astro-ph/0204359)
- Young, A. J., Fabian, A. C., Ross, R. R., & Tanaka, Y., 2001, MNRAS, 325, 1045
- Zdziarski, A. A., 1998, MNRAS, 296, L51
- Zdziarski, A. A., 2000, in Poutanen & Svensson (1999), 153
- Zdziarski, A. A., Grove, J. E., Poutanen, J.,

- Rao, A. R., & Vadawale, S. V., 2001, *ApJ*, 554, L45
- Zdziarski, A. A., Lubiński, P., & Smith, D. A., 1999, *MNRAS*, 303, L11
- Zhang, S. N., Cui, W., & Chen, W., 1997, *ApJ*, 482, L155
- Zhang, S. N., Cui, W., Harmon, B. A., Paciesas, W. S., Remillard, R., & van Paradijs, J., 1997a, *ApJ*, 477, L95
- Zhang, S. N., Mirabel, I. F., Harmon, B. A., Kroeger, R. A., Rodriguez, L. F., Hjellming, R. M., & Rupen, M. P., 1997b, in *Proc. 4th Compton Symposium*, ed. C. D. Dermer, M. S. Strickman, J. D. Kurfess, (Woodbury: AIP), 141
- Zhang, W., Jahoda, K., Swank, J. H., Morgan, E. H., & Giles, A. B., 1995, *ApJ*, 449, 930
- Zhang, W., Morgan, E. H., Jahoda, K., Swank, J. H., Strohmayer, T. E., Jernigan, G., & Klein, R. I., 1996, *ApJ*, 469, L29



## APPENDIX A

---

### **Table of Fit Results**

This appendix contains the table with the results of fitting multiple Lorentzians to selected power spectra of the Cyg X-1 RXTE/PCA monitoring observations from 1998–2001 in the frequency range from  $(1/512)$  Hz to 32 Hz (P30157) or 128 Hz (others), for the 2–13.1 keV band (Table 5.1 on p. 93). See chapter 5 for a definition of the symbols used. Pages 138 to 145 contain the best fit parameters for the four broad Lorentzians and the power-law, followed by the best fit parameters of the narrow QPOs on pages 146 to 149. All uncertainties are at the 68% level in units of the last digit shown. Where no uncertainties are given for parameters of the broad Lorentzians, these parameters have been held fixed. All parameters of the narrow Lorentzians were kept free parameters, however, no attempt was made to determine formal uncertainties for these parameters.

No	Prop.-ID	PCU off	JD-2400000	date	Exp. ks	$R_1$	$f_1$ $10^{-1}$ Hz	$Q_1$	$R_2$	$f_2$ Hz	$Q_2$
1	P30157-01	4	50793.725	1997.12.11	2.9	0.274(7)	0.44(2)	0.50	0.245(5)	3.36(14)	0.60
2	P30157-02		50800.798	1997.12.18	2.4	0.261(8)	0.35(2)	0.50	0.271(6)	2.97( $\frac{15}{3}$ )	0.60
3	P30157-03		50807.396	1997.12.24	3.0	0.302(9)	0.24(2)	0.50	0.263( $\frac{6}{7}$ )	2.08(11)	0.60
4	P30157-04		50813.263	1997.12.30	1.6	0.292( $\frac{11}{12}$ )	0.39(4)	0.50	0.259(9)	2.94( $\frac{27}{21}$ )	0.60
5	P30157-05		50821.698	1998.01.08	3.0	0.308(7)	0.34(2)	0.50	0.239(5)	3.42( $\frac{17}{6}$ )	0.60
6	P30157-06		50829.465	1998.01.15	3.4	0.334( $\frac{8}{9}$ )	0.35(2)	0.50	0.225(6)	3.63( $\frac{24}{22}$ )	0.60
7	P30157-07		50836.546	1998.01.23	2.9	0.286(7)	0.36(2)	0.50	0.244(6)	2.96(15)	0.60
8	P30157-08		50843.549	1998.01.30	2.5	0.302(7)	0.42(2)	0.50	0.231( $\frac{6}{5}$ )	4.15( $\frac{21}{21}$ )	0.60
9	P30157-09		50850.502	1998.02.06	2.4	0.284(7)	0.46(3)	0.50	0.227(6)	3.73( $\frac{20}{19}$ )	0.60
10	P30157-10		50858.480	1998.02.13	3.1	0.267(7)	0.52( $\frac{4}{3}$ )	0.50	0.233(6)	3.47( $\frac{18}{17}$ )	0.60
11	P30157-11		50865.481	1998.02.20	3.1	0.280(6)	0.37(2)	0.50	0.237(4)	3.98(15)	0.60
12	P30157-12		50872.614	1998.02.28	2.5	0.273( $\frac{7}{8}$ )	0.43( $\frac{3}{2}$ )	0.50	0.235(6)	3.35(18)	0.60
13	P30157-13		50883.284	1998.03.10	2.9	0.263( $\frac{8}{9}$ )	0.29(2)	0.50	0.268(5)	2.52( $\frac{11}{10}$ )	0.60
14	P30157-14		50889.285	1998.03.16	2.9	0.286(8)	0.29(2)	0.50	0.260( $\frac{5}{6}$ )	2.70( $\frac{13}{12}$ )	0.60
15	P30157-15		50896.495	1998.03.23	2.4	0.266(9)	0.31(2)	0.50	0.267(6)	2.50( $\frac{13}{12}$ )	0.60
16	P30157-16		50901.571	1998.03.29	2.2	0.274(9)	0.47(3)	0.50	0.236(7)	3.16( $\frac{25}{20}$ )	0.60
17	P30157-17		50909.362	1998.04.05	3.0	0.262(10)	0.32(3)	0.50	0.269( $\frac{7}{8}$ )	2.23( $\frac{13}{8}$ )	0.60
18	P30157-18	4	50916.637	1998.04.13	1.8	0.309( $\frac{9}{10}$ )	0.37(3)	0.50	0.236(8)	3.05( $\frac{25}{20}$ )	0.60
19	P30157-19	3	50925.429	1998.04.21	2.3	0.266(9)	0.34(2)	0.50	0.267(6)	2.88(13)	0.60
20	P30157-20	4	50932.095	1998.04.28	2.7	0.272(8)	0.41( $\frac{3}{2}$ )	0.50	0.242(7)	2.87( $\frac{18}{17}$ )	0.60
21	P30157-21		50939.509	1998.05.06	2.7	0.280(6)	0.46(2)	0.50	0.242(4)	4.26( $\frac{18}{17}$ )	0.60
22	P30157-22		50946.236	1998.05.12	2.6	0.246( $\frac{7}{8}$ )	0.37( $\frac{3}{2}$ )	0.50	0.261(5)	3.01( $\frac{14}{13}$ )	0.60
23	P30157-23		50953.379	1998.05.19	1.9	0.258(8)	0.52( $\frac{4}{3}$ )	0.50	0.254( $\frac{4}{6}$ )	3.96( $\frac{16}{18}$ )	0.60
24	P30157-24		50960.379	1998.05.26	2.2	0.260(5)	0.80(3)	0.50	0.216(4)	7.38( $\frac{31}{30}$ )	0.60
25	P30157-25		50966.378	1998.06.01	1.8	0.234(5)	1.14(5)	0.50	0.224(4)	9.74(38)	0.60
26	P30157-26	4	50973.376	1998.06.08	1.8	0.228(6)	1.04( $\frac{5}{4}$ )	0.50	0.228( $\frac{4}{5}$ )	7.82( $\frac{35}{34}$ )	0.60
27	P30157-27		50981.372	1998.06.16	3.2	0.235(4)	1.10(4)	0.50	0.228(3)	7.84(26)	0.60
28	P30157-28		50992.037	1998.06.27	3.3	0.255(4)	0.96(3)	0.50	0.220(3)	7.98( $\frac{38}{27}$ )	0.60
29	P30157-29		50997.108	1998.07.02	2.8	0.267(3)	1.94(5)	0.50	0.199(3)	24.98( $\frac{80}{81}$ )	0.96(4)
30	P30157-30		51004.256	1998.07.09	2.3	0.243(4)	1.75( $\frac{7}{6}$ )	0.50	0.230(4)	19.37( $\frac{84}{87}$ )	0.72(4)
31	P30157-31		51010.326	1998.07.15	1.9	0.230(5)	1.87(8)	0.50	0.243(5)	15.91( $\frac{116}{113}$ )	0.64(5)
32	P30157-32		51015.184	1998.07.20	2.5	0.254(3)	2.48( $\frac{6}{5}$ )	0.50	0.207(3)	28.14( $\frac{85}{86}$ )	0.97(4)
33	P30157-33		51024.319	1998.07.29	1.9	0.257(4)	2.49(8)	0.50	0.222( $\frac{4}{5}$ )	24.59( $\frac{29}{20}$ )	0.81( $\frac{6}{5}$ )
34	P30157-34		51031.381	1998.08.05	2.8	0.225( $\frac{4}{5}$ )	0.99(4)	0.50	0.232(3)	7.92( $\frac{22}{24}$ )	0.60
35	P30157-35		51038.112	1998.08.12	2.9	0.226(4)	0.96(4)	0.50	0.227(3)	8.13( $\frac{24}{23}$ )	0.60
36	P30157-36		51043.055	1998.08.17	2.8	0.225(4)	0.94(4)	0.50	0.223(3)	7.61(27)	0.60
37	P30157-37	4	51052.125	1998.08.26	2.3	0.257( $\frac{5}{6}$ )	0.70(3)	0.50	0.237(4)	5.96( $\frac{23}{22}$ )	0.60
38	P30157-38		51058.859	1998.09.02	2.3	0.221(5)	0.78(4)	0.50	0.240(4)	6.12( $\frac{21}{20}$ )	0.60
39	P30157-39		51065.987	1998.09.09	2.2	0.226(5)	1.03(5)	0.50	0.235( $\frac{3}{4}$ )	8.07( $\frac{28}{27}$ )	0.60
40	P30157-40		51072.986	1998.09.16	2.7	0.219(5)	1.06(5)	0.50	0.225(4)	7.44( $\frac{28}{27}$ )	0.60

No	$R_3$	$f_3$ Hz	$Q_3$	$R_4$	$f_4$ Hz	$Q_4$	$A_{\text{PL}}$	$\alpha$	$\chi^2/\text{dof}$	$\chi^2_{\text{red}}$
1	0.204(2)	2.01(4)	0.60	0.042( $\frac{339}{16}$ )	44.32( $\frac{78441}{1997}$ )	1.00	...	...	92.4/ 58	1.59
2	0.209(3)	1.91(4)	0.60	0.053( $\frac{82}{15}$ )	42.55( $\frac{14047}{1611}$ )	1.00	...	...	64.5/ 58	1.11
3	0.236(2)	1.59(3)	0.60	0.048( $\frac{158}{15}$ )	39.68( $\frac{19092}{1699}$ )	1.00	...	...	51.4/ 58	0.89
4	0.228(4)	1.66(5)	0.60	0.047( $\frac{238}{18}$ )	46.40( $\frac{67490}{1904}$ )	1.00	...	...	66.8/ 58	1.15
5	0.213(3)	1.76(4)	0.60	0.046( $\frac{282}{20}$ )	52.11( $\frac{45704}{2837}$ )	1.00	...	...	58.9/ 58	1.01
6	0.208(4)	1.83(5)	0.60	0.040( $\frac{12}{5}$ )	20.79( $\frac{1531}{445}$ )	1.00	...	...	50.5/ 58	0.87
7	0.209(3)	1.82(4)	0.60	0.047( $\frac{379}{17}$ )	46.01( $\frac{54777}{2029}$ )	1.00	...	...	80.7/ 61	1.32
8	0.202( $\frac{3}{2}$ )	2.00(5)	0.60	0.051( $\frac{92}{13}$ )	38.86( $\frac{13712}{1428}$ )	1.00	0.00	1.41	65.0/ 59	1.10
9	0.193(3)	2.03(5)	0.60	0.047( $\frac{42}{13}$ )	41.39( $\frac{7225}{1427}$ )	1.00	...	...	99.8/ 58	1.72
10	0.197(2)	2.07(4)	0.60	0.039( $\frac{108}{15}$ )	43.86( $\frac{39770}{1795}$ )	1.00	0.00	1.57	82.6/ 59	1.40
11	0.191(3)	1.98(4)	0.60	0.038( $\frac{30}{11}$ )	41.38( $\frac{5739}{1359}$ )	1.00	...	...	75.5/ 58	1.30
12	0.211(3)	1.84(4)	0.60	0.037( $\frac{41}{12}$ )	43.06( $\frac{9778}{1552}$ )	1.00	...	...	72.1/ 58	1.24
13	0.218(2)	1.72(3)	0.60	0.059( $\frac{130}{16}$ )	40.50( $\frac{18792}{1599}$ )	1.00	...	...	84.7/ 58	1.46
14	0.225(2)	1.78(3)	0.60	0.050( $\frac{53}{13}$ )	40.48( $\frac{10725}{1415}$ )	1.00	...	...	64.8/ 58	1.12
15	0.219(3)	1.78(3)	0.60	0.051( $\frac{54}{15}$ )	44.67( $\frac{8957}{1587}$ )	1.00	...	...	62.9/ 58	1.08
16	0.228(3)	1.78(4)	0.60	0.052( $\frac{378}{18}$ )	49.41( $\frac{50897}{1885}$ )	1.00	...	...	115.5/ 61	1.89
17	0.224(2)	1.73(3)	0.60	0.057( $\frac{121}{16}$ )	40.34( $\frac{16434}{1598}$ )	1.00	...	...	56.8/ 61	0.93
18	0.221(3)	1.89( $\frac{5}{4}$ )	0.60	0.048( $\frac{157}{16}$ )	40.18( $\frac{30464}{1686}$ )	1.00	...	...	65.1/ 58	1.12
19	0.208(3)	1.99(4)	0.60	0.049( $\frac{387}{17}$ )	42.48( $\frac{47677}{1766}$ )	1.00	...	...	88.5/ 61	1.45
20	0.215(3)	1.80(4)	0.60	0.057( $\frac{46}{16}$ )	44.24( $\frac{6573}{1473}$ )	1.00	...	...	78.3/ 58	1.35
21	0.191(3)	2.13(5)	0.60	0.051( $\frac{52}{12}$ )	37.51( $\frac{6835}{1226}$ )	1.00	...	...	63.0/ 58	1.09
22	0.207(3)	1.95(4)	0.60	0.048( $\frac{190}{16}$ )	45.20( $\frac{57782}{1906}$ )	1.00	...	...	75.9/ 58	1.31
23	0.177( $\frac{3}{2}$ )	2.40( $\frac{4}{3}$ )	0.60	0.031( $\frac{324}{11}$ )	45.79( $\frac{18270}{2250}$ )	1.00	...	...	62.2/ 58	1.07
24	0.125( $\frac{3}{2}$ )	2.77( $\frac{15}{14}$ )	0.60	0.040( $\frac{136}{14}$ )	46.05( $\frac{55304}{1863}$ )	1.00	...	...	65.6/ 61	1.08
25	0.104( $\frac{4}{6}$ )	3.66( $\frac{31}{32}$ )	0.60	0.047( $\frac{370}{20}$ )	48.19( $\frac{154284}{1905}$ )	1.00	...	...	64.4/ 58	1.11
26	0.127( $\frac{3}{5}$ )	3.29( $\frac{19}{23}$ )	0.60	0.053( $\frac{890}{33}$ )	57.23( $\frac{135712}{4918}$ )	1.00	...	...	87.9/ 58	1.51
27	0.123(3)	3.40(16)	0.60	0.045( $\frac{408}{19}$ )	45.54( $\frac{81682}{2446}$ )	1.00	...	...	61.1/ 61	1.00
28	0.132( $\frac{3}{4}$ )	3.24( $\frac{14}{13}$ )	0.60	0.041( $\frac{371}{14}$ )	43.30( $\frac{57754}{2114}$ )	1.00	...	...	61.2/ 61	1.00
29	...	...	...	0.065( $\frac{50}{16}$ )	49.80( $\frac{6668}{1590}$ )	1.00	0.00	1.15	64.2/ 60	1.07
30	...	...	...	0.079( $\frac{56}{19}$ )	49.52( $\frac{5804}{1528}$ )	1.00	...	...	69.5/ 59	1.18
31	...	...	...	0.086( $\frac{163}{26}$ )	53.87( $\frac{19659}{2116}$ )	1.00	...	...	62.1/ 62	1.00
32	...	...	...	0.080( $\frac{26}{14}$ )	46.14( $\frac{7273}{1043}$ )	1.00	...	...	113.1/ 62	1.82
33	...	...	...	0.087( $\frac{273}{30}$ )	62.10( $\frac{27764}{3085}$ )	1.00	...	...	91.3/ 62	1.47
34	0.129( $\frac{1}{4}$ )	3.50( $\frac{8}{14}$ )	0.60	0.030( $\frac{274}{19}$ )	48.15( $\frac{113359}{4198}$ )	1.00	...	...	110.6/ 58	1.91
35	0.132( $\frac{2}{3}$ )	3.44( $\frac{10}{12}$ )	0.60	0.033( $\frac{458}{11}$ )	46.34( $\frac{180943}{1955}$ )	1.00	...	...	96.0/ 58	1.66
36	0.133(4)	3.14( $\frac{13}{12}$ )	0.60	0.055( $\frac{40}{14}$ )	44.07( $\frac{5338}{1739}$ )	1.00	...	...	96.8/ 61	1.59
37	0.153(3)	2.88( $\frac{10}{13}$ )	0.60	0.043( $\frac{205}{15}$ )	42.42( $\frac{57799}{1739}$ )	1.00	...	...	73.2/ 58	1.26
38	0.145(3)	3.16(10)	0.60	0.038( $\frac{293}{16}$ )	45.11( $\frac{132575}{1637}$ )	1.00	...	...	88.1/ 58	1.52
39	0.121( $\frac{4}{3}$ )	3.73( $\frac{16}{15}$ )	0.60	...	...	...	...	...	72.8/ 60	1.21
40	0.133(3)	3.27(12)	0.60	...	...	...	...	...	54.6/ 57	0.96

No	Prop.-ID	PCU off	JD-2400000	date	Exp. ks	$R_1$	$f_1$ $10^{-1}$ Hz	$Q_1$	$R_2$	$f_2$ Hz	$Q_2$
41	P30157-42	4	51082.411	1998.09.25	2.3	0.254	1.04	0.50	0.219( $\frac{6}{5}$ )	8.29(20)	0.60
42	P30157-43		51094.723	1998.10.08	2.8	0.258(5)	0.99(4)	0.50	0.219(4)	8.75(41)	0.60
43	P30157-44	4	51100.822	1998.10.14	2.5	0.244(5)	1.22(5)	0.50	0.210(4)	8.53( $\frac{40}{39}$ )	0.60
44	P30157-46		51115.527	1998.10.29	2.3	0.257(5)	1.09( $\frac{5}{6}$ )	0.50	0.217(4)	8.48( $\frac{40}{38}$ )	0.60
45	P30157-47		51121.920	1998.11.04	2.2	0.241(5)	0.92(4)	0.50	0.215(4)	7.07( $\frac{27}{26}$ )	0.60
46	P30157-48		51128.917	1998.11.11	1.8	0.256(5)	1.05(5)	0.50	0.208( $\frac{4}{5}$ )	8.61( $\frac{48}{45}$ )	0.60
47	P30157-49		51138.109	1998.11.20	2.8	0.250(4)	1.22(4)	0.50	0.224(3)	10.78(36)	0.60
48	P30157-50	4	51143.914	1998.11.26	2.8	0.236(4)	1.68(6)	0.50	0.232(3)	13.18( $\frac{38}{30}$ )	0.60
49	P30157-51		51150.504	1998.12.03	2.6	0.243(4)	1.44(5)	0.50	0.230( $\frac{4}{5}$ )	12.48( $\frac{46}{49}$ )	0.60
50	P30157-52		51156.849	1998.12.09	2.8	0.235( $\frac{3}{5}$ )	1.49(5)	0.50	0.221( $\frac{4}{6}$ )	12.73( $\frac{48}{34}$ )	0.60
51	P40099-01		51192.892	1999.01.14	7.8	0.228(2)	1.76( $\frac{3}{4}$ )	0.50	0.239(1)	15.27( $\frac{20}{22}$ )	0.60
52	P40099-02		51206.843	1999.01.28	3.8	0.248(4)	0.88(3)	0.50	0.227(3)	7.71(22)	0.60
53	P40099-03		51220.624	1999.02.11	6.0	0.254( $\frac{3}{4}$ )	0.68(2)	0.50	0.228(3)	5.58( $\frac{13}{13}$ )	0.60
54	P40099-04		51234.821	1999.02.25	8.3	0.241(2)	0.99(2)	0.50	0.221(2)	8.68(17)	0.60
55	P40099-05	14	51251.730	1999.03.14	3.2	0.247(3)	1.30(4)	0.50	0.226(2)	13.35(29)	0.60
56	P40099-05	1	51251.663	1999.03.14	5.2	0.270(3)	1.29(3)	0.50	0.230(2)	12.12( $\frac{31}{34}$ )	0.60
57	P40099-08	1	51293.513	1999.04.25	7.4	0.276(2)	0.97(2)	0.50	0.224(2)	10.16( $\frac{23}{21}$ )	0.60
58	P40099-10	4	51319.714	1999.05.21	5.2	0.256(2)	1.55(3)	0.50	0.233(2)	14.99(26)	0.60
59	P40099-11	14	51334.487	1999.06.04	3.2	0.228(4)	1.06(4)	0.50	0.227(3)	9.08( $\frac{32}{30}$ )	0.60
60	P40099-11	1	51334.693	1999.06.05	5.1	0.232(3)	1.20(4)	0.50	0.223(2)	9.26(24)	0.60
61	P40099-12	13	51352.457	1999.06.22	6.8	0.239(2)	1.52(3)	0.50	0.231(2)	13.28( $\frac{26}{28}$ )	0.60
62	P40099-13	14	51365.402	1999.07.05	6.3	0.237(2)	1.36(3)	0.50	0.227( $\frac{2}{3}$ )	12.31( $\frac{30}{31}$ )	0.60
63	P40099-14	14	51379.385	1999.07.19	3.0	0.223(4)	1.45(6)	0.50	0.241( $\frac{3}{4}$ )	11.94( $\frac{45}{30}$ )	0.60
64	P40099-15	14	51390.367	1999.07.30	9.0	0.270( $\frac{6}{5}$ )	1.40( $\frac{13}{15}$ )	0.37(5)	0.181( $\frac{8}{9}$ )	21.34( $\frac{84}{89}$ )	1.08( $\frac{11}{9}$ )
65	P40099-16	14	51407.269	1999.08.16	6.5	0.262(2)	1.59(3)	0.50	0.231( $\frac{1}{2}$ )	14.52(21)	0.60
66	P40099-17	14	51420.280	1999.08.29	5.1	0.302(3)	1.42(3)	0.50	0.230(2)	14.49( $\frac{32}{34}$ )	0.60
67	P40099-18	14	51435.259	1999.09.13	3.7	0.273( $\frac{3}{4}$ )	0.99(3)	0.50	0.222( $\frac{3}{4}$ )	10.14( $\frac{36}{37}$ )	0.60
68	P40099-19	13	51447.164	1999.09.25	8.1	0.278(2)	2.94(4)	0.50	0.194(2)	33.10( $\frac{72}{68}$ )	1.06(3)
69	P40099-20	3	51464.133	1999.10.12	2.8	0.248(3)	2.06(6)	0.50	0.240(2)	18.24( $\frac{29}{36}$ )	0.60
70	P40099-21	14	51476.142	1999.10.24	5.7	0.257(2)	2.16(4)	0.50	0.213(2)	28.35(71)	0.94(3)
71	P40099-22		51491.315	1999.11.08	2.2	0.251(4)	1.71(6)	0.50	0.237(3)	15.13( $\frac{40}{41}$ )	0.60
72	P40099-22	14	51491.114	1999.11.08	4.8	0.240(3)	1.62(4)	0.50	0.246(2)	15.73( $\frac{20}{19}$ )	0.60
73	P40099-23		51506.080	1999.11.23	5.9	0.235( $\frac{2}{3}$ )	1.26(3)	0.50	0.226(2)	10.71(23)	0.60
74	P40099-23	14	51506.144	1999.11.23	2.9	0.220(6)	1.42( $\frac{9}{8}$ )	0.50	0.223(4)	10.15(49)	0.60
75	P40099-24		51517.986	1999.12.05	3.1	...	...	...	0.190(3)	10.86( $\frac{48}{68}$ )	0.61(5)
76	P40099-24	14	51518.188	1999.12.05	1.9	0.077(3)	0.42( $\frac{6}{5}$ )	0.50	0.188( $\frac{4}{5}$ )	17.69( $\frac{46}{36}$ )	0.79( $\frac{9}{7}$ )
77	P40099-25	134	51530.059	1999.12.17	2.8	0.266(3)	2.58(7)	0.50	0.207(4)	27.65( $\frac{115}{117}$ )	0.96(5)
78	P40099-26	14	51544.025	1999.12.31	3.6	0.245(4)	1.22(4)	0.50	0.221(3)	9.61( $\frac{31}{36}$ )	0.60
79	P40099-27	134	51557.982	2000.01.14	4.4	0.271(3)	1.73( $\frac{3}{4}$ )	0.50	0.230(2)	16.68( $\frac{23}{22}$ )	0.60
80	P40099-28	14	51572.838	2000.01.29	3.3	0.261(3)	1.96(5)	0.50	0.235(2)	17.51(26)	0.60

No	$R_3$	$f_3$ Hz	$Q_3$	$R_4$	$f_4$ Hz	$Q_4$	$A_{PL}$	$\alpha$	$\chi^2/\text{dof}$	$\chi^2_{\text{red}}$
41	0.117(5)	$3.19(\frac{13}{5})$	0.60	...	...	...	...	...	68.9/ 62	1.11
42	$0.128(\frac{5}{7})$	$3.03(\frac{19}{18})$	0.60	$0.049(\frac{109}{16})$	$44.42(\frac{24676}{1768})$	1.00	...	...	63.6/ 58	1.10
43	0.118(5)	$3.40(\frac{24}{22})$	0.60	$0.058(\frac{469}{22})$	$48.03(\frac{123204}{2184})$	1.00	...	...	110.2/ 61	1.81
44	$0.123(\frac{4}{5})$	$3.13(\frac{20}{18})$	0.60	$0.046(\frac{402}{19})$	$45.21(\frac{92573}{2130})$	1.00	...	...	71.3/ 58	1.23
45	0.143(3)	$3.27(\frac{41}{14})$	0.60	...	...	...	...	...	91.4/ 63	1.45
46	$0.134(\frac{3}{5})$	$3.20(\frac{15}{18})$	0.60	$0.042(\frac{377}{20})$	$45.69(\frac{101706}{2273})$	1.00	...	...	43.1/ 58	0.74
47	0.105(5)	$3.95(\frac{28}{26})$	0.60	$0.054(\frac{171}{18})$	$46.69(\frac{30995}{1865})$	1.00	...	...	74.1/ 58	1.28
48	0.072(6)	$5.11(\frac{74}{70})$	0.60	$0.037(\frac{144}{15})$	$38.51(\frac{36039}{1335})$	1.00	...	...	91.6/ 58	1.58
49	$0.093(\frac{11}{10})$	$3.47(\frac{41}{44})$	0.60	$0.068(\frac{40}{16})$	$49.05(\frac{4858}{1438})$	1.00	...	...	105.7/ 58	1.82
50	$0.082(\frac{14}{12})$	$3.25(\frac{51}{44})$	0.60	$0.060(\frac{46}{15})$	$48.02(\frac{6345}{1539})$	1.00	0.00	1.34	75.3/ 56	1.35
51	$0.041(\frac{6}{7})$	$5.66(\frac{137}{113})$	0.60	$0.063(\frac{1}{2})$	$28.13(\frac{104}{97})$	1.00	0.00	1.00	103.0/ 66	1.56
52	0.136(3)	$3.53(12)$	0.60	0.050(2)	$25.12(\frac{186}{168})$	1.00	...	...	71.0/ 65	1.09
53	0.161(2)	$2.82(6)$	0.60	$0.054(\frac{1}{2})$	$25.60(\frac{143}{133})$	1.00	...	...	52.8/ 68	0.78
54	0.120(2)	$3.61(\frac{15}{11})$	0.60	0.054(1)	$26.73(\frac{122}{113})$	1.00	0.00	1.87	110.2/ 63	1.75
55	$0.052(\frac{6}{9})$	$5.93(\frac{196}{147})$	0.60	$0.046(\frac{4}{5})$	$29.43(\frac{670}{441})$	1.00	0.00	3.25	74.2/ 63	1.18
56	0.073(6)	$4.28(\frac{33}{47})$	0.60	0.041(3)	$26.94(\frac{380}{238})$	1.00	0.00	2.67	114.4/ 63	1.82
57	0.108(3)	$3.90(\frac{19}{17})$	0.60	0.047(2)	$31.74(\frac{251}{238})$	1.00	0.00	2.02	104.0/ 66	1.58
58	$0.044(\frac{6}{7})$	$5.68(\frac{149}{113})$	0.60	$0.050(\frac{2}{3})$	$24.20(\frac{169}{147})$	1.00	0.00	1.03	118.4/ 63	1.88
59	0.123(4)	$3.72(\frac{23}{21})$	0.60	0.053(3)	$30.91(\frac{450}{365})$	1.00	0.00	3.56	49.5/ 66	0.75
60	0.115(3)	$3.69(\frac{17}{16})$	0.60	0.056(2)	$27.25(\frac{172}{160})$	1.00	0.00	1.01	98.2/ 63	1.56
61	0.076(5)	$4.79(\frac{64}{52})$	0.60	0.059(2)	$27.50(\frac{181}{163})$	1.00	0.00	1.50	83.3/ 63	1.32
62	0.087(6)	$3.87(\frac{41}{37})$	0.60	0.052(2)	$25.09(\frac{201}{178})$	1.00	0.00	0.92	101.8/ 66	1.54
63	$0.093(\frac{11}{9})$	$3.80(\frac{61}{55})$	0.60	0.067(3)	$24.88(\frac{190}{170})$	1.00	...	...	81.7/ 65	1.26
64	$0.090(\frac{11}{10})$	$3.92(\frac{42}{42})$	0.60	0.043(2)	$27.92(\frac{352}{227})$	1.00	0.00	0.96	90.6/ 67	1.35
65	$0.028(\frac{4}{3})$	$10.60(\frac{33}{37})$	$4.73(\frac{164}{123})$	0.055(2)	$26.87(\frac{213}{191})$	1.00	0.00	0.97	58.6/ 68	0.86
66	$0.059(\frac{8}{7})$	$4.93(\frac{115}{90})$	0.60	0.044(4)	$24.61(\frac{357}{270})$	1.00	0.00	1.16	94.6/ 69	1.37
67	$0.102(\frac{7}{6})$	$3.60(\frac{41}{37})$	0.60	0.047(4)	$28.08(\frac{557}{457})$	1.00	0.00	2.00	71.5/ 63	1.13
68	...	...	...	$0.058(\frac{2}{1})$	$28.97(\frac{148}{136})$	1.00	0.00	1.24	137.4/ 70	1.96
69	...	...	...	0.053(2)	$28.33(\frac{206}{190})$	1.00	0.00	1.28	121.9/ 64	1.90
70	...	...	...	0.065(2)	$30.88(\frac{171}{157})$	1.00	0.00	2.57	77.9/ 64	1.22
71	0.056(9)	$5.32(\frac{137}{103})$	0.60	0.062(3)	$30.03(\frac{221}{194})$	1.00	...	...	63.1/ 71	0.89
72	...	...	...	0.070(2)	$27.74(\frac{151}{144})$	1.00	...	...	54.8/ 67	0.82
73	0.104(3)	$4.15(\frac{22}{21})$	0.60	0.058(2)	$28.74(\frac{179}{161})$	1.00	...	...	108.3/ 62	1.75
74	0.108(6)	$4.36(\frac{57}{48})$	0.60	$0.058(\frac{5}{6})$	$30.73(\frac{667}{487})$	1.00	...	...	68.5/ 62	1.11
75	0.076(4)	$7.10(25)$	$1.83(\frac{14}{13})$	$0.060(\frac{6}{3})$	$85.82(\frac{1475}{871})$	1.00	0.00	1.07	116.9/ 69	1.69
76	0.066(7)	$7.99(\frac{58}{61})$	$1.59(\frac{23}{19})$	...	...	...	0.00	1.02	100.7/ 66	1.53
77	...	...	...	$0.033(\frac{5}{6})$	$25.32(\frac{955}{621})$	1.00	0.00	0.78	102.9/ 67	1.54
78	0.109(4)	$4.14(\frac{30}{28})$	0.60	0.060(3)	$29.14(\frac{309}{270})$	1.00	...	...	93.4/ 68	1.37
79	...	...	...	0.063(2)	$29.70(\frac{183}{169})$	1.00	0.00	1.96	104.0/ 69	1.51
80	...	...	...	0.055(2)	$30.11(\frac{270}{242})$	1.00	0.00	1.23	97.1/ 71	1.37

No	Prop.-ID	PCU off	JD-2400000	date	Exp. ks	$R_1$	$f_1$ $10^{-1}$ Hz	$Q_1$	$R_2$	$f_2$ Hz	$Q_2$
81	P50110-01	13/34	51614.728	2000.03.11	9.2	0.261(2)	1.60(3)	0.50	0.244( $\frac{1}{3}$ )	14.97( $\frac{20}{37}$ )	0.60
82	P50110-02	14	51629.718	2000.03.26	2.9	0.224(5)	2.93( $\frac{18}{20}$ )	0.70(8)	0.216(4)	26.99( $\frac{96}{98}$ )	0.94(4)
83	P50110-03	014	51642.749	2000.04.08	2.5	0.267(4)	1.55( $\frac{6}{5}$ )	0.50	0.214( $\frac{3}{11}$ )	13.41( $\frac{45}{112}$ )	0.60
84	P50110-03	14	51642.611	2000.04.08	3.0	0.282( $\frac{3}{4}$ )	1.38(4)	0.50	0.218(3)	13.81( $\frac{42}{46}$ )	0.60
85	P50110-04	14	51655.700	2000.04.21	12.9	0.236(2)	0.69(2)	0.50	0.232(2)	6.36(11)	0.60
86	P50110-05	14	51670.541	2000.05.06	8.7	0.270(3)	0.84(2)	0.50	0.215(2)	7.97(19)	0.60
87	P50110-06	014	51684.493	2000.05.19	4.7	0.263( $\frac{4}{5}$ )	0.62(2)	0.50	0.221( $\frac{3}{4}$ )	5.44( $\frac{23}{25}$ )	0.60
88	P50110-07		51697.722	2000.06.02	0.7	0.239( $\frac{8}{9}$ )	1.11(9)	0.50	0.213( $\frac{6}{7}$ )	9.13( $\frac{98}{70}$ )	0.60
89	P50110-07	14	51697.530	2000.06.02	1.2	0.263( $\frac{36}{39}$ )	0.97( $\frac{48}{304}$ )	0.50	0.230( $\frac{100}{39}$ )	8.88( $\frac{366}{648}$ )	0.60
90	P50110-08	1/4	51712.457	2000.06.16	11.8	0.253(2)	1.05(2)	0.50	0.217(2)	9.31(17)	0.60
91	P50110-09	1	51729.419	2000.07.03	4.4	0.247(4)	1.09(4)	0.50	0.210(3)	9.19(32)	0.60
92	P50110-10		51740.521	2000.07.15	1.0	0.218( $\frac{10}{11}$ )	1.17( $\frac{10}{9}$ )	0.50	0.214(8)	6.12( $\frac{47}{3}$ )	0.60
93	P50110-10	134	51740.382	2000.07.14	3.0	0.243(5)	0.99(4)	0.50	0.211(4)	7.23( $\frac{33}{31}$ )	0.60
94	P50110-10	14	51740.591	2000.07.15	1.2	0.237( $\frac{11}{13}$ )	1.08( $\frac{18}{16}$ )	0.50	0.215(10)	6.97( $\frac{69}{62}$ )	0.60
95	P50110-11	1	51754.328	2000.07.28	7.2	0.284(3)	0.86(2)	0.50	0.208(2)	9.04(24)	0.60
96	P50110-12	13/34	51768.265	2000.08.11	5.3	0.264(3)	1.00(3)	0.50	0.214(3)	8.25(24)	0.60
97	P50110-12	1/4	51768.265	2000.08.11	4.9	0.286(3)	1.09(3)	0.50	0.212(3)	9.40(31)	0.60
98	P50110-13	1	51784.298	2000.08.27	3.4	0.269(3)	1.73( $\frac{5}{4}$ )	0.50	0.229(2)	15.89( $\frac{29}{30}$ )	0.60
99	P50110-15	14	51811.248	2000.09.23	6.9	0.261(2)	1.40(3)	0.50	0.233(2)	13.16( $\frac{27}{29}$ )	0.60
100	P50110-15	1	51811.400	2000.09.23	3.0	0.251(3)	1.41(4)	0.50	0.230( $\frac{3}{4}$ )	13.19( $\frac{46}{51}$ )	0.60
101	P50110-16		51827.106	2000.10.09	3.4	0.241(3)	1.38(4)	0.50	0.220(2)	11.90(31)	0.60
102	P50110-16	134	51827.246	2000.10.09	3.0	0.254(4)	1.51(5)	0.50	0.225(3)	13.36( $\frac{44}{46}$ )	0.60
103	P50110-16	4	51827.106	2000.10.09	3.2	0.253(3)	1.37(4)	0.50	0.225( $\frac{2}{3}$ )	13.70(34)	0.60
104	P50110-17	1/4	51838.083	2000.10.20	4.2	0.247(3)	1.61(4)	0.50	0.231(2)	14.93( $\frac{27}{30}$ )	0.60
105	P50110-18	1	51852.089	2000.11.03	5.7	0.053(2)	0.80(10)	0.50	0.182(5)	16.36( $\frac{54}{56}$ )	0.73( $\frac{5}{7}$ )
106	P50110-19		51867.140	2000.11.18	3.3	0.270(2)	2.84(6)	0.50	0.178(2)	34.77( $\frac{84}{86}$ )	1.18(4)
107	P50110-19	14	51867.011	2000.11.18	11.1	0.278(2)	2.74(5)	0.50	0.187(2)	33.66( $\frac{76}{77}$ )	1.14( $\frac{4}{5}$ )
108	P50110-20		51879.957	2000.12.01	3.2	0.233(3)	1.58(5)	0.50	0.226( $\frac{2}{3}$ )	13.55( $\frac{39}{37}$ )	0.60
109	P50110-20	14	51879.957	2000.12.01	4.2	0.233(3)	1.62(5)	0.50	0.227( $\frac{3}{4}$ )	13.19( $\frac{45}{54}$ )	0.60
110	P50110-20	1	51880.148	2000.12.01	2.6	0.244(4)	1.74(6)	0.50	0.230(3)	14.52( $\frac{40}{43}$ )	0.60
111	P50110-21	1/4	51895.962	2000.12.17	5.4	0.244(4)	2.73( $\frac{15}{16}$ )	0.58(5)	0.208(3)	28.00( $\frac{75}{76}$ )	0.94(3)
112	P50110-22	14	51911.877	2001.01.02	3.4	0.250(3)	1.70(4)	0.50	0.221(2)	16.04(23)	0.60
113	P50110-22	3	51912.011	2001.01.02	3.5	0.256(3)	1.68(5)	0.50	0.232(2)	15.46(22)	0.60
114	P50110-23	13/34	51925.862	2001.01.16	10.9	0.195(2)	5.58(9)	1.04(4)	0.179(1)	40.52(49)	1.26(2)
115	P50110-24	14	51938.816	2001.01.29	6.3	0.091( $\frac{4}{13}$ )	0.00( $\frac{18}{0}$ )	0.00( $\frac{18}{0}$ )	0.138(2)	40.28( $\frac{54}{56}$ )	1.07(4)
116	P50110-25	14	51950.824	2001.02.10	4.8	0.273(4)	3.21( $\frac{17}{18}$ )	0.56(5)	0.167(4)	37.07( $\frac{64}{67}$ )	1.67(9)
117	P50110-26	14	51963.886	2001.02.23	8.3	0.277(2)	1.61(3)	0.50	0.228( $\frac{2}{3}$ )	15.39( $\frac{28}{32}$ )	0.60
118	P50110-27	14	51600.772	2000.02.26	5.1	0.284( $\frac{6}{5}$ )	1.86( $\frac{13}{14}$ )	0.51(5)	0.195(6)	25.09( $\frac{113}{116}$ )	1.00( $\frac{8}{8}$ )
119	P50110-28	13/14	51586.089	2000.02.11	3.6	0.275(3)	2.42(6)	0.50	0.184( $\frac{8}{11}$ )	30.18( $\frac{99}{107}$ )	1.20( $\frac{12}{11}$ )
120	P50110-29	14	51996.651	2001.03.28	4.9	0.271(3)	1.00(3)	0.50	0.213(3)	9.02( $\frac{29}{33}$ )	0.60

No	$R_3$	$f_3$ Hz	$Q_3$	$R_4$	$f_4$ Hz	$Q_4$	$A_{\text{PL}}$	$\alpha$	$\chi^2/\text{dof}$	$\chi^2_{\text{red}}$
81	0.052( $\frac{7}{6}$ )	5.41( $\frac{95}{77}$ )	0.60	0.066(2)	30.08( $\frac{136}{124}$ )	1.00	0.00	1.83	124.2/ 66	1.88
82	...	...	...	0.066(2)	33.57( $\frac{235}{210}$ )	1.00	0.00	1.31	56.3/ 60	0.94
83	0.057( $\frac{7}{22}$ )	6.21( $\frac{197}{181}$ )	0.60	0.017( $\frac{52}{7}$ )	37.06( $\frac{9782}{3261}$ )	1.00	0.00	1.01	89.4/ 66	1.36
84	0.064( $\frac{9}{7}$ )	5.08( $\frac{133}{105}$ )	0.60	0.039( $\frac{4}{5}$ )	29.25( $\frac{559}{448}$ )	1.00	0.00	1.35	80.5/ 66	1.22
85	0.149(2)	3.02(6)	0.60	0.057(2)	25.34( $\frac{139}{130}$ )	1.00	...	...	86.7/ 65	1.33
86	0.134(2)	3.13( $\frac{10}{9}$ )	0.60	0.051(2)	26.61( $\frac{196}{177}$ )	1.00	0.00	1.62	91.0/ 66	1.38
87	0.156(3)	2.54( $\frac{11}{10}$ )	0.60	0.054(4)	21.83( $\frac{311}{277}$ )	1.00	0.00	1.12	52.5/ 69	0.76
88	0.096( $\frac{11}{10}$ )	3.35( $\frac{68}{48}$ )	0.60	0.044(4)	24.88( $\frac{499}{380}$ )	1.00	...	...	51.1/ 65	0.79
89	0.107(11)	3.95( $\frac{250}{129}$ )	0.60	0.045( $\frac{9}{12}$ )	36.87( $\frac{3456}{1675}$ )	1.00	...	...	39.4/ 71	0.55
90	0.117(2)	3.65(12)	0.60	0.051(2)	25.96( $\frac{151}{142}$ )	1.00	...	...	82.9/ 68	1.22
91	0.102(5)	3.35( $\frac{30}{25}$ )	0.60	0.039(4)	21.02( $\frac{364}{291}$ )	1.00	0.00	1.11	120.4/ 69	1.75
92	0.147(5)	2.93( $\frac{19}{17}$ )	0.60	0.061(4)	32.11( $\frac{541}{444}$ )	1.00	...	...	90.3/ 68	1.33
93	0.135(4)	3.29( $\frac{21}{19}$ )	0.60	0.059(6)	36.40( $\frac{1262}{709}$ )	1.00	...	...	62.7/ 68	0.92
94	0.134(6)	3.30( $\frac{31}{28}$ )	0.60	0.061( $\frac{6}{8}$ )	28.00( $\frac{758}{552}$ )	1.00	...	...	68.5/ 67	1.02
95	0.105(4)	3.15( $\frac{17}{16}$ )	0.60	0.036(2)	26.52( $\frac{316}{275}$ )	1.00	0.00	1.29	87.8/ 69	1.27
96	0.124(3)	3.52( $\frac{17}{16}$ )	0.60	0.055(3)	28.54( $\frac{386}{318}$ )	1.00	...	...	86.3/ 71	1.22
97	0.124(4)	3.51( $\frac{19}{18}$ )	0.60	0.049(3)	25.82( $\frac{328}{373}$ )	1.00	...	...	67.3/ 71	0.95
98	0.024( $\frac{12}{3}$ )	6.63( $\frac{1260}{420}$ )	0.60	0.053( $\frac{3}{3}$ )	25.78( $\frac{182}{161}$ )	1.00	0.00	1.56	102.9/ 69	1.49
99	0.082( $\frac{5}{5}$ )	4.38( $\frac{47}{42}$ )	0.60	0.061(2)	27.57( $\frac{166}{146}$ )	1.00	0.00	1.89	62.3/ 69	0.90
100	0.087( $\frac{10}{8}$ )	4.19( $\frac{67}{62}$ )	0.60	0.060(3)	29.27( $\frac{238}{206}$ )	1.00	...	...	101.7/ 71	1.43
101	0.095(4)	4.72( $\frac{38}{35}$ )	0.60	0.054( $\frac{2}{3}$ )	28.40( $\frac{230}{200}$ )	1.00	...	...	58.8/ 68	0.86
102	0.084( $\frac{7}{6}$ )	5.62( $\frac{105}{93}$ )	0.60	0.047( $\frac{5}{7}$ )	39.72( $\frac{1499}{1083}$ )	1.00	...	...	73.2/ 71	1.03
103	0.078(5)	5.09( $\frac{70}{59}$ )	0.60	0.057(3)	29.50( $\frac{301}{252}$ )	1.00	...	...	80.8/ 71	1.14
104	0.043(7)	6.24( $\frac{215}{138}$ )	0.60	0.054( $\frac{3}{3}$ )	32.79( $\frac{324}{267}$ )	1.00	...	...	85.6/ 68	1.26
105	0.094( $\frac{9}{9}$ )	6.69(46)	1.16( $\frac{14}{9}$ )	0.032( $\frac{4}{4}$ )	72.83( $\frac{883}{711}$ )	1.50( $\frac{52}{33}$ )	0.00	1.21	95.0/ 66	1.44
106	...	...	...	0.047(2)	25.39( $\frac{163}{178}$ )	1.00	0.00	0.91	95.7/ 70	1.37
107	...	...	...	0.060(2)	28.38( $\frac{153}{146}$ )	1.00	0.00	0.95	83.2/ 70	1.19
108	0.068(7)	4.62( $\frac{72}{62}$ )	0.60	0.059(2)	27.85( $\frac{177}{158}$ )	1.00	...	...	92.9/ 68	1.37
109	0.072( $\frac{13}{5}$ )	4.37( $\frac{108}{95}$ )	0.60	0.060(3)	30.79( $\frac{323}{276}$ )	1.00	...	...	101.7/ 71	1.43
110	0.060( $\frac{7}{8}$ )	5.67( $\frac{147}{115}$ )	0.60	0.059(4)	26.11( $\frac{260}{218}$ )	1.00	...	...	90.6/ 68	1.33
111	...	...	...	0.065(1)	32.04( $\frac{125}{127}$ )	1.00	...	...	98.1/ 66	1.49
112	...	...	...	0.053(2)	29.44( $\frac{195}{242}$ )	1.00	0.00	1.76	105.4/ 68	1.55
113	...	...	...	0.042( $\frac{3}{3}$ )	25.82( $\frac{215}{197}$ )	1.00	0.00	1.10	131.2/ 68	1.93
114	...	...	...	0.046(1)	31.25( $\frac{194}{154}$ )	1.00	0.00	0.99	106.0/ 60	1.77
115	0.050(4)	14.02( $\frac{93}{76}$ )	1.84( $\frac{22}{20}$ )	...	...	...	0.00	1.23	55.4/ 59	0.94
116	0.053( $\frac{7}{6}$ )	9.93( $\frac{44}{50}$ )	2.61( $\frac{49}{42}$ )	0.065(2)	24.11( $\frac{120}{110}$ )	1.00	0.00	0.96	94.6/ 63	1.50
117	0.046( $\frac{11}{8}$ )	4.65( $\frac{139}{108}$ )	0.60	0.057(2)	27.08( $\frac{162}{146}$ )	1.00	0.00	1.11	100.0/ 69	1.45
118	0.038( $\frac{11}{8}$ )	9.81( $\frac{67}{94}$ )	2.58( $\frac{108}{76}$ )	0.049(2)	24.54( $\frac{246}{194}$ )	1.00	...	...	70.1/ 59	1.19
119	0.070( $\frac{19}{15}$ )	5.67( $\frac{187}{146}$ )	0.60	0.055( $\frac{2}{4}$ )	36.45( $\frac{435}{354}$ )	1.00	...	...	130.4/ 70	1.86
120	0.122(4)	3.34( $\frac{18}{16}$ )	0.60	0.051(3)	27.13( $\frac{292}{225}$ )	1.00	...	...	70.6/ 68	1.04

No	Prop.-ID	PCU off	JD-2400000	date	Exp. ks	$R_1$	$f_1$ $10^{-1}$ Hz	$Q_1$	$R_2$	$f_2$ Hz	$Q_2$
121	P50110-30		52006.660	2001.04.07	1.6	$0.246(\frac{4}{5})$	$1.45(6)$	0.50	$0.209(\frac{3}{4})$	$12.39(53)$	0.60
122	P50110-30	14	52006.798	2001.04.07	2.9	$0.251(4)$	$1.06(4)$	0.50	$0.224(3)$	$10.44(33)$	0.60
123	P50110-32	13/14	52034.545	2001.05.05	10.4	$0.259(\frac{2}{4})$	$1.41(2)$	0.50	$0.226(1)$	$12.97(19)$	0.60
124	P50110-33	13/14/34	52048.554	2001.05.19	3.4	$0.259(4)$	$0.80(3)$	0.50	$0.215(3)$	$6.60(\frac{28}{27})$	0.60
125	P50110-34	13/34	52064.516	2001.06.04	3.9	$0.252(3)$	$1.09(\frac{3}{4})$	0.50	$0.222(2)$	$10.91(\frac{32}{30})$	0.60
126	P50110-34	1/4	52064.716	2001.06.04	4.3	$0.258(3)$	$1.24(\frac{4}{3})$	0.50	$0.216(3)$	$11.00(33)$	0.60
127	P50110-35	13/14/34	52076.496	2001.06.15	12.3	$0.243(2)$	$1.07(2)$	0.50	$0.217(2)$	$8.81(16)$	0.60
128	P50110-35	1	52076.433	2001.06.15	1.9	$0.229(5)$	$1.10(\frac{6}{5})$	0.50	$0.223(4)$	$8.89(38)$	0.60
129	P50110-36	1/4	52092.392	2001.07.01	5.3	$0.239(3)$	$1.36(3)$	0.50	$0.226(2)$	$12.08(\frac{31}{23})$	0.60
130	P50110-41	1/4	51979.788	2001.03.11	9.6	$0.266(2)$	$1.47(2)$	0.50	$0.219(1)$	$13.38(20)$	0.60



No	$R_3$	$f_3$ Hz	$Q_3$	$R_4$	$f_4$ Hz	$Q_4$	$A_{\text{PL}}$	$\alpha$	$\chi^2/\text{dof}$	$\chi^2_{\text{red}}$
121	0.087(6)	4.94( $\frac{77}{67}$ )	0.60	0.052( $\frac{4}{5}$ )	31.23( $\frac{295}{363}$ )	1.00	...	...	97.7/ 67	1.46
122	0.083(5)	4.72( $\frac{65}{54}$ )	0.60	0.044( $\frac{5}{6}$ )	37.23( $\frac{860}{655}$ )	1.00	...	...	65.7/ 68	0.97
123	0.063(4)	4.98( $\frac{54}{48}$ )	0.60	0.043(2)	29.53( $\frac{289}{249}$ )	1.00	0.00	1.06	123.3/ 66	1.87
124	0.141(3)	3.09(16)	0.60	0.054(4)	23.10( $\frac{504}{355}$ )	1.00	...	...	64.6/ 70	0.92
125	0.104(4)	4.70( $\frac{39}{36}$ )	0.60	0.050(4)	31.89( $\frac{577}{448}$ )	1.00	...	...	92.3/ 65	1.42
126	0.101(5)	3.97( $\frac{33}{30}$ )	0.60	0.059(2)	26.64( $\frac{196}{180}$ )	1.00	...	...	88.4/ 71	1.25
127	0.122(2)	3.72(12)	0.60	0.052(2)	27.83( $\frac{199}{185}$ )	1.00	...	...	82.5/ 68	1.21
128	0.115(5)	3.72( $\frac{31}{27}$ )	0.60	0.058(3)	29.02( $\frac{294}{262}$ )	1.00	...	...	62.8/ 71	0.89
129	0.082(3)	4.91( $\frac{39}{35}$ )	0.60	0.051(2)	30.08( $\frac{268}{230}$ )	1.00	...	...	100.2/ 71	1.41
130	0.064(3)	5.17(50)	0.60	0.046(2)	28.46( $\frac{196}{173}$ )	1.00	0.00	2.30	89.3/ 66	1.35

No	$R_{\text{add},1}$	$f_{\text{add},1}$ Hz	$Q_{\text{add},1}$	$R_{\text{add},2}$	$f_{\text{add},2}$ Hz	$Q_{\text{add},2}$	$R_{\text{add},3}$	$f_{\text{add},3}$ Hz	$Q_{\text{add},3}$
1	0.030	0.21	2000.00	...	...	...	...	...	...
2	0.068	0.21	4.31	...	...	...	...	...	...
3	0.060	0.15	7.19	...	...	...	...	...	...
4	0.052	0.29	9.24	...	...	...	...	...	...
5	0.073	0.22	4.39	...	...	...	...	...	...
6	0.040	0.41	9.03	...	...	...	...	...	...
7	...	...	...	...	...	...	...	...	...
8	...	...	...	...	...	...	...	...	...
9	0.032	0.37	2000.00	...	...	...	...	...	...
10	...	...	...	...	...	...	...	...	...
11	0.082	0.12	7.62	...	...	...	...	...	...
12	0.033	0.21	2000.00	...	...	...	...	...	...
13	0.040	0.12	270.48	...	...	...	...	...	...
14	0.106	0.18	2.15	...	...	...	...	...	...
15	0.040	0.19	2000.00	...	...	...	...	...	...
16	...	...	...	...	...	...	...	...	...
17	...	...	...	...	...	...	...	...	...
18	0.046	0.20	11.58	...	...	...	...	...	...
19	...	...	...	...	...	...	...	...	...
20	0.029	0.21	2000.00	...	...	...	...	...	...
21	0.069	0.33	5.13	...	...	...	...	...	...
22	0.047	0.22	10.97	...	...	...	...	...	...
23	0.036	0.21	2000.00	...	...	...	...	...	...
24	...	...	...	...	...	...	...	...	...
25	0.042	0.81	9.20	...	...	...	...	...	...
26	0.031	0.36	214.11	...	...	...	...	...	...
27	...	...	...	...	...	...	...	...	...
28	...	...	...	...	...	...	...	...	...
29	...	...	...	...	...	...	...	...	...
30	0.037	0.89	6.38	...	...	...	...	...	...
31	...	...	...	...	...	...	...	...	...
32	...	...	...	...	...	...	...	...	...
33	...	...	...	...	...	...	...	...	...
34	0.031	0.35	13.87	...	...	...	...	...	...
35	0.024	0.41	2000.00	...	...	...	...	...	...
36	...	...	...	...	...	...	...	...	...
37	0.028	0.41	19.09	...	...	...	...	...	...
38	0.019	0.48	1077.16	...	...	...	...	...	...
39	0.025	0.37	2000.00	...	...	...	...	...	...
40	0.040	0.42	8.71	...	...	...	0.032	0.04	8.58



No	$R_{\text{add},1}$	$f_{\text{add},1}$ Hz	$Q_{\text{add},1}$	$R_{\text{add},2}$	$f_{\text{add},2}$ Hz	$Q_{\text{add},2}$	$R_{\text{add},3}$	$f_{\text{add},3}$ Hz	$Q_{\text{add},3}$
81	0.037	0.75	9.10	...	...	...	...	...	...
82	0.031	0.97	12.25	0.036	0.43	12.65	0.043	0.05	4.19
83	...	...	...	0.028	0.41	50.66	...	...	...
84	0.026	0.63	2000.00	...	...	...	...	...	...
85	0.072	0.29	3.33	0.029	0.15	713.33	...	...	...
86	...	...	...	...	...	...	0.016	0.02	62.54
87	...	...	...	...	...	...	...	...	...
88	0.024	0.35	2000.00	0.068	0.19	9.59	...	...	...
89	...	...	...	...	...	...	...	...	...
90	0.028	0.80	7.90	...	...	...	...	...	...
91	...	...	...	...	...	...	...	...	...
92	...	...	...	0.084	0.15	9.56	...	...	...
93	...	...	...	0.036	0.13	14.87	...	...	...
94	...	...	...	0.077	0.08	8.87	...	...	...
95	...	...	...	...	...	...	...	...	...
96	...	...	...	...	...	...	...	...	...
97	...	...	...	...	...	...	...	...	...
98	...	...	...	...	...	...	...	...	...
99	...	...	...	...	...	...	...	...	...
100	...	...	...	...	...	...	...	...	...
101	0.016	0.97	2000.00	...	...	...	...	...	...
102	...	...	...	...	...	...	...	...	...
103	...	...	...	...	...	...	...	...	...
104	0.018	0.87	35.85	...	...	...	...	...	...
105	...	...	...	...	...	...	...	...	...
106	...	...	...	...	...	...	...	...	...
107	...	...	...	...	...	...	...	...	...
108	0.023	0.63	2000.00	...	...	...	...	...	...
109	...	...	...	...	...	...	...	...	...
110	...	...	...	...	...	...	0.040	0.11	9.51
111	0.033	1.11	9.23	...	...	...	0.022	0.10	11.78
112	0.021	0.87	13.86	...	...	...	...	...	...
113	0.029	0.79	9.16	...	...	...	...	...	...
114	0.031	3.24	7.83	0.068	1.48	3.17	0.062	0.09	0.76
115	0.042	0.11	2.88	0.023	0.32	7.06	0.121	0.07	0.08
116	0.032	1.34	13.80	...	...	...	...	...	...
117	...	...	...	...	...	...	...	...	...
118	0.053	0.95	5.06	0.052	0.02	1.12	0.023	0.01	580.12
119	...	...	...	...	...	...	...	...	...
120	0.021	0.77	50.90	...	...	...	...	...	...

No	$R_{\text{add},1}$	$f_{\text{add},1}$ Hz	$Q_{\text{add},1}$	$R_{\text{add},2}$	$f_{\text{add},2}$ Hz	$Q_{\text{add},2}$	$R_{\text{add},3}$	$f_{\text{add},3}$ Hz	$Q_{\text{add},3}$
121	0.041	1.07	5.68	...	...	...	...	...	...
122	...	...	...	0.058	0.43	8.61	...	...	...
123	0.019	0.63	376.83	...	...	...	...	...	...
124	...	...	...	...	...	...	...	...	...
125	0.043	0.93	7.89	0.027	0.45	2000.00	...	...	...
126	...	...	...	...	...	...	...	...	...
127	0.029	0.77	7.94	...	...	...	...	...	...
128	...	...	...	...	...	...	...	...	...
129	...	...	...	...	...	...	...	...	...
130	...	...	...	...	...	...	0.051	0.03	1.20

## *Acknowledgements*

First of all I want to thank my thesis advisor Prof. Rüdiger Staubert for making this work possible and for being always and patiently available for questions and discussions. Apart from his scientific input, I am grateful for having seen and learned about graceful and fair “managing” of science by being part of his group.

For support, help, and discussions during everyday work I owe Prof. Staubert’s, assistant Dr. Jörn Wilms profound thanks. One of the unbelievable many projects he successfully initiated is the DFG grant (and its extension) for my PhD project. Together Jörn and Dr. Michael Nowak (see below) pioneered the fundamental methods and ideas that were first applied on a greater scale during the Cyg X-1 campaign described in this work. Jörn was my main collaborator in the work presented here and I want to thank him very much for the good team work.

I experienced the open and friendly atmosphere in the X-ray working group of Prof. Staubert and the stellar atmospheres working group of Prof. Klaus Werner as very motivating and want to thank all the people responsible for this exceptional climate. Especially I want to thank the “Espresso Runde” for many witty, interesting, knowledge-providing after-mensa-espresso-times. I will surely miss you all.

I thank my office mate Lic. Math. Sara Benloch for good companionship during work & breaks. Dipl. Phys. Ingo Kreykenbohm always was a good office neighbour and only his installation of my somewhat complicated laptop made the actual writing of this thesis possible under conditions where I had to be mobile. I am happy that Dipl. Phys. Thomas Gleissner is continuing the Cyg X-1 campaign project at the IAAT since there are still many interesting questions to explore with that data and since the “hand-over” phase went very smoothly.

A very important experience for me was the collaboration with people from other institutes, mainly with Dr. Michael Nowak, from the Center for Space Research (CSR, MIT), Boston, and formerly from Jila (CU), Boulder, and with Dr. William Heindl, Emrah Kalemci, and others from the Center for Astronomy and Space Science (CASS, UCSD), La Jolla. In this context I am thankful for having had the opportunity for several visits to Boulder and La Jolla and I want to thank Prof. Mitchell Begelman and Dr. Richard Rothschild and their respective groups very much for their hospitality.

I also had the opportunity to participate in ground-based observations, for Dr. Thomas Rauch’s (IAAT) planetary nebulae program as well as for my own project (with Jörn and Thomas). I especially thank Thomas for including me into his observing run in Israel.

Astronomers that I had the pleasure to meet during my work for this thesis and that influenced it are, e.g., Dr. Robert Fender, Dr. Catherine Brocksopp, Prof. Guy Pooley, Dr. David M. Smith, and Dr. Ronald Remillard.

A group of physicists – Dipl. Phys. Karin Hauser, Dipl. Phys. Stephanie Oberkirsch, Dipl. Phys. Henrike Prochel, Dipl. Phys. Anton Pichler, and myself – started their first semester in Tübingen at the same time, then went into quite different fields of physics, and now help each other to look “over the rim” every once in a while, and will hopefully keep up the meetings in the future. Thank you for the nice hikes & more!

Last but not least I could not have pursued astronomy so freely without the support of my parents. Without them this work would not be. They and my sister have always been there for me and I thank them deeply.

## *Lebenslauf*

- 31.05.1971 geboren in Aurich, Niedersachsen
- 09.1977–01.1980 Volksschule Freising-Neustift, Bayern
- 01.1980–07.1980 Trinity Lutheran Elementary School, Norfolk, VA, USA
- 07.1980–11.1980 Volksschule Freising-Neustift, Bayern
- 11.1980–12.1984 Deutsche Abt. der International School SHAPE, Mons, Belgien  
seit 1981: Gymnasialstufe
- 12.1984–05.1990 Gymnasium Balingen, Baden-Württemberg
- 05.1990 Abitur
- 10.1990–09.1997 Eberhard-Karls-Universität Tübingen, Studium der Physik
- 03.1993 Vordiplom
- 03.1996–05.1997 Diplomarbeit über die “Anwendung Linearer Zustandsraummodelle auf die Kurzzeitvariabilität des Schwarzkochkandidaten Cynus X-1” unter der Anleitung von Herrn Prof. Dr. R. Staubert:
- 05.1997 Diplom
- 08.1997–09.1997 wissenschaftliche Angestellte, IAA Tübingen
- 10.1997–04.1998 Eberhard-Karls-Universität Tübingen, Zweitstudium Informatik
- 10.1997–12.1997 Forschungsaufenthalt an der University of California at San Diego, La Jolla, CA, USA (DAAD Fellowship)
- 01.1998–02.2002 wissenschaftliche Angestellte, IAA Tübingen
- 08.1997–07.2002 Anfertigung der Dissertation mit dem Titel “Accretion Disk Weather of Black Hole X-Ray Binaries – The Case of Cygnus X-1” an der Universität Tübingen, Institut für Astronomie und Astrophysik, Abt. Astronomie, unter Anleitung von Herrn Prof. Dr. R. Staubert
- 03.2002– wissenschaftliche Angestellte, Max-Planck-Institut für extraterrestrische Physik, Garching  
Dienstaufgabe: Archive Scientist für die INTEGRAL Mission  
Dienstort: INTEGRAL Science Data Center, Versoix, Schweiz

Meine akademischen Lehrer waren die Professoren, Dozenten und Dozentinnen Dres.:

*Angewandte Physik:* K. Gaukler, H. Lichte

*Astronomie und Astrophysik:* H. Mauder, H. Ruder, R. Staubert, K. Werner

*Chemie:* J. Strähle, H. Ebert

*Experimentalphysik:* M. Baumann, H. Clement, F. Gönnerwein, W. Hartmann,  
R. Hübener, O. Lutz, W. Nakel, G. Staudt, G. Wagner

*Mathematik:* H. Kaul, M. Wolff, A. Wörz

*Theoretische Physik:* A. Fäßler, H. Müther, H. Reinhardt, H. Stumpf, H. Wittern